Amorphous and microcrystalline silicon applied in very thin tandem solar cells

Sandra Schicho

JÜLICH
FORSCHUNGSZENTRUM

Mitglied der Helmholtz-Gemeinschaft

Schriften des Forschungszentrums Jülich
Reihe Energie & Umwelt / Energy & Environment Band / Volume 99

Forschungszentrum Jülich GmbH
Institute of energy and climate research (IEK)
Photovoltaics (IEK-5)

Amorphous and microcrystalline silicon applied in very thin tandem solar cells

Sandra Schicho

Schriften des Forschungszentrums Jülich
Reihe Energie & Umwelt / Energy & Environment Band / Volume 99

ISSN 1866-1793 ISBN 978-3-89336-693-4

Bibliographic information published by the Deutsche Nationalbibliothek.
The Deutsche Nationalbibliothek lists this publication in the Deutsche Nationalbibliografie; detailed bibliographic data are available in the Internet at http://dnb.d-nb.de.

Publisher and Distributor:	Forschungszentrum Jülich GmbH Zentralbibliothek 52425 Jülich Phone +49 (0) 24 61 61-53 68 · Fax +49 (0) 24 61 61-61 03 e-mail: zb-publikation@fz-juelich.de Internet: http://www.fz-juelich.de/zb
Cover Design:	Grafische Medien, Forschungszentrum Jülich GmbH
Printer:	Grafische Medien, Forschungszentrum Jülich GmbH
Copyright:	Forschungszentrum Jülich 2011

Schriften des Forschungszentrums Jülich
Reihe Energie & Umwelt / Energy & Environment Band / Volume 99

D 82 (Diss.,RWTH Aachen University, 2011)

ISSN 1866-1793
ISBN 978-3-89336-693-4

The complete volume ist freely available on the Internet on the Jülicher Open Access Server (JUWEL) at http://www.fz-juelich.de/zb/juwel

Contents

Abstract

Thin-film solar cells are fabricated by low-cost production processes, and are therefore an alternative to conventionally used wafer solar cells based on crystalline silicon. Due to the different band gaps, tandem cells that consist of amorphous (a-Si:H) and microcrystalline (μc-Si:H) single junction solar cells deposited on top of each other use the solar spectrum much more efficient than single junction solar cells. The silicon layers are usually deposited on TCO (Transparent Conductive Oxide)-coated glass and metal- or plastic foils. Compared to the CdTe and CIGS based thin-film technologies, silicon thin-film solar cells have the advantage that no limitation of raw material supply is expected and no toxic elements are used. Nevertheless, the production cost per Watt-peak is the decisive factor concerning competitiveness and can be reduced by, e.g., shorter deposition times or reduced material consumption. Both cost-reducing conceptions are simultaneously achieved by reducing the a-Si:H and μc-Si:H absorber layer thicknesses in a tandem device.

In the work on hand, the influence of an absorber layer thickness reduction up to 77% on the photovoltaic parameters of a-Si:H/μc-Si:H tandem solar cells was investigated. An industry-oriented Radio Frequency Plasma-Enhanced Chemical Vapour Deposition (RF-PECVD) system was used to deposit the solar cells on glass substrates coated with randomly structured TCO layers. The thicknesses of top and bottom cell absorber layers were varied by adjusting the deposition time. Reduced layer thicknesses lead to lower absorption and, hence, to reduced short-circuit current densities which, however, are partially balanced by higher open-circuit voltages and fill factors. Furthermore, by using very thin amorphous top cells, the light-induced degradation decreases tremendously. Accordingly, a thickness reduction of 75% led to an efficiency loss of only 21 %.

By adjusting the parameters for the deposition of a-Si:H top cells, a wider band gap of the intrinsic absorber and window-p-type doped material was achieved. Higher open-circuit voltages were observed using such materials. Two different types of high band

gap amorphous absorber layers with the associated p-doped layers were implemented into very thin tandem cells.

An elongation of the light path in the absorber material, which is usually accomplished by using textured front contacts and back reflectors, is crucial for the performance of very thin tandem cells. Periodically patterned aluminum plates, which had shown very good light trapping properties for μc-Si:H single junction solar cells, were suggested as substrates for very thin tandem cells. In comparison to tandem cells on standard substrates, higher short-circuit current densities and quantum efficiencies were observed on Al that indicated good light trapping. However, tandem cells on aluminum plates exhibited much lower open-circuit voltages. Raman measurements revealed a higher crystallinity and compressive stress in the microcrystalline bottom cells deposited on aluminum plates compared to cells deposited on standard substrates under the same deposition conditions.

The silane concentration that is applied for the deposition of μc-Si:H influences the crystalline volume fraction in a way that under otherwise constant deposition conditions lower values lead to higher crystalline volume fractions. By means of a sample series for which different silane concentrations were applied the orientation of the cubic silicon crystals and the appearance of stacking faults or twinning in the microcrystalline layers were investigated depending on silane concentration and crystalline volume fraction. For these studies, Raman spectroscopy with two different excitation lasers and X-ray diffraction in Bragg-Brentano and Grazing Incidence geometry were carried out. No preferential orientation of the silicon crystals in the investigated materials was detected by asymmetrical Grazing Incidence XRD measurements or by symmetrical Bragg-Brentano measurements. However, in all investigated layers stacking faults and twins were discovered which appear as hexagonal phase in the diffractograms of the microcrystalline silicon. To gain more information about the phase transition from amorphous to microcrystalline and microcrystalline to amorphous silicon depth resolved XRD and Raman measurements were performed. Therefore, intrinsic layers with a crystallinity gradient in growth direction were deposited by applying a linear decreasing and increasing silane concentration, respectively. Raman measurements along a wedge-

shaped, well-defined etch crater were compared to XRD measurements under varying incident angles in regards to crystallinity. It was found that the phase transition from a-Si:H to μc-Si:H and μc-Si:H to a-Si:H both occur in a very narrow silane concentration range which shows the importance of a precise adjustment to achieve transition material which is preferred for photovoltaic application.

Zusammenfassung

Dünnschichtsolarzellen sind aufgrund ihrer kostengünstigen Herstellung eine Alternative zu konventionellen Solarmodulen aus kristallinem Silizium. Tandemzellen, bei denen zwei Einzelzellen aus amorphem (a-Si:H) und mikrokristallinem (µc-Si:H) Silizium übereinander abgeschieden werden, nutzen das Sonnenspektrum aufgrund der verschiedenen Bandlücken effizienter als Einzelzellen. Dadurch erhöht sich der Wirkungsgrad stark. Die Siliziumschichten werden im Allgemeinen auf TCO (Transparent Conductive Oxide)-beschichtete Glassubstrate und preiswerte Metall- oder Plastikfolien abgeschieden. Im Vergleich zu Dünnschichttechnologien, die auf CdTe und CIGS basieren, haben Silizium-Dünnschichtsolarzellen den Vorteil, dass keine Rohstoffknappheit zu erwarten ist und sie keine giftigen Stoffe enthalten. Geringere Produktionskosten pro Watt-Peak sind in Hinblick auf die Wettbewerbsfähigkeit notwendig und können zum Beispiel durch kürzere Depositionszeiten oder geringere Materialkosten realisiert werden. Diese beiden Möglichkeiten der Kostensenkung können gleichzeitig durch eine Reduzierung der a-Si:H- und µc-Si:H-Absorberschichtdicken in Tandemzellen erreicht werden.

In der vorliegenden Arbeit wurde untersucht, welchen Einfluss eine signifikante (bis zu 77%) Reduzierung der Absorberschichtdicken auf die Solarzellenparameter von a-Si:H/µc-Si:H Tandemzellen hat. Die untersuchten Tandemzellen wurden in einem industrienahen RF-PECVD (Radio Frequency Plasma-Enhanced Chemical Vapour Deposition)-System auf TCO-beschichtete Glassubstrate abgeschieden, die eine nicht-periodische Oberflächenstruktur aufwiesen. Verschiedene Siliziumschichtdicken wurden durch Anpassung der Depositionszeiten erreicht. Auf der einen Seite führt die Reduzierung der Schichtdicken zu einer Abnahme der Absorption, und folglich der Kurzschlussstromdichten, was jedoch durch höhere Leerlaufspannungen und Sammlungseffizienzen teilweise ausgeglichen wird. Auf der anderen Seite sinkt die lichtinduzierte Degradation der sehr dünnen amorphen Topzellen erheblich. So führte eine Reduzierung der Gesamtschichtdicke um 75% zu einer Wirkungsgradeinbuße von nur 21%.

Durch Anpassung der a-Si:H-Depositionsbedingungen wurde eine Aufweitung der Bandlücke in der p-dotierten Fensterschicht sowie dem intrinsischen Absorbermaterial erreicht, was zu einer weiteren Erhöhung der Leerlaufspannung führte. Zwei so optimierte Topzellentypen wurden in dünne Tandemzellen eingesetzt und führten zu einer deutlich verbesserten Solarzelleneffizienz gegenüber dünnen Tandemzellen mit Standard-Topzellen.

Sehr dünne Tandemzellen sind auf eine effiziente Lichtwegverlängerung im Absorbermaterial angewiesen, was zum Beispiel durch texturierte Vorderseitenkontakte und Rückreflektoren erreicht wird. Periodisch strukturierte Aluminiumsubstrate hatten sehr gute Lichteinfangeigenschaften in µc-Si:H-Einzelzellen gezeigt, was eine Anwendung als Substrat für sehr dünne Tandemzellen nahelegte. Im Vergleich zu Tandemzellen auf Standardsubstraten mit nicht-periodischer Oberflächentextur wurden erhöhte Kurzschlussstromdichten und Quanteneffizienzen für Tandemzellen auf Aluminiumsubstraten ermittelt, was auf verbesserten Lichteinfang hindeutete. Jedoch erreichten die letztgenannten Tandemzellen vergleichsweise niedrige Leerlaufspannungen. Raman-Analysen zeigten einen höheren kristallinen Anteil sowie Kompressionsspannung im mikrokristallinen Silizium der Bottomzelle auf Aluminiumsubstraten im Vergleich zu Standardsubstraten, wobei die Tandemzellen unter gleichen Depositionsbedingungen abgeschieden wurden. Diese beiden Struktureigenschaften der auf Aluminium gewachsenen Tandemzellen wurden zur Erklärung der niedrigen Leerlaufspannungen herangezogen.

Weiterhin wurde die Mikrostruktur (z.B. Kristallorientierung, Kristallinität) von µc-Si:H in Abhängigkeit der während der Abscheidung verwendeten Silankonzentration untersucht. Unter sonst konstanten Depositionsbedingungen führen geringe Silankonzentrationen zu einem höheren kristallinen Volumenanteil in der mikrokristallinen Schicht. Dies wurde durch verschiedene Strukturanalysen, Röntgendiffraktometrie (XRD) in Bragg-Brentano-Geometrie und unter streifendem Einfall, sowie Raman-Spektroskopie mit zwei verschiedenen Anregungslaser-wellenlängen, bestätigt. Eine häufig diskutierte kristallographische Vorzugsorientierung der kubischen Siliziumkristalle konnte in den vorliegenden Materialien nicht

nachgewiesen werden, jedoch wurden Stapelfehler und Zwillinge detektiert. Um den Übergang zwischen µc-Si:H zu a-Si:H und a-Si:H zu µc-Si:H genauer zu untersuchen, wurden Schichten mit Kristallinitätsgradienten in Wachstumsrichtung deponiert. Diese Gradienten wurden durch linear zunehmende beziehungsweise linear abnehmende Silankonzentrationen realisiert. Durch Raman-Analysen an einem wohldefiniertem Ätzkrater wurden Kristallinitäten tiefenaufgelöst bestimmt und mit Einfallswinkel-abhängigen XRD-Messungen verglichen. Es zeigte sich, dass der Übergang von µc-Si:H zu a-Si:H und a-Si:H zu µc-Si:H in einem kleinen Silankonzentrationsfenster verläuft und daher eine präzise Einstellung der Depositionsparameter notwendig ist, um das für Solarzellenanwendung bevorzugte Übergangsmaterial herzustellen.

.

Chapter 1

Introduction

The history of photovoltaic energy conversion is closely connected to the development of semiconductor diodes and goes back to the year 1954 when Chapin, Fuller and Pearson from Bell Labs presented the first working solar cell which was based on crystalline silicon [1]. In the same year, Reynolds et al. reported on a simple cadmium sulfide solar cell [2] and only one year later Gremmelmeier introduced the first gallium arsenide solar cell [3]. Theoretical investigations evidenced that the absorption behaviour of crystalline silicon fits well to the sun spectrum. The so-called "Shockley-Queisser-limit" predicted a highest possible conversion efficiency of 33% for solar energy into electrical energy for absorber materials with band gaps E_g between 1 eV < E_g < 1.45 eV [4].

Due to the initially very high production costs and efforts crystalline silicon solar cells were first only used in extraterrestrial application but the call for cheaper fabrication led to the use of advanced technologies and investigations on new materials. In 1974, Spear et al. had successfully shown that it is possible to dope thin,

hydrogenated amorphous silicon (a-Si:H), deposited from a gas mixture of silane and hydrogen [5]. This finding paved the way for the development of amorphous thin-film solar cells using layer thicknesses ~ 100 times thinner than wafer-based solar cells. The first p-i-n solar cell with a-Si:H as absorber material, presented in 1976, had an efficiency of 2.4% [6]. Unfortunately, amorphous silicon exhibits light-induced degradation, which means that sun light creates dangling bonds that act as recombination centres and lead to a reduced solar cell performance [7]. One possibility to increase the stability against degradation is the combination of amorphous silicon based materials with identical or different band gaps to multijunction solar cells. The individual layers can be deposited much thinner which reduces the consequences of degradation, and, in case of different band gaps, the solar spectrum is used more efficiently. A stabilized efficiency up to 13.7% was achieved by a triple junction cell made of a-Si:H and a-SiGe:H [8].

Microcrystalline silicon (µc-Si:H) was first deposited by Vepřek and Mareček and describes material having small crystallites with a size of a few ten nanometres embedded in amorphous phase [9]. Because of its higher doping efficiency and conductivity µc-Si:H was initially used as doped layer material in amorphous silicon devices [10; 11]. It was not until 1994 that microcrystalline silicon was used also as absorber material in single junction solar cells [12]. The better absorption behaviour in the infrared wavelength region compared to amorphous silicon and a negligible degradation made µc-Si:H a suitable candidate for bottom cell intrinsic material in tandem cells as an alternative to a-SiGe:H. Triple junction solar cells with an a-Si:H/µc-Si:H/µc-Si:H structure are also possible and achieved 15% on lab scale [13]. A big advantage of the silicon based thin-film technology is its possibility to deposit on large areas. At present (2010), a-Si:H/µc-Si:H modules achieve up to 9.6% (total area) efficiency on 2.6 × 2.2 m² size [14], and just recently Oerlikon Solar reported on efficiencies of 10.0% in mass production on substrates sizes of 1.3 × 1.1 m² [15].

The demand for photovoltaic production is unbroken. The installed photovoltaic power increased from 5.95 GW in 2008 to 7.3 GW in 2009 from which about 68% were installed in Germany, Italy and the Czech Republic. Compared to Japan and the United

States whose share amounted to 6% and 7% [16], respectively, the important role of Germany in photovoltaic power generation becomes clear.

The photovoltaic market is still ruled by technologies based on mono- and multicrystalline silicon wafer solar cells. But the share of thin-film technologies, like cadmium telluride (CdTe), copper indium (gallium) (di)selenide (CI(G)S) or a-Si:H (including tandem and triple junction cells with µc-Si:H or a-SiGe:H) increased from 2008 to 2009 from 13% to 19.3%, and it is supposed to reach ~ 23.4% in 2010 [17] and 31% in the year 2013 [18]. Figure 1.1 shows the development of the worldwide photovoltaic production and emphasizes the increasing share of the thin-film production. The largest cell and panel producer in 2009 was First Solar applying CdTe thin-film technology [19].

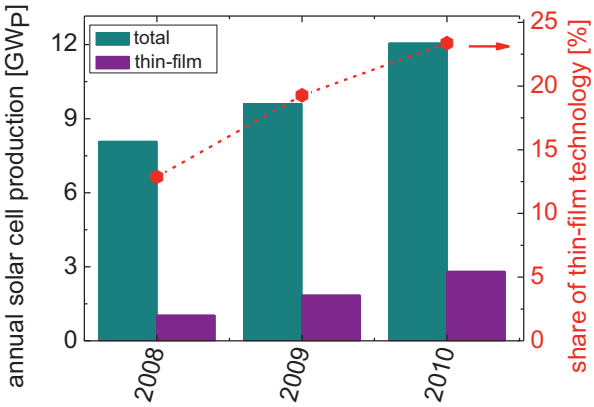

Figure 1.1 Annual solar cell production worldwide and the share of thin-film technology with predicted values for 2010 [17]

On the one hand, mono- and multicrystalline solar cells achieve higher average efficiencies between 14 – 19% in mass production compared to thin-film technology. On the other hand, the production costs are much lower for thin-film solar cells, which results in much lower costs per produced power. For comparison, the lowest retail price for multicrystalline silicon solar modules is 1.99 $/W (1.55 €/W), for a monocrystalline

silicon module 2.17 $/W (1.69 €/W) and for thin-film modules low retail prices of 1.07 $/W (0.83 €/W) are achieved [20] (September 2010).

First Solar reported on production costs of 0.76 €/W_p for CdTe modules reaching 11.2% in mass production [21]. Oerlikon Solar advertise equipment with which the lowest production price of 0.50 €/W_P for amorphous/microcrystalline silicon modules with stabilized efficiencies of 10% is achieved [15].

In future, the most decisive factor which technology will gain or lose market share is the ratio of costs per produced power. To be able to compete with other thin-film concepts and to sustain besides the crystalline silicon market it is necessary to further decrease the price per Watt-peak. The present thesis deals with aspects to achieve this aim.

After the technological and theoretical background is introduced in Chapter 2 an investigation on the reduction of the absorber layer thicknesses of a-Si:H/µc-Si:H tandem solar cells deposited on glass-based substrates is presented. Effects on the cell performance are discussed with special focus on the behaviour after light-induced degradation (Chapter 3).

Amorphous silicon with a high band gap was considered as top cell absorber material to further improve the open-circuit voltage of the very thin tandem cells. Detailed investigations and optimization of intrinsic and p-type doped amorphous material towards high open-circuit voltage-devices are presented in Chapter 4.

For enhancing the current generation in the very thin absorber layers honeycomb-structured aluminum that evidenced superior light trapping properties was suggested as substrate for thin tandem cells. Chapter 5 discusses the advantages and challenges of using Al plates as substrate for a-Si:H/µc-Si:H tandem cells.

Material properties strongly influence the electrical properties of microcrystalline silicon and the solar cell performance. Therefore, studies on the microstructure of differently deposited µc-Si:H by means of Raman spectroscopy and X-ray diffraction were carried out, and are shown in Chapter 6. The appearance of a preferential orientation and stacking faults is evaluated and discussed. Additionally, the phase

transitions from a-Si:H to μc-SiH and μc-SiH to a-Si:H are investigated by depth dependent Raman and XRD measurements.

Chapter 2

Fundamentals

This chapter gives a short overview of the material properties of amorphous and microcrystalline silicon, the sample preparation techniques, and characterization methods. Amorphous and microcrystalline silicon are described regarding their use in thin-film solar cells with special focus on tandem cells. The influence of the most important deposition parameters during the Plasma-Enhanced Chemical Vapour Deposition, which was used for the preparation of the thin films, is explained. Finally, the methods with which material properties and solar cell performances were investigated are described.

2.1 Physical and technological background

2.1.1 Hydrogenated amorphous silicon a-Si:H

Structure In a matrix silicon is connected by covalent bonds to four other silicon atoms that form a tetrahedron. In amorphous silicon, this well-ordered structure vanishes as it can be seen in Figure 2.1. Bonding lengths and angles vary from the crystalline lattice and some Si atoms have only three bonding partners, which leave so-called “dangling bonds”. These open bonds act as defects so that amorphous silicon shows very poor electrical properties. By incorporating hydrogen into the material the dangling bonds are partially passivated which makes an application in semiconductor devices or solar cells possible [22].

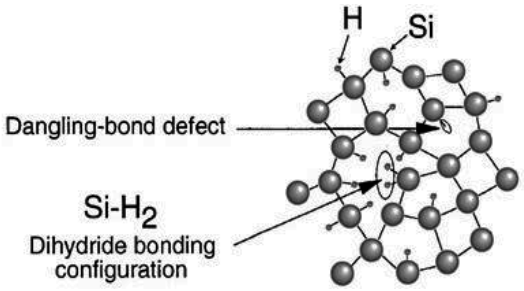

Figure 2.1 Structure of a-Si:H with dangling bonds [23]

Growth mechanism When the process gas mixture dissociates in the plasma radicals, ions and atoms are generated which will be explained in more detail in subsection 2.2.2. The main precursor for the growth of amorphous silicon is supposed to be SiH_3. When SiH_3 fragments with one unsaturated bond at the Si-atoms reach a hydrogen-terminated substrate surface, they may abstract one H-atom from a Si-atom under formation of SiH_4. A dangling bond is left on the Si-atom at the surface. A second SiH_3 diffuses to this dangling bond and forms a Si–Si bond as illustrated in Figure 2.2 [24]. Higher

deposition temperatures enhance the surface diffusivity and the abstraction of hydrogen, which leads to a more compact amorphous network with less hydrogen.

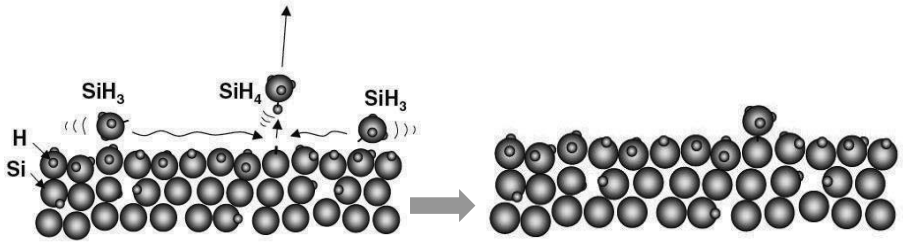

Figure 2.2 Growth of amorphous silicon: SiH_3 molecule fragments diffuse over the hydrogen-terminated surface and can abstract a hydrogen atom from a Si-atom. SiH_4 is formed which does not contribute to the film growth. A second SiH_3 may diffuse to the left dangling bond on the Si-atom on the surface where it attaches; the film grows [24].

Optical properties Conduction and valence band are separated by the band gap, which has a low density of states. Due to the disordered character of amorphous silicon the states of holes and electrons are not confined in the bands anymore [25] leading to band tail states near the band edges [26]. Therefore, no defined energy band gap can be detected for a-Si:H [27]. Often, the optical band gap is approached by the Tauc band gap E_T which is derived from the plot [28]

$$\alpha(h\nu) = (A/h\nu)(h\nu - E_T)^2. \tag{2.1}$$

The value E_T for a-Si:H amounts typically to ~ 1.75 eV [27]. It is also common to name the band gap by the photon energy, which corresponds to a certain absorption coefficient, e.g., $\alpha = 10^4$ cm^{-1} gives the E_{04} band gap.

Amorphous silicon is regarded as direct semiconductor due to the lack of long-range order. The momentum of electrons in the valence and conduction band is not determined and, consequently, no additional phonon is required for a transition between these states.

By changing the deposition conditions, e.g., hydrogen dilution or deposition temperature, band gap E_T values between 1.6 – 1.8 eV are achievable [29]. Alloying with carbon leads to a widening of the band gap E_T up to 2.6 eV whereas the incorporation of germanium reduces the band gap.

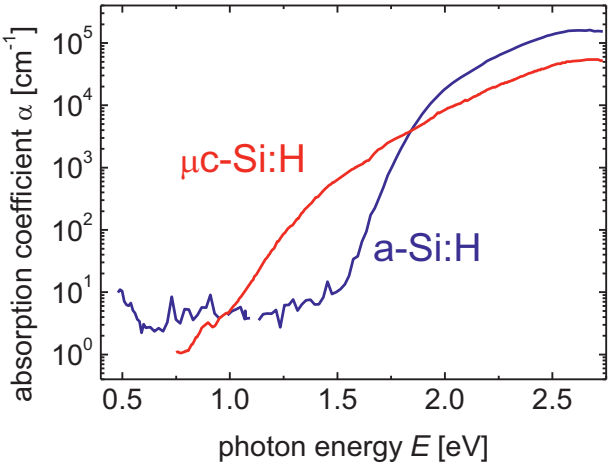

Figure 2.3 Absorption coefficient α as a function of photon energy of a-Si:H and μc-Si:H [30]

Figure 2.3 shows the absorption coefficient of hydrogenated amorphous silicon and μc-Si:H, both fabricated under standard conditions in Jülich at IEF5. Since a-Si:H is a direct semiconductor it has an high absorption coefficient for photon energies above ~ 1.85 eV. Consequently, amorphous silicon absorbs light with higher energies (shorter wavelengths) sufficiently while the absorption for light in the infrared region is low.

Staebler-Wronski-effect A drawback of a-Si:H regarding its use in semiconductor devices is the light-induced degradation. Staebler and Wronski found that dark and photoconductivity are tremendously reduced under illumination. The effect named after its two discoverers is attributed to the creation of defect states in the band gap acting as recombination centres and can be reversed by annealing at temperatures above 150°C [7]. The origin of the Staebler-Wronski-effect is still not fully understood. As a likely explanation, it is assumed that photogenerated electron-hole pairs recombine near a

week Si–Si bond and release energy high enough to break the bond. One Si atom may bond with a hydrogen atom leaving one dangling bond at the second Si atom where charge carriers can be trapped [31].

One way to reduce the efficiency loss of solar cells due to the Staebler-Wronski-effect is to use thinner a-Si:H absorber layers in stacked cells. A smaller number of defects are created in thinner layers and additionally a higher electric field builds up over the thin layers and recombination processes are reduced.

2.1.2 Microcrystalline Silicon

Structure Microcrystalline silicon (also referred to as nanocrystalline silicon), first deposited by Vepřek and Mareček in 1968 [9], is a phase mixture of crystals embedded in amorphous tissue. The silicon atoms are still arranged in tetrahedrons and form elementary cells in the face-centered cubic (fcc) structure. Adjacent crystals can be oriented differently and are separated by grain boundaries or amorphous phase. The latter represents the difference to multicrystalline silicon, which contains no amorphous tissue. The size of the crystals is about 10 nm to 20 nm that coalesce to conical shaped columns with a length of about 200 nm as it can be seen in Figure 2.4. Electrically active defects such as grain boundaries are passivated by hydrogen that reduces the carrier recombination in the material drastically [32].

The amount of crystalline phase (or crystallinity) is a crucial factor for the application in solar cells and is adjusted by choosing an adequate set of deposition parameters. The crystallinity, which is the portion of crystalline phase in relation to the total volume, is usually determined by Raman spectroscopy and should lie in the range of 60 – 70% [33; 34].

Usually, μc-Si:H exhibits a random crystal orientation for device-grade material [34; 35]. Although several research groups still controversially discuss the existence and importance of a preferential crystal orientation parallel to the {110} planes in μc-Si:H. The crystal orientation can be investigated by, e.g., X-ray diffraction or Transmission Electron Microscopy [36; 37].

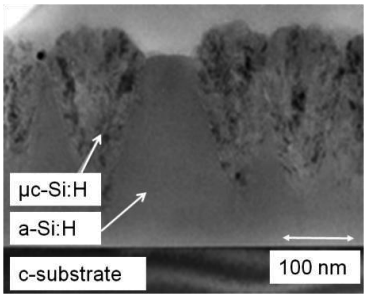

Figure 2.4 Appearance of crystalline phase embedded in amorphous matrix for µc-Si:H with low crystallinity [38]

Growth mechanism Several models are suggested for the growth of µc-Si:H which all have in common that atomic hydrogen plays an important role. In the *etching model*, introduced by Vepřek [9], the atomic hydrogen is supposed to etch weak, stressed, or angulated Si–Si bonds of amorphous tissue selectively, followed by a removal of Si atoms: A new precursor can now insert at this site, forming a more stable bond. The *surface diffusivity model* suggests that the high hydrogen dilution used for the preparation of µc-Si:H leads to an temperature independent H-coverage of the substrate surface. It also causes local heating due to exothermic hydrogen exchange reactions like the recombination of two hydrogen atoms to a hydrogen molecule [9], the abstraction of H from Si-H or the passivation of dangling Si-bonds by hydrogen. The third model, the so-called *chemical annealing model*, is based on the layer-by-layer growth technique where the amorphous silicon is exposed to hydrogen plasma, crystallization occurs under the assumption that H–atoms permeate into the growth region where a flexible crystalline network develops if sufficient H is present and the abstraction of Si-atoms is negligible [39].

Optical properties As shown in Figure 2.3 µc-Si:H exhibits a lower absorption coefficient α for high photon energies above ~ 1.85 eV as a-Si:H. The band gap varies with crystallinity, but generally amounts to ~ 1.1 eV [40; 41]. Consequently, µc-Si:H absorbs light in the infrared region. Because microcrystalline silicon has an indirect band gap, optical transitions require, additional to photons with suitable energy, the

participation of phonons [42]. Therefore, the probability of an optical induced transition is reduced. The overall low α, compared to other thin-film semiconductors with direct band gap like Cu(In,Ga)Se_2 and CdTe [43], makes it necessary to apply rather thick microcrystalline layers and/or to use light trapping structure.

2.1.3 Thin-film solar cells

In amorphous and microcrystalline silicon, the diffusion length of electrons and holes is low compared to mono- and multicrystalline silicon. Therefore, the transport of photogenerated charge carriers must be realized by a drift process, which is achieved by expanding the space charge region by inserting an intrinsic layer between the p-type and n-type doped regions [44].

Design of p-i-n single junction solar cells The design of a thin-film solar cell is shown in Figure 2.5. As substrate, usually transparent glass is chosen on which the front contact, a so-called transparent conductive oxide (TCO), is deposited. Such TCOs are tin-doped indium oxide (In_2O_3:Sn; short: ITO), fluorine-doped tin dioxide (SnO_2:F) or gallium- or aluminum-doped zinc oxide (ZnO:Ga/Al). A certain roughness of the TCO layer acts as light diffuser and enhances the path length through the thin silicon layer.

As positive pole a boron doped p-type layer with a thickness of approximately 15 – 20 nm is used. In case of an a-Si:H single junction cell carbon is incorporated into the a-Si:H p-doped layer to widen the band gap and enhancing the transparency.

The absorber layer thickness is a trade-off between sufficient light absorption and long deposition times, and in case of a-Si:H absorber layers, light-induced degradation which increases with layer thickness. Typical thicknesses of intrinsic a-Si:H and μc-Si:H layers single junction solar cells are ~ 300 nm and 1 – 1.5 μm, respectively.

Due to the lower conductivity compared to n-type doped μc-Si:H often n-type a-Si:H is used as negative pole to avoid current collection from outside of the defined cell area. Finally, a stack of zinc oxide and a highly reflecting metal, e.g., chromium or silver, is used as back reflector/contact.

The structure of solar cells in the n-i-p configuration is basically the same. The inverted deposition sequence offers the possibility of using non-transparent substrates. This type of solar cells will be discussed in more detail in chapter 5.

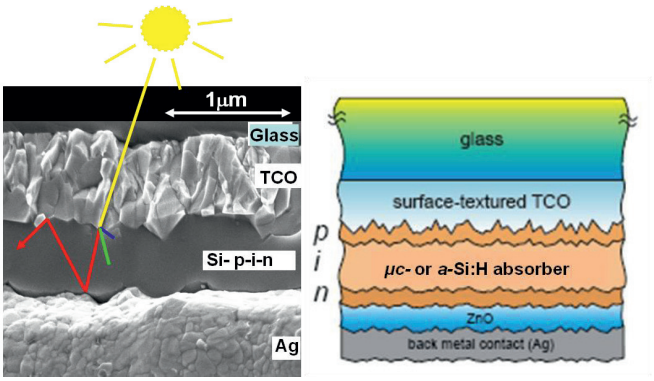

Figure 2.5 Image taken by Scanning Electron Microscopy (SEM) (left) and a scheme of a p-i-n single junction solar cell with its component layers (right) (by Zeman, 2007). The light enters the cell though the glass side and is scattered by the rough TCO into the silicon layers where it is absorbed.

Operation In the p-i-n solar cell, the light enters at the substrate side and travels through the TCO and p-doped layer where the absorption should be as low as possible. Due to the textured surface of the TCO layer, the light is scattered into the absorber layer where charge carriers are generated.

The optical inactive and highly conductive p- and n-type doped layers build a potential over the intrinsic layer. Charge carriers that are generated by incident light in the absorber layer are separated by the electrical field and drift to the corresponding contacts. Due to defects in the material photogenerated charge carriers can recombine again and do not contribute to the current. Therefore, it is necessary that the driving force for the charge carrier drift, the average electric field $\overline{E}$, is sufficiently high. The definition of $\overline{E}$ is given by:

$$\overline{E} = (V_D - V)/d_i \tag{2.2}$$

with V_D as the built-in potential, V as the external applied voltage and d_i as the absorber layer thickness. Since the charge carrier separation is realized by a drift process, p-i-n solar cells are also called drift cells in contrast to diffusion cells where the charge separation is realized by diffusion.

Photovoltaic parameters To characterize the performance of the solar cell four parameters are generally regarded which are derived from the current-voltage-(*IV*)-characteristics: conversion efficiency η, fill factor *FF*, open-circuit voltage V_{oc} and short-circuit current density J_{sc}.

The *IV*-characteristic of a solar cell is often approximated by the superposition of the *IV*-curve of the solar cell diode in the dark and the photocurrent under illumination [45]. The charge carrier generation results in a shift of the *IV*-curve into the fourth quadrant where power can be extracted from the diode. A photocurrent I_{photo} adds to the dark current of an ideal diode I_{diode} so that the diode equation changes to

$$I = I_0 \left(e^{\frac{qV_{diode}}{kT}} - 1 \right) - I_{photo} \tag{2.3}$$

with I_0 as the dark saturation current, T as the temperature, k as the Boltzmann factor and q as the elementary charge. If I_{photo} reaches the value of I_{diode} the net current flow through the cell is zero and the voltage is at its maximum possible value, the open-circuit voltage V_{oc}. The short-circuit current I_{sc} results from the collection of photogenerated carriers and is accessible when the voltage is zero. In the ideal case, where resistive losses are moderate, I_{sc} and the I_{photo} are identical. Therefore, the short-circuit current is the largest current which can be drawn from the solar cell.

Open-circuit voltage and short-circuit current are depicted in Figure 2.6 which exemplarily shows the *IV*-characteristic of an illuminated solar cell. The maximum power point MPP is the point where the product of I and V, or rather power P, of the solar cell is at its maximum. The efficiency is then defined by $\eta = P_{MPP}/P_i$ with P_i as the power of the incident light. As a measure of the charge carrier collection efficiency the fill factor *FF* is derived from the ratio of the maximum power delivered by the solar

cell and the product of V_{oc} and I_{sc}: $FF = P_{MPP}/(V_{oc}I_{sc})$. Graphically it is the ratio of the rectangles given by the straight and dotted line in Figure 2.6, respectively.

The short-circuit current I_{sc} depends among others on the spectrum of the incident light, the number of photons and the active cell area. Therefore, the measurements are carried out under standard conditions to compare the values of different solar cells. Generally, at a constant temperature of 25°C a solar cell with an active area of 1×1 cm² is illuminated by a spectrum close to the AM1.5 and a power density of 100 mW/cm². An explanation of the AM1.5 spectrum will be given in subsection 2.3.7.

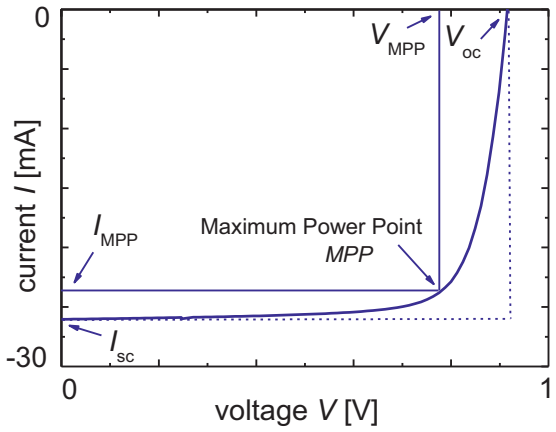

Figure 2.6 Current-voltage-(IV-)characteristic of a solar cell, indicating MPP, J_{sc}, V_{oc} and the derivation of FF

2.1.4 Amorphous and microcrystalline tandem cells

Since the light absorption of a particular material appears only in a certain wavelength range a big part of the solar spectrum cannot be used and is lost for a single junction solar cell. First, photons with energies less than the band gap do not contribute to charge carrier generation and second, all the photon energy exceeding the band gap is lost and causes thermalization. For a better use of the solar spectrum a-Si:H and µc-Si:H single junction cells are combined in a tandem cell. Each photon is guided into the

absorber layer where the band gap matches the photon energy. Hence, the solar spectrum is used more efficiently and losses by thermalization are reduced [25].

Based on this idea multijunction cells with three or more absorber layers with different band gaps can be stacked on top of each other using the light spectrum more efficiently.

The sequence of the absorber layers in multijunction cells is chosen in a way that the incident light first reaches materials with the higher band gaps. Accordingly, a-Si:H is used as top cell material where high energetic light in the wavelength region between 400 – 600 nm and a low penetration depth is absorbed. The transmitted infrared light is led to the bottom cell with μc-Si:H as absorber. A ZnO:Al/Ag layer stack reflects light that is not absorbed during the first pass through the cell back into the absorber layers so that the effective light path in the absorber material is enhanced.

Electrical connection of the subcells The subcells are electrically connected in series by the so-called tunnel recombination junction. Since the voltages must have the same sign the orientation of the p-type doped layers have to face the same direction. Consequently, the n-type layer of the top cell is adjacent to the p-type layer of the bottom cell [25]. Electrons from the n-type doped layer and holes from the p-type doped layer need to recombine at the interface. To allow recombination the Fermi level of the n-type layer of the top cell and the p-type layer of the bottom cell must be very close to the conduction and valence band, respectively, as it can be seen in Figure 2.7. The recombination process is trap-assisted which means that the charge carriers tunnel within the junction, and are trapped by defects where recombination can take place. A sufficiently high defect density is therefore required in the mid-gap to maintain a high recombination rate. More details are given in subsection 4.5.1.

Due to the series connection of the two subcells the top and bottom cell voltages V_{top} and V_{bot} for each current value sum up to the total voltage V assuming that no losses at the tunnel recombination junction occur.

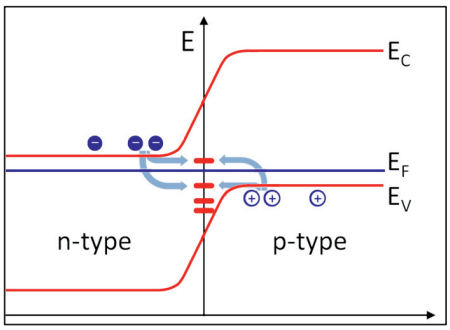

Figure 2.7 Band diagram of a tunnel recombination junction in a tandem cell

Current matching Both subcells need to provide similar or, ideally, the same number of charge carriers to allow each hole to recombine with an electron. If this is not possible because one subcell provides more charge carriers at the tunnel recombination junction than the other one, an electric field arises along the junction [46; 47]. The total current through the tandem cell is limited by the subcell that delivers the lower current due to the series connection. In case of top cell limitation (TCL) the short-circuit current generated in the top cell is lower than the bottom cell short-circuit current. Accordingly, bottom cell limitation (BCL) occurs when the bottom cell short-circuit current is lower than the top cell short-circuit current.

Generally, a slight bottom cell limitation in the initial state is preferred and leads to a matched device after light-induced degradation.

2.1.5 Radio Frequency Plasma-Enhanced Chemical Vapour Deposition (RF-PECVD)

Several methods can be used to deposit amorphous and microcrystalline silicon such as reactive sputtering, electron beam evaporation, Photo-CVD, spontaneous chemical vapour deposition, Electron Cyclotron Resonance (ECR) microwave deposition, Pulsed Laser Deposition (PLD) or gas jet deposition [27]. However, most of these techniques are not well developed yet and achieve material properties that cannot be used for photovoltaic production.

The most common deposition methods are Plasma-Enhanced Chemical Vapour Deposition (PECVD) at various frequencies and Hot-Wire Chemical Vapour Deposition (HWCVD), yielding device-quality a-Si:H and µc-Si:H. In the following the PECVD system and process will be described exemplarily by means of the system that was used for this work.

PECVD system Figure 2.8 illustrates the basic setup of the used PECVD system. Two parallel electrode plates are located in a vacuum chamber that achieves a base pressure $< 5 \times 10^{-7}$ Torr. The RF-power is supplied at the electrode where also the gas inlet is realized via a showerhead. The carrier that holds the substrate serves as grounded electrode and is placed in front of a heater opposite to the powered electrode.

The power produced by an RF-generator is capacitively coupled to the former electrode via a matchbox, which consists of an inductive coil (L) and two variable capacitors (C_1, C_2). Their capacities are automatically adjusted such that the impedance of the matchbox matches the impedance of the plasma at any time.

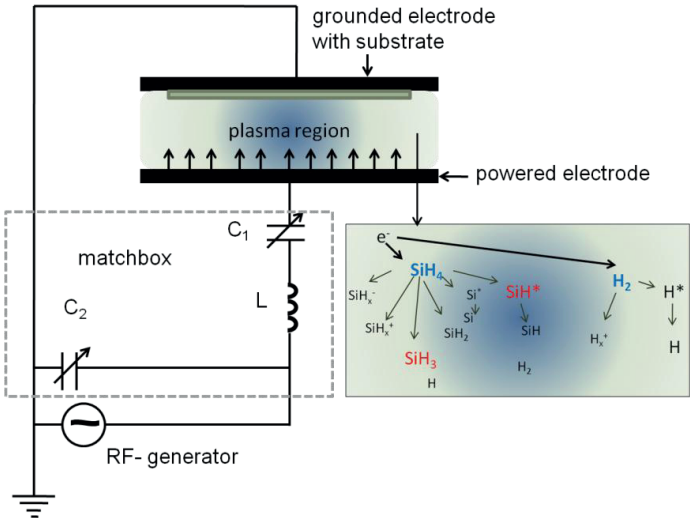

Figure 2.8 Capacitive plasma excitation between the powered and grounded electrode by an RF-field and dissociation processes in the silane/hydrogen gas mixture

Deposition process The process gas mixture is fed between the two electrodes through a showerhead electrode. By applying an alternating (RF)-electric field to the electrode plates some of the few present electrons are accelerated and collide with silane (SiH_4) and hydrogen (H_2) molecules. Both gases dissociate and release electrons that are also accelerated in the RF-field and ionize the gas further; collision ionization occurs. Long- and short-living radicals and ions are formed as is can be seen in Figure 2.8. The short-living radicals $^{\bullet}SiH_2$, $^{\bullet}SiH$ and $^{\bullet}Si$ react with SiH_4 as follows [23]:

$$^{\bullet}SiH_2+SiH_4 \rightarrow Si_2H_6 \text{ or } SiH_3+SiH_3$$
$$^{\bullet}SiH+SiH_4 \rightarrow SiH_2+SiH_3$$
$$^{\bullet}Si+SiH_4 \rightarrow SiH+SiH_3.$$

The fragment SiH_3 shows no reactivity with SiH_4 and is regarded as the main precursor for the film growth [23; 32]. Excited particles such as Si* and SiH* cause a characteristic refulgence when they return to a lower energy level which can be used for plasma diagnostics, e.g., by Optical Emission Spectroscopy (OES). The precursor deposit on the heated substrate and the layer starts to grow as it was described previously in subsection 2.1.1 and subsection 2.1.2. Besides SiH_3 the presence of atomic hydrogen is important for the film growth [40]. A high hydrogen dilution is necessary to deposit µc-Si:H since the hydrogen plasma etches week and twisted bonds. However, only a small amount is built into the layer so that the hydrogen content of intrinsic µc-Si:H layers is usually 3 – 8% [44].

Optimized process settings For the growth of amorphous silicon the deposition pressure is usually set between 0.05 Torr and 3 Torr. Lower pressure leads to uniform film growth whereas high process pressures up to 10 Torr are preferred for microcrystalline growth [27]. A higher RF-power leads to an increase in deposition rates but also in powder formation that deteriorates the layer quality. By depositing at low pressure and with low silane concentration powder formation can be avoided. Problematic is also the standing wave effect which can cause an inhomogeneous voltage distribution on the substrate and, therefore, inhomogeneous layer growth especially on

large substrates [48]. Generally, the substrate temperature lies between 160°C and 250°C. At lower temperatures, more hydrogen is incorporated into amorphous silicon, which influences the band gap [29]. At higher temperatures, the surface diffusivity is enhanced and the amorphous network becomes more ideal and less hydrogen is bonded [27]. Regarding the surface diffusivity the same applies for the growth of µc-Si:H: a higher deposition temperature first leads to an increasing crystallinity. However, above a certain temperature the crystallinity decreases due to a thermal desorption of hydrogen [32].

The electrode gap is usually between 6 – 25 mm. Narrower gaps allow for uniform depositions whereas maintaining the plasma is easier with wider electrode gaps.

Whether a layer grows amorphous or microcrystalline is very sensitive to the silane concentration *SC* defined by $SC = Q_{\mathrm{SiH_4}}/(Q_{\mathrm{SiH_4}} + Q_{\mathrm{H_2}})$ with $Q_{\mathrm{SiH_4}}$ and $Q_{\mathrm{H_2}}$ as the gas flow rates of silane and hydrogen, respectively.

For device-quality a-Si:H and µc-Si:H layers the deposition regime has to be adjusted thoroughly for certain chamber setups. Since the parameters influence each other, an optimum has to be found. Generally, a-Si:H is deposited at lower pressure and power but higher silane concentration compared to µc-Si:H.

2.2 Sample preparation

In the following section, the material and solar cell preparation is described. The main parameters for the doped and intrinsic amorphous and microcrystalline layers are given.

2.2.1 Substrate treatment

Commercially available, SnO_2:F-coated substrates with a pyramidal texture (Asahi U) were used for the deposition of amorphous single junction solar cells as well as for tandem solar cells. Single layers for material investigations were deposited on Corning Glass to avoid influences of the textured and conductive SnO_2:F. To ensure a residue-free surface both substrate types were cleaned by DeContam® and an

additionally applied ultrasonic bath for about 2 h. Subsequently, they were rinsed with deionized water in an overflow basin until the conductance due to residues was sufficiently low. Finally, the substrates were dried by a spin dryer.

Microcrystalline single junction solar cells and layer stacks were deposited on ZnO:Al substrates prepared at IEF5. To enhance the light path in the solar cells a certain roughness of the surface is preferable. Therefore, the ZnO:Al layers sputtered on Corning Glass were etched for 30 – 40 s in a 0.5% HCl solution which leaves a crater-like texture on the surface.

2.2.2 Silicon deposition

Amorphous and microcrystalline intrinsic and doped layers were deposited in a large area RF-PECVD system that is suitable for four 10 × 10 cm² substrates or one 30 × 30 cm² substrate. Figure 2.9 illustrates the PECVD system and its main components. All layers were deposited with an excitation frequency of 13.56 MHz. The electrode gap for PC1 (Process Chamber) and PC3 was 12.5 mm.

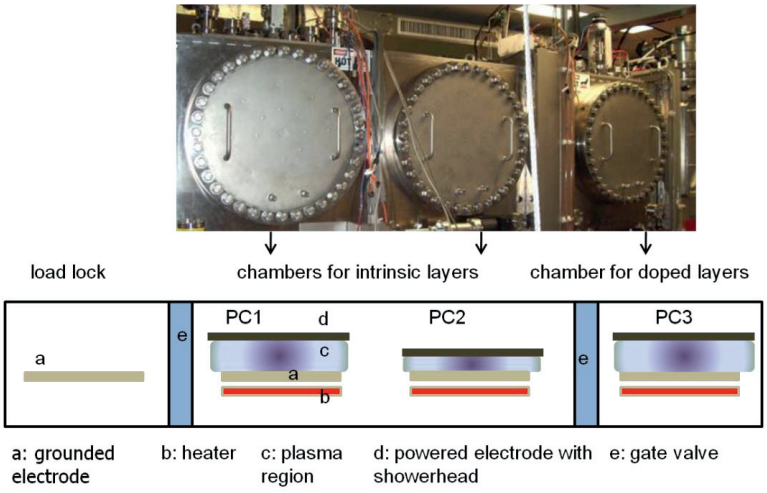

Figure 2.9 Scheme of the used large area PECVD system

The substrates were placed into the load lock and transferred to PC3. After a heating up time of 30 min the process gas was let into the chamber. The p-type doping was realized by adding Trimethylborane (TMB, $(CH_3)_3B$) diluted in H_2 to the SiH_4/H_2-mixture. For amorphous p-type doped layers also methane (CH_4) was used to widen the band gap. After the deposition, an Ar-purge was applied to prevent cross-contamination when the substrate holder is transferred to the intrinsic chamber PC1 where the amorphous or microcrystalline intrinsic layers were deposited. The deposition of an a-Si:H i-layer started with a highly hydrogen diluted buffer layer which had proven of value to achieve an increase in open-circuit voltage [22]. Finally, the substrates were transferred back to PC3 for the n-type doped layer deposition. Hydrogen diluted Phosphine (phosphorus trihydride, PH_3) was used as dopand. All cells were equipped with a low-conductive a-Si:H n-layer to avoid carrier collection from outside the defined active area.

For tandem cells a µc-Si:H n-doped layer was deposited after the a-Si:H n-doped layer followed by a µc-Si:H p-doped layer. The use of µc-Si:H doped layers is necessary to reach a high conductivity in the tunnel recombination junction. The amorphous n-layer is used to protect the a-Si:H i-layer from being etched by the high hydrogen containing plasma used for the µc-Si:H n-layer. An argon purge was applied after the µc-Si:H n-layer and the chamber was pumped down to a base pressure below 5×10^{-7} Torr before the µc-Si:H p-doped layer was deposited. The second absorber layer and the final a-Si:H n-layer were prepared in the same manner as for the top cell and completed the tandem cell.

2.2.3 Back contact

After the silicon deposition, the samples cooled for about 30 min in the load lock and were then taken out. All tandem cells and many of the single junction cells were equipped with a sputtered ZnO:Al layer as back reflector. Subsequently, Ag pads and grids were evaporated through a shadow mask defining an active cell area of 1×1 cm². Uncovered ZnO:Al was etched off by using a 0.25% HCl-solution. The sample

preparation was finished by an annealing step at 160°C for about 30 min at ambient atmosphere.

2.3 Material and solar cell characterization methods

2.3.1 Dark and photoconductivity

The conductivity of intrinsic material in the dark (dark conductivity) results from charge carriers in defect states that are thermally activated. By illuminating the sample with light, the conductivity increases due to photogenerated charge carriers. Consequently, the photosensitivity, which is the ratio of photoconductivity to dark conductivity, is a measure of how many charge carriers can be generated by light. A high photosensitivity is preferred for photovoltaic application. Values of ~ 10^6 are typical for device-grade a-Si:H material.

The intrinsic layers were deposited on Corning Glass without TCO or a conducting p-doped layer. To enhance the adhesion of the silicon layer the Corning Glass was roughened by applying a treatment with argon plasma.

Silver contacts were evaporated onto the layers which were then placed into a vacuum tube and annealed for 30 min at ~ 160°C. The current measurements were carried out at room temperature by applying voltages from -100 V to 100 V. As the contact geometry and the thickness are known the conductivity σ can be determined by:

$$\sigma(V) = j/E = bI/(dlV) \tag{2.4}$$

with, b as distance between the contacts, I as the measured current, l as the width of the contacts, d as layer thickness and V as the applied voltage. For the photoconductivity measurements the samples were illuminated by a halogen lamp.

2.3.2 Optical spectroscopy

Optical properties like transmittance or reflectivity of the used substrates and fabricated solar cells were measured with a Perkin Elmer Lambda 950 spectrometer,

which covers a wavelength range from 250 nm to 2500 nm. In the ultraviolet (UV) wavelength region the irradiation is realized by a deuterium lamp whereas in the visible (Vis) and infrared (IR) region a tungsten-halogen lamp is used. At $\lambda = 860$ nm the detector changes due to the corresponding spectral sensitivity which causes artefacts in the measured spectra. Further details about the measuring setup and the routine can be found elsewhere [49].

From the ratio of diffuse to total transmittance, the haze is derived which is often used as a quality feature for glass-based, TCO-covered substrates. With the help of the reflectivity of the solar cell pads and additional external quantum efficiency measurements, the parasitic absorption and internal quantum efficiency are accessible. Diffuse and total reflectivity are used to evaluate non-transparent substrates for n-i-p solar cells.

2.3.3 Photothermal Deflection Spectroscopy

Photothermal Deflection Spectroscopy (PDS) is a method to measure the optical absorption of materials, which is especially sensitive in the sub band gap region. The investigated layers were deposited on Corning Glass that underwent an argon treatment to roughen the surface. Typical absorption spectra of μc-Si:H and a-Si:H were shown in Figure 2.3 from which the band gap energy, e.g., E_T or E_{04} can be derived.

The basic effect, on which this high-sensitivity spectroscopy technique is based, is the change in refractive index due to the heating of matter adjacent to the sample surface.

In Figure 2.10 the transverse PDS setup is schematically shown: Monochromatic light strikes the sample normal to its surface which is surrounded by the inert and non-absorbing deflection medium carbon tetrachloride (CCl_4) with a highly temperature dependent refractive index. A fraction of the energy of the incident light is absorbed by the investigated material and converted into thermal energy [50]. Sample heating is a direct consequence of optical absorption. Thus, photothermal spectroscopy signals are directly dependent on light absorption [51]. The temperature increase in the sample results in a temperature increase in the adjacent fluid and leads to a change in its density

and, hence, refractive index. The latter causes a temperature-dependent deflection of the probe laser beam that runs parallel to the sample surface. The spectral dependency of the absorption in the sample is determined by relating the deflection of the probe laser beam, detected by a position sensor, relative to the incident light with a certain wavelength that is measured by a reference detector. To enhance the Signal-to-Noise-Ratio the incident light beam is chopped and the deflection is measured by a lock-in amplifier.

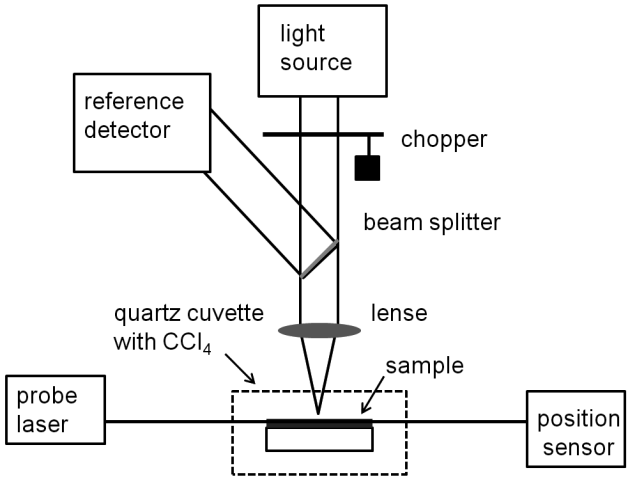

Figure 2.10 Scheme of PDS setup for measurements in transverse geometry

2.3.4 Layer thickness determination

To measure the thickness of the deposited layers and cells the silicon layer at two adjacent spots was ablated by means of a laser [52]. The wavelength of the laser is chosen in a way that only silicon is removed; substrate and TCO remain unchanged. The needle of a profilometer (Dektak 3030 Veeco Instruments Inc.) moves over the sample surface and the engraved spots without silicon. Simultaneously, the instrument displays the height profile and the difference between surface and bottom of the cavity gives the silicon thickness.

2.3.5 Raman spectroscopy

By means of Raman spectroscopy the crystallinity of different µc-Si:H layers was investigated. For a thickness dependent crystallinity examination microscopic Raman measurements were carried out at an etch crater whereas layer stacks were usually investigated with the near backscattering setup. Both configurations are described in the following and the data evaluation is explained.

Raman effect When monochromatic light interacts with matter scattering on molecules and atoms occurs. Most of the incident light is scattered elastically by Rayleigh scattering so that the wave numbers $\bar{\nu}_0$ of the incident and scattered light are identical. Besides the Rayleigh scattering also so-called Stokes and Anti-Stokes processes occur. The Stokes process describes the excitation of oscillations with a wave number $\bar{\nu}_{vib}$ in the molecules due to the impact of light. The molecule gains energy that is lost for the incident light. Consequently, the scattered light has a wave number that is reduced by $\bar{\nu}_{vib}$ relative to the incident light with a wave number $\bar{\nu}_0$. In the Raman spectrum, the Stokes line appears at $\bar{\nu}_0 - \bar{\nu}_{vib}$.

The Anti-Stoke line results from an energy gain of the scattered light, which is transferred from molecules that oscillate with $\bar{\nu}_{vib}$. Consequently, the wave number of the scattered light increases by $\bar{\nu}_{vib}$ and the Anti-Stokes line appears at a higher wave number in the Raman spectrum [53]. Since this energy gain is only possible when the molecules are in an excited state, and most molecules are in ground state at room temperature, the Anti-Stokes process is rather rare leading to a lower intensity in the Raman spectrum compared to the Stokes line. Figure 2.11 displays schematically a Raman spectrum with the Rayleigh line at $\bar{\nu}_0$, the Stokes line at lower wave number $\bar{\nu}_{Stokes} = \bar{\nu}_0 - \bar{\nu}_{vib}$ and Anti-Stokes lines at higher wave numbers $\bar{\nu}_{Anti\text{-}Stokes} = \bar{\nu}_0 + \bar{\nu}_{vib}$.

Due to the periodicity of a crystal and its translation symmetry, only certain phonons with $\bar{\nu}_{vib}$ are allowed so that Raman scattering can only appear at certain wave numbers. In amorphous materials, the translation symmetry is lost and no selection rule for allowed and forbidden phonon transitions applies. Hence, no discrete lines, but a broad band is observed in the Raman spectrum.

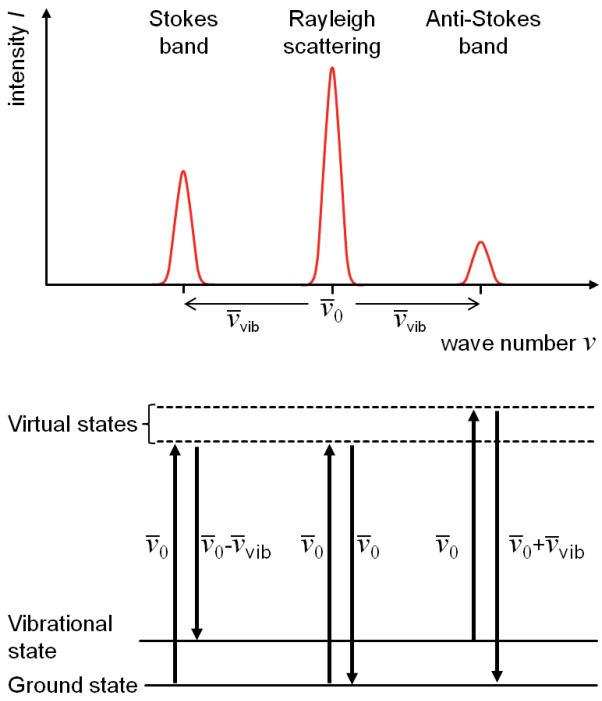

Figure 2.11 Scheme of Raman spectrum and related energy transitions

Near backscattering setup for Raman measurements In general, Raman measurements were carried out in the near backscattering configuration shown in Figure 2.12 where the laser beam strikes the sample under an angle of 60°. The Raman scattered light, which distributes isotropically from the sample surface, is detected by a spectrometer that is arranged outside the directly reflected radiation. Hence, reflected light does not interfere with the measuring signal.

A beam cleaning optic ensured that influences of plasma lines of the exciting laser are excluded. A notch filter reduces the intensity of the Rayleigh scattering which is necessary because the wavelengths of the Raman shifted radiation are very close to the exciting radiation and, thus, to the elastically scattered Rayleigh light. The high intensity of the latter would obscure the signal referring to the Stokes and Anti-Stokes process.

Two excitation lasers with wavelengths of 488 nm and 647 nm were used to probe the µc-Si:H in different depths.

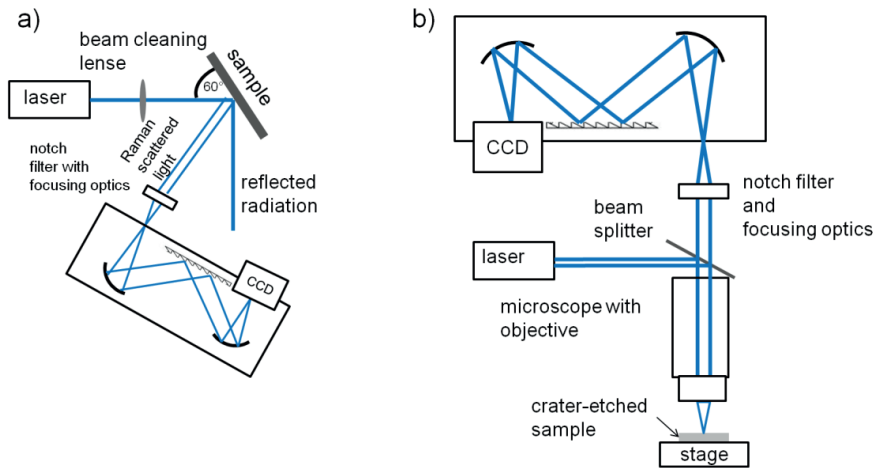

Figure 2.12 a) Sketch of near backscattering Raman measuring setup used for conventional crystallinity determination b) Sketch of microscopic Raman measurement setup used for the investigation of the crater-etched samples

Setup for microscopic Raman measurements For Raman measurement along a wedge-shaped etch crater microscopic Raman was applied. A scheme of the setup is shown in Figure 2.12 b). By using an Olympus BX 51 microscope with a magnification of 50 and numerical aperture of 0.8 the resulting spot size was in the order of 1 µm. Special care was taken to prevent a significant heating of the thin µc-Si:H layers to avoid unintended crystallization and a shift of the Raman peak. The scattered Raman light was analyzed with a liquid nitrogen cooled Photometrics CCD attached to a Horiba Spex 270M Monochromator. The spectral resolution was around 1.3 cm^{-1}.

Etching procedure for depth resolved Raman measurements For depth resolved Raman measurements as they were carried out in section 6.6 a well-defined crater was etched into each layer with the help of a flow cell. As etching agent 4 mol/l concentrated potassium hydroxide (KOH) was used. The design of the flow cell made it

possible to etch well-defined craters into the silicon layers whose depth gradient was measured by a profilometer. With the help of microscope images of the craters, it was possible to estimate the depth of the spots at which Raman measurements were carried out. Since the etched crater is not smooth, a small lateral shift can cause a rather big shift in depth. This has to be taken in consideration.

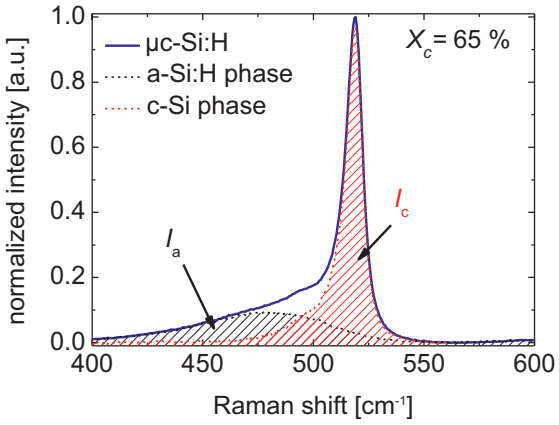

Figure 2.13 Raman spectrum of a µc-Si:H layer. The amorphous and crystalline phase contributions are given by hatched areas.

Data evaluation The Raman data were evaluated with the help of an amorphous silicon reference spectrum measured with the according laser wavelength. First, a baseline was subtracted from the measured spectrum in the range of 400 – 560 cm^{-1}. Second, the intensity of the spectrum was normalized to its maximum. The amorphous reference spectrum was then scaled by a factor so that the slope in the wave number region between 400 cm^{-1} and 450 cm^{-1} matched the measured spectrum. Subsequently, the scaled amorphous spectrum is subtracted from the measured spectrum in the range of 400 – 560 cm^{-1}. The remaining crystalline fraction is integrated and the crystalline volume fraction X_c^{Raman} is calculated by:

$$X_c^{Raman} = I_c/(I_c+I_a). \tag{2.5}$$

Figure 2.13 shows exemplarily a fit of a microcrystalline silicon Raman spectrum. The hatched areas refer to the crystalline and amorphous phase, I_c and I_a, as indicated.

2.3.6 X-ray diffraction

In general, X-ray diffraction (XRD) measurements detect the scattering intensity of radiation on electrons. The positions of the intensity maxima are related to local atomic distances. The intensities are a result of constructive interferences of X-rays with the wavelength λ that are scattered at adjacent lattice planes. If the latter have a consistent distance d an angle θ between the plane and the X-ray exists for which the path length difference of the scattered X-rays equal a multiple integer n of the X-ray wavelength. Bragg's law describes this relation by:

$$2d\sin\theta = n\lambda. \tag{2.6}$$

Therefore, information about micro- and macroscopic structure can be gained, including the existence of long-range and medium-range order in microcrystalline and transition-close amorphous silicon.

X-ray diffractometer The XRD measurements were performed by a Bruker D8 Advance X-Ray diffractometer. The Cu_{K_α} radiation with a wavelength of 1.54 Å was generated by a tube power of 40 mA/40 kV. A parabolically curved multilayer mirror (so-called Göbel mirror) was used to convert divergent radiation emerging from an X-ray source into a parallel beam according to Figure 2.14. Consequently, the probing X-rays irradiate a wider area.

A parallel plate collimator (PPC) is applied on the secondary side. This module defines the acceptance angle of the diffracted beam seen by the detector. The PPC consists of a set of parallel plates perpendicular to the diffraction plane. The distance between the plates defines the acceptance angle of the collimator, here 0.24°. Figure 2.15 illustrates the whole configuration that was applied for the Grazing Incident and Bragg-Brentano XRD measurements. An energy dispersive Sol-X was used as detector. It met the requirements for a large X-Ray active area as well as for an energy resolution

to separate Cu_{K_β} from Cu_{K_α} simultaneously (Bruker AXS Specification Sheets 2010). Shorter measurement times and a low background signal were so realized.

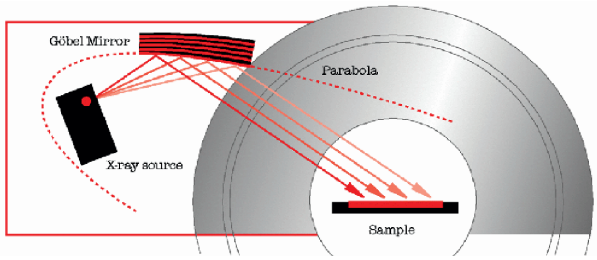

Figure 2.14 Göbel mirror: the X-ray is adjusted to the focus of the parabola of the multilayered Göbel mirror resulting in parallel reflected beams [54].

Bragg-Brentano geometry The Bragg-Brentano (BB) geometry or θ/2θ-scan is the basic measurement setup in XRD analysis and the most commonly used one. It is mainly applied for random oriented powders but also thin films can be investigated, especially polycrystalline films on flat substrates.

The angle θ defines the angle between incoming beam and sample surface and correspondingly between exiting beam and sample surface. During the measurement the incident angle θ and the scattered angle 2θ are varied and the scattered intensity $I(2\theta)$ is recorded as a function of 2θ. It is important to note that the scattering vector is always normal to the surface of the sample and, consequently, only lattice planes oriented parallel to the substrate are detected; tilted crystals are not considered.

When measuring thin films it has to be taken into consideration that the X-Rays fully penetrate the whole probing volume of the thin sample. Underlying material contributes to the diffractogram making the data analysis more difficult.

Grazing Incidence geometry Especially for analyzing very thin films for which the penetration depth of the X-rays exceed the layer thickness by far, Grazing Incidence X-ray diffraction (GI-XRD) measurements are more advantageous compared to the conventional Bragg-Brentano geometry. The sample is irradiated under a very small

angle, which ensures that the structural information stems from the probed thin film and a contribution of underlying material is at least reduced or excluded.

In Figure 2.15 shows the incident angle under which the X-ray penetrates into the thin-film sample. During the measurement α is kept constant. A diffractogram is recorded by moving the detector along the 2θ-circle. The Bragg reflections appear at nearly the same position as in the Bragg-Brentano scans.

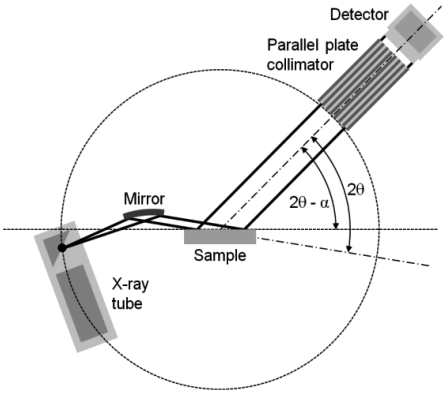

Figure 2.15 Used diffractometer configuration with parallel beam optics. The plane of the figure is the scattering plane and angle α refers to the incident angle.

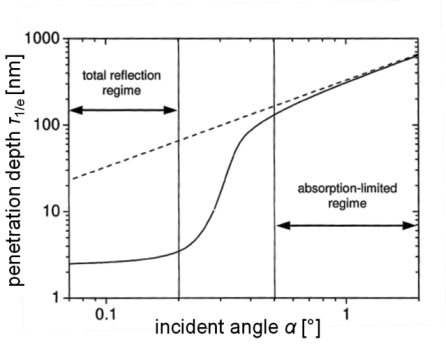

Figure 2.16 The penetration depth $\tau_{1/e}$ is shown as a function of the incident angle α on a double-logarithmic scale (exemplarily shown for a TiO_2 thin film). The dashed line gives the penetration limit derived from equation 2.7 [54].

For the asymmetric Grazing Incidence geometry, the scattering vector changes its orientation continuously throughout the measurement and with it also the orientation of the reflecting lattice planes. For randomly oriented samples, no difference between GI and BB diffractograms is expected. Samples for which the structural properties depend on thickness and orientation the different tilt of grain agglomerates, as it is the case in μc-Si:H, has to be taken into consideration for the interpretation of GI measurements [54].

Penetration depth The penetration depth of the X-rays is shown in Figure 2.16 as a function of the incident angle on a double-logarithmic scale (for a TiO_2 thin film that serves as example). Three different regimes can be seen: Below a critical angle α_c total reflection occurs and the penetration depth is nearly constant. When α increases above α_c the penetration depth increases and approaches the limit described by:

$$\tau_{1/e} = \frac{\sin\theta}{\mu} \tag{2.7}$$

with μ as the linear attenuation coefficient. When varying angles in the vicinity of α_c, the sample is probed in depths that can differ in orders of magnitude whereas for higher incident angles the change in penetration depth with α is far less pronounced [54]. To calculate the penetration depth it is therefore crucial to determine the incident angle exactly, which was not possible in the used diffractometer. When mounting the sample slight tilts of the sample could not be excluded so that an offset for α occurred. Therefore, suitable angles had to be determined prior the GI-XRD measurements.

Measuring routine Grazing Incidence XRD Before a GI-XRD scan was performed, it was necessary to determine suitable incident angles. This was done by running an omega-scan at the position where the most intense reflection of cubic silicon (the {111} peak at 28.44°), and also a high signal of the amorphous phase appear. The incident angle α is varied between - 0.2° and 1.8°. As it can be seen in Figure 2.17, from a certain α on an increasing diffraction intensity is recorded indicating that the X-ray starts to penetrate into the µc-Si:H layer. A region with linear increase appears in a logarithmic plot, emphasized by the red line in Figure 2.17. In this region, appropriate incident angles above the critical angle α_c are found. For a further increase of α, the signal intensity saturates because the X-rays already probed the whole layer and start to penetrate into the glass substrate. No intensity increase is possible. The scheme in Figure 2.18 illustrates the penetration of the X-ray for different incident angles. In case a) the incident angle is too small: total reflection at the surface occurs. For case b) α is appropriate since the X-ray penetrates deep into the sample, whereas in case c) it is too

large and an undesired contribution of the glass substrate is recorded which makes the quantitative analysis more complicated.

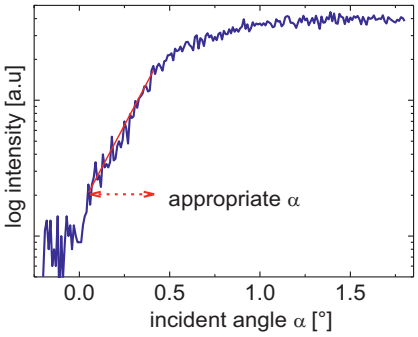

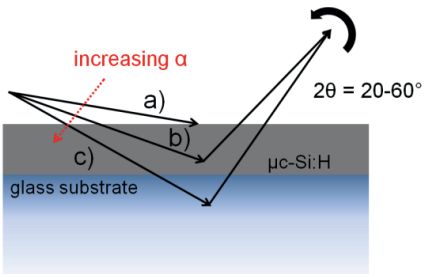

Figure 2.17 Omega-scan for α-determination *Figure 2.18 Scheme of Grazing Incidence XRD*

After a suitable incident angle was chosen, a detector scan was carried out in a range of 2θ = 20°– 60° for which α was kept constant and the detector moved around the sample. In the ideal case the X-ray penetrates into the µc-Si:H layer probing a large volume without reaching the glass substrate.

A small step width between 0.02° and 0.05° and long integration times of 100 s/step up to 120 s/step were chosen for the measurements to ensure a good Signal-to-Noise-Ratio (SNR).

Data evaluation Grazing Incidence XRD The diffractograms of µc-Si:H were evaluated by Diffrac^{plus} Topas 4 which is a graphics-based software application, e.g., for profile analysis. First, as reference, Grazing Incidence XRD was performed on standard amorphous silicon deposited on a chromium-covered glass. The chromium hindered the X-ray to penetrate into the glass substrate and, thus, a diffractogram of a-Si:H and chromium was obtained. Due to short and medium range order also amorphous silicon shows diffracted intensities in XRD measurements which are located as broad humps at ~ 27.6° and at ~ 51° [55].

Figure 2.19 depicts a diffractogram of a µc-Si:H layer and an a-Si:H reference used for the fitting procedure. The background caused by Compton scattering was simulated by a superposition of a Chebychev polynomial of 1st order and a 1/x-function which is

then subtracted from the measured diffractogram. The reflections were fitted with Pseudo-Voigt profiles that are a combination of Gaussian and Lorentz profiles.

In Figure 2.19, the Pseudo-Voigt profiles that were used to describe the amorphous phase are shown by the dashed curves. The parameters gained from this fit such as position, full width at half maximum (FWHM) and integrated intensity ratio of the first and second diffraction peak were used to fit the amorphous phase in µc-Si:H diffractograms.

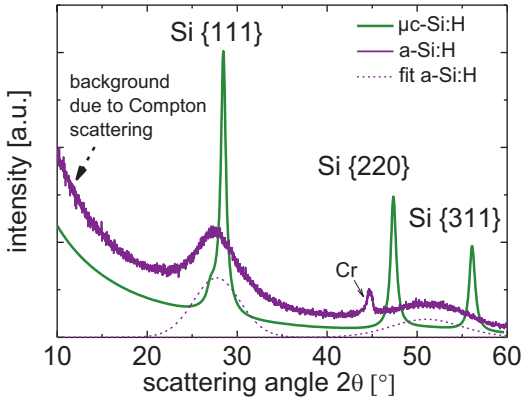

Figure 2.19 Diffractograms of standard a-Si:H, deposited on Cr-covered glass, and highly crystalline silicon. The dashed curves depict the Pseudo-Voigt profiles used for the fitting procedure of the amorphous background.

The Bragg reflections of the cubic crystalline phase at 28.44°, 47.3° and 56.12°, corresponding to the {111}, {220} and {311} reflections, and the often appearing reflection from the hexagonal phase at ~ 27°, were fitted by Pseudo-Voigt profiles. With I as the integrated intensity of the according peak the crystalline volume fraction X_c^{XRD} is calculated by:

$$X_c^{XRD} = I_c/(I_c + I_a) \tag{2.8}$$

with

$$I_c = I_{111}+I_{220}+I_{311}+I_{hex} \tag{2.9}$$

and

$$I_a = I_{27.6°} + I_{51°}. \tag{2.10}$$

Measuring routine Bragg-Brentano XRD The Bragg-Brentano diffractograms were recorded directly after the GI measurements so that the sample mounting was the same and the illuminated area similar. The scanned range, step width and integration time were identical to the GI measurements for one sample, but could slightly vary from sample to sample. In the Bragg-Brentano setup the X-ray penetrates the whole sample, including the substrate and the ZnO:Al layer. The latter one is strongly textured leading to an intense peak. Due to the necessary high integration times and small step widths, the ZnO:Al intensity would have damaged the energy dispersive detector seriously. Therefore, the measurements were stopped right before the ZnO:Al reflection at ~ 34° and resumed at ~ 36°.

Data evaluation Bragg-Brentano XRD The Bragg-Brentano diffractograms were fitted in the same manner as the Grazing Incidence XRD diffractograms. Additionally, the glass substrate had to be considered giving a broad hump at ~ 25°. Therefore, a reference diffractogram of pure glass was recorded and fitted, and used to describe the glass contribution to the diffracted intensity. The crystalline volume fraction was calculated from the amorphous and crystalline integrated intensities as shown before.

2.3.7 Measurement of solar cell parameters

In subsection 2.1.3 the four solar cell parameters efficiency, fill factor, open-circuit voltage and short-circuit current density were introduced. In the following, the measuring setup and procedure is described.

In order to compare the performance of different solar cells under illumination standard testing conditions (STC) had been defined. Since temperature and irradiance influence the J_{sc} and V_{oc} strongly, it was appointed to measure solar cells at a temperature of 25°C and with an irradiance of 100 mW/cm². Additionally, it is crucial to define the spectrum with which the solar cells are investigated. The used AM1.5

spectrum describes the solar spectrum that reaches the earth after travelling through the atmosphere. The number “1.5” indicates how much air mass in respect to perpendicular irradiation the sunlight has to pass before reaching the earth’s surface as it can be seen in Figure 2.20. The AM1.5 spectrum is very close to the sun spectrum found in Europe.

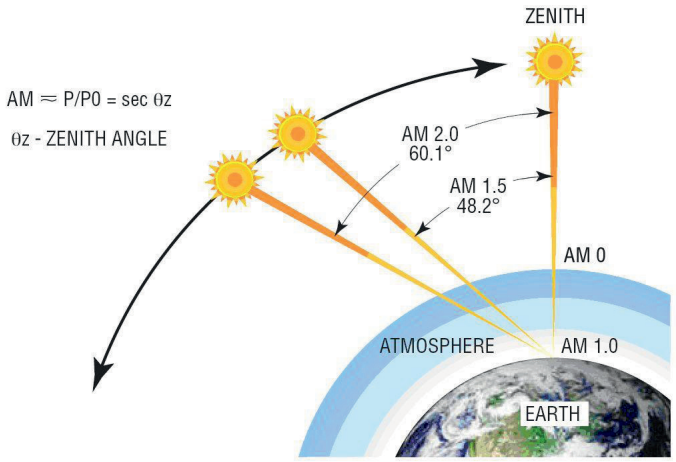

Figure 2.20 The definition of various global air mass (AM) conditions [by Newport]

The photovoltaic parameters were measured with a class A solar simulator of the type WACOM-WXS-140S-Super. The solar simulator was calibrated with a Hamamatsu photodiode S1336-BQ before the measurements. The solar cell was mounted on a copper block which was connected to an electrical heating and water cooling system to ensure a constant temperature of 25 ±1°C. To improve the electrical and thermal contact a suction device was used to fix the solar cell. Gold-coated metallic pins contacted all 18 solar cell pads with the size of 1×1 cm² at the same time from underneath the sample. A xenon and a halogen lamp are used in combination to achieve a spectrum very close to the AM1.5 spectrum with a irradiance intensity of 100 mW/cm².

The measurement of the photovoltaic parameters was carried out by means of a computer-controlled voltage source with the possibility to measure the current response (SMU 238, Keithley). The applied voltage varied from -0.5 V up to a value close to the

expected open-circuit voltage. The upper limit was set to 1.5 V for tandem solar cells, 1 V for a-Si:H single junction cells and μc-Si:H were measured up to 0.6 V. The photovoltaic parameters η, *FF*, V_{oc} and J_{sc} were automatically calculated by a measuring program.

2.3.8 External quantum efficiency

By means of solar simulator measurements, the performance of the solar cells over the completely integrated wavelength range is observed. Quantum efficiency measurements evaluate the solar cell performance as a function of the wavelength. By applying suitable filtered bias light the top and bottom cell of a tandem cell can be characterized separately.

Definition The external quantum efficiency *EQE* describes the probability that a photon creates an electron-hole pair in the solar cell that contributes to the current flow. It is defined as the ratio of the number of collected charge carriers (given by the photo current density $J(\lambda)$) to the number of photons that impinge the solar cell perpendicular (given by the photon flux density of the incident light $\Phi(\lambda)$) with a certain wavelength, leading to:

$$EQE(\lambda) = J(\lambda)/e\Phi(\lambda) \tag{2.11}$$

Sometimes, also the internal quantum efficiency *IQE* is of interest, which is calculated by taken the cell reflectivity in consideration:

$$IQE = EQE/(1 - R) \tag{2.12}$$

Experimental setup For the determination of the (external) quantum efficiency, first, the spectral response $S(\lambda)$ is measured by means of the Differential Spectral Response (DSR) method. The spectral response is the ratio of the generated photo current density $J(\lambda)$ to the irradiance $E_{Ph}(\lambda)$ which reaches the solar cell. With the help of a reference

photo diode for which the spectral response is known the photo current density of the solar cell is derived. The quantum efficiency is then calculated by:

$$EQE(\lambda) = S(\lambda)hc/e\lambda. \tag{2.13}$$

The short-circuit current density of the top and bottom cell is accessed:

$$J_{sc} = e \int_{\lambda_{start}}^{\lambda_{end}} EQE\,(\lambda)\cdot\Phi(\lambda)d(\lambda). \tag{2.14}$$

The measuring setup is shown in Figure 2.21. The solar cell is irradiated by monochromatic light in the wavelength region between 300 nm < λ < 1200 nm which is created by a Xe-lamp and a grated monochromator. The lock-in technique is used to increase the Signal-to-Noise-Ratio. Therefore, the incident light is modulated with a chopper frequency of 29 Hz. For a reference measurement, the light beam is divided by a beam splitter and led to a reference photo diode.

Quantum efficiency measurements on tandem cells To obtain information about the individual top and bottom cell performance of the tandem cell, bias light and bias voltage have to be applied during the measurement. When measuring the spectral response of the top cell the bottom cell is illuminated with bias light of high intensity, filtered with an OG 590 filter that transmits only light above a wavelength of 590 nm. The bottom cell is now saturated and the incident probing light causes only a spectral response of the limiting top cell. To measure the top cell in open-circuit condition, additional to the bias light a bias voltage in the range of the open-circuit voltage of the bottom cell is applied. For the top cell measurement wavelengths between 300 – 800 nm are used; the step width amounted to 10 nm.

To access the spectral response of the bottom cell the top cell is irradiated by bias light filtered with an IF 450 filter transmitting light up to a wavelength of 450 nm. The spectral response is recorded from λ ~ 400 nm to λ = 1200 nm. A bias voltage that equals roughly the open-circuit voltage of the top cell is applied.

A comparison of the short-circuit current densities of both subcells shows if the matching condition ($J_{sc,top} = J_{sc,bot}$) is fulfilled. Therefore, $J_{sc,top}$ and $J_{sc,bot}$ are calculated by integrating the quantum efficiency and the irradiance over the measured wavelength according to equation 2.14.

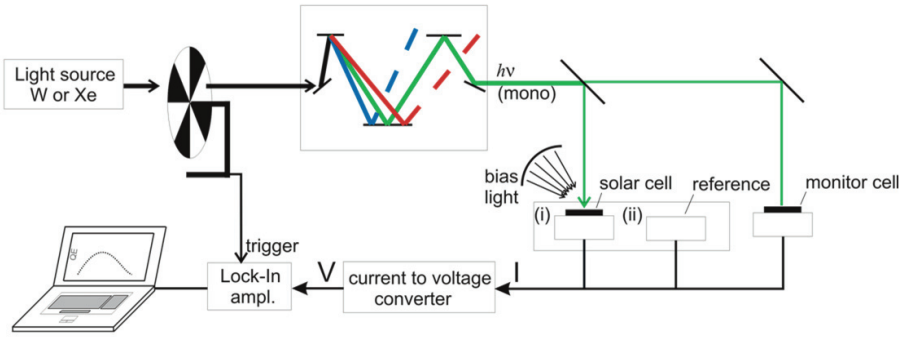

Figure 2.21 Measuring setup DSR: Xe-light modulated by a chopper is led to a grated monochromator. Reference and solar cell are irradiated simultaneously by light with a certain wavelength. Bias light and bias voltage are applied for measurements on tandem solar [56].

2.3.9 Light soaking procedure

As it was described in subsection 2.1.1, amorphous silicon suffers from light-induced degradation. Consequently, the performance of a-Si:H single junction solar cells and tandem solar cells having a-Si:H top cells decrease when they are exposed to light until a semi-stable state (stabilized) is reached. To evaluate the performance of the fabricated solar cells not the initial but stabilized performance is of interest. Therefore, most of the investigated tandem and a-Si:H single junction solar cells underwent the light soaking procedure.

Standard conditions appointed by NREL (National Renewable Energy Laboratory, USA) were used for the degradation. Accordingly, the cells were kept at open-circuit conditions and illuminated by an AM1.5 spectrum with an irradiance of 100 mW/cm² at 50°C. The light soaking was carried out for 1000 h after which the cell performance was regarded as stabilized.

Chapter 3

Thinner absorber layers in a-Si:H/µc-Si:H tandem cells

Tandem solar cells consisting of an amorphous silicon top cell and microcrystalline silicon bottom cell use the light spectrum more efficiently than single junction solar cells. In order to achieve a high power output, the absorber layers have to be sufficiently thick. Total thicknesses between ~ 1.5 – 3 µm are therefore usually applied. This chapter presents investigations on the influence of significant thinner absorber layers on the photovoltaic parameters and quantum efficiencies in tandem solar cells. Effects are discussed for a simultaneous and individual reduction of the top and bottom cell absorber layer thickness. Subsequently, the behaviour of thin and standard thick tandem cells after light-induced degradation is evaluated.

3.1 Introduction

Silicon based thin-film technologies have to face a high competition on the photovoltaic market. To enhance the attractiveness of the a-Si:H/µc-Si:H tandem concept the manufactures have to increase the efficiencies or reduce the fabrication costs tremendously, or ideally both.

In recent years, promising progress has been made in both, reducing the production costs and increasing the efficiency. The latest developments include the implementation of intermediate reflectors between the top and bottom cell [57] and the use of an antireflection layer between the zinc oxide and silicon layer [58]. Record efficiencies up to 11.7% on lab scale have been achieved by Yamamoto et al. [59]. For 10 × 10 cm² solar modules deposited at a large area PECVD system at IEF5, a stabilized efficiency of 10.1% was found [60]. Very recently, Sunfilm reported a new world record of 9.6% total area efficiency for a module of 2.6 × 2.2 m² size [61]. For comparison, the efficiencies of mono- and multicrystalline silicon solar modules reach ~ 19% in mass production to date.

This chapter focuses on very thin tandem cells with the aim to reduce the production cost per Watt peak. The use of very thin absorber layers reduces the deposition time, material consumption, and reactor cleaning effort. Consequently, a higher throughput is achieved. These aspects are all closely related to a decrease in production costs.

Thin intrinsic layers lead to a reduced absorption of light resulting in a reduced short-circuit current densities. So far, no detailed study on the extent to which a deterioration of cell performance occurs, when the total thickness is significantly reduced, has been done. The reduced layer thicknesses result in a smaller recombination volume that should enhance the open-circuit voltage. Additionally, a stronger electrical field extends over the thin absorber layers and suppresses recombination processes therein. Consequently, higher fill factors are expected. Thin amorphous top cells (< 150 nm) show a lower degradation rate compared to standard thick top cells (~ 300 –

400 nm thick) [7] which, to a certain degree, should balance the lower initial efficiencies.

3.2 Thin-film a-Si:H/µc-Si:H tandem cells on different TCOs

Silicon based thin-film solar cells in the p-i-n configuration are usually deposited on TCO (Transparent Conductive Oxide)-covered glass substrates. After some general aspects about TCOs the morphology and optical properties of two distinct substrate types will be presented. Based on these properties the performance of thin tandem cells deposited on the substrates will be discussed.

3.2.1 TCO types and requirements

The requirements TCO layers have to fulfill are diverse. They have to provide a good contact to the silicon layer and support the growth of device-grade silicon. Furthermore, high conductivity, high transmittance, and good optical scatter properties are essential. The latter is necessary to trap light in the thin silicon layers and is achieved by a textured surface. The most common TCOs are tin-doped indium oxide (In_2O_3:Sn), fluorine-doped tin dioxide (SnO_2:F) and gallium- or aluminum-doped zinc oxide (ZnO:Ga/Al). Commercially available tin dioxide covered glass substrates are for example Asahi U, using 1.1 mm thick green glass, or NSG, applying 3 mm thick white glass.

3.2.2 Substrate morphology

For the presented studies Asahi U and ZnO:Al layers, deposited in-house at IEF5-Photovoltaik on 1.1 mm thick Corning Glass, were used as substrates [62]. Whereas the tin dioxide exhibits a naturally grown surface structure the sputtered ZnO:Al has to undergo a wet-etching procedure to roughen the surface. Figure 3.1 and Figure 3.2 show SEM images in which the morphologies of the two substrate types are visualized. Both surfaces are randomly structured. Pyramids are observed on the surface of the as-deposited SnO_2:F (Figure 3.1) while the texture-etched ZnO:Al on Corning Glass shows

a crater-like structure (Figure 3.2). The size and depth of the craters vary, but the feature sizes are generally much larger than for the Asahi U substrate. Whereas the craters include a flat angle with the surface (~ 20°) steeper angles of ~ 37° are found for the pyramids on Asahi U. Since these pyramids have a smaller feature height the rms (root mean square)-roughness amounts to only ~ 40 nm for Asahi U compared to ~ 120 nm for ZnO:Al.

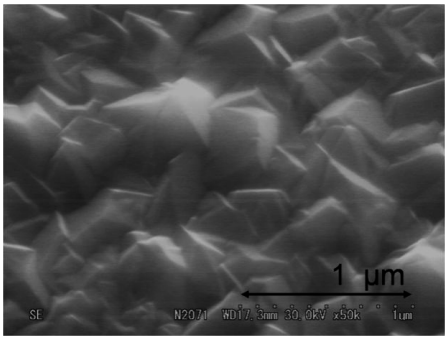

Figure 3.1 SEM image of naturally grown pyramidal structure of Asahi U substrates

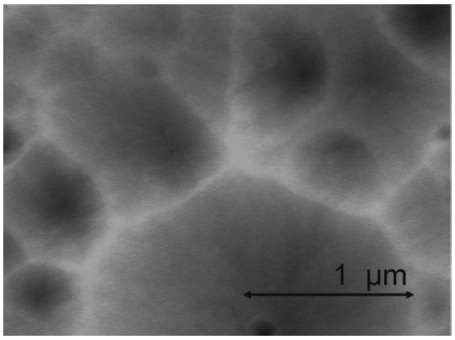

Figure 3.2 SEM image of the crater-like structure of ZnO:Al after etching

3.2.3 Optical properties

In order to evaluate the light scattering ability and transparency of Asahi U and texture-etched ZnO:Al in the wavelength region relevant for solar cells diffuse and total transmittance were measured by a Perkin Elmer Lambda 950 spectrometer. The data are discussed in relation to material properties and surface texture.

Influence of material The diffuse and total transmittance (T_{diff}, T_{total}) of the Asahi U and (texture-etched) ZnO:Al substrates were measured in the range from 300 nm < λ < 1200 nm which is the relevant spectrum for solar cell application. In Figure 3.3 T_{diff}, T_{total} and their quotient, the haze, is depicted. In the low λ region, the low transmittance of both substrate types stems from optical band-to-band transitions in the TCO layers. The different absorption edges of Asahi U and ZnO:Al are related to

the different band gap energies of SnO_2:F and ZnO:Al which amount to 3.4 eV and 3.2 eV, respectively. Part of the absorption in the red and infrared region is caused by the iron particles in the green glass of the Asahi U substrates [63]. For that reason glass with a low iron content such as Corning Glass is preferred for photovoltaic application based on µc-Si:H.

Influence of morphology The small structure size of the SnO_2:F surface leads to interferences in the transmittance curve and a low diffuse transmittance. This results in a low haze value. The lower transmittance of Asahi U in the short-wavelength region is attributed to internal light trapping. Due to the steep surface features and the low refractive index of the adjacent material air (n = 1) the light is reflected into the TCO layer itself [64]. This effect is visible since no index matching fluid was applied during the measurement. However, if silicon with a refractive index of 3.5 is deposited on top of the TCO this effect is not observed and the light is scattered into the Si layer.

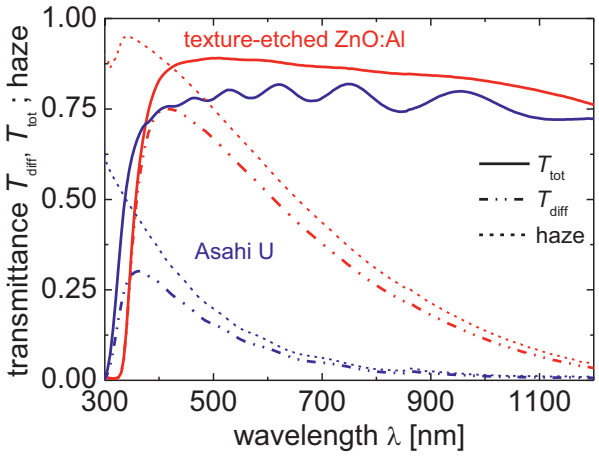

Figure 3.3 Diffuse and total transmittance of texture-etched ZnO:Al and Asahi U. The ratio (haze) is displayed additionally.

For both substrates, the haze, which is a measure of how much light is scattered at a rough surface [65], decreases for light with longer wavelengths. However, higher values

are observed for the ZnO:Al substrate. It shows that larger structures usually scatter light with longer wavelengths more efficiently.

The haze is often used to evaluate the light trapping properties of TCOs and the short-circuit current densities reached by solar cells deposited on the TCOs. Lechner et al. showed that a correlation between haze and J_{sc} exists when the same TCO type with similar properties is compared. No general correlation is found when considering different types of TCO [66]. Thus, comparison of the light trapping properties of Asahi U and ZnO:Al has to be treated carefully.

A lower performance on Asahi U substrates is expected according to the optical measurements. First, iron particles in the used glass absorb in the infrared region and, second, the small feature size scatters light of longer wavelength less efficiently.

Detailed studies on optical and electrical properties of ZnO:Al were done by Hüpkes et al. [67]. Recent developments in the field of TCO were published by Zhu [68; 69] and Berginski [62].

3.2.4 Tandem cells deposited on Asahi U and ZnO:Al substrates

To investigate how the morphology and optical properties of the two substrates affect the performance of tandem solar cells, two current matched tandem cells with a silicon thickness of about 960 nm, which is much thinner than typical cells, were deposited on each type of substrate.

Comparison of quantum efficiency In Figure 3.4, the quantum efficiencies of the two tandem cells are compared. The individual subcells are displayed as well as their summation. The top cell on Asahi U shows a spectral response already at a wavelength of ~ 320 nm whereas for the top cell on ZnO:Al no absorption occurs below a wavelength of ~ 360 nm. Due to the higher band gap energy of Sn_2O:F compared to ZnO:Al, Asahi U type substrates become transparent at lower wavelengths as ZnO:Al substrates. The energy of the light is not high enough to be absorbed in the TCO layer and reaches the silicon layer where it contributes to charge carrier creation. This is in accordance to the transmittance measurements shown and discussed in subsection 3.2.3.

Additionally, the parasitic absorption of the window-p-doped layer on ZnO:Al is stronger. Due to the n-type character of ZnO:Al it is necessary to use a thicker p-doped layer that consists of highly conductive microcrystalline and an amorphous p-doped layer. This design improves the contact between the TCO and the p-doped layer but leads to a stronger parasitic absorption and a further shift of the absorption edge to higher wavelengths.

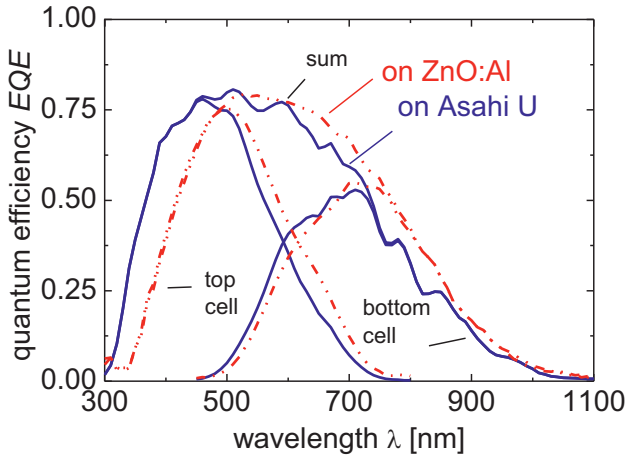

Figure 3.4 Quantum efficiency measurements of tandem cells on a Asahi U and a ZnO:Al substrate with a total thickness of 960 nm

For both top cells the maximum *EQE* value is similar, although it appears at higher wavelengths for the cell on the ZnO:Al substrate. The *EQE* characteristics of the bottom cell on ZnO:Al evidences a much better response in the infrared region with a higher maximum than on Asahi U. The lower response on Asahi U substrates stems partially from the used green glass, which absorbs parasitically in the infrared region. Therefore, it is derived that on Asahi U a thicker bottom cell is necessary to reach a similar high short-circuit current density than on ZnO:Al substrates.

Comparison of cell performance Table 3.1 summarizes the cell performances measured under AM1.5 and the short-circuit current densities of top and bottom cell

derived from the quantum efficiency measurements. A higher $J_{sc,bot}$ confirms the good response in the infrared wavelength region for the tandem cell on ZnO:Al. Additionally, an open-circuit voltage of 1429 mV and a high fill factor of 75% indicate a good quality of TCO/p-interface.

On Asahi U, a significantly lower open-circuit voltage and a lower fill factor are observed. This suggests a rather defect rich TCO/p-interface leading to high recombination and hence lower V_{oc} and *FF*.

Table 3.1 Photovoltaic parameters of thin tandem cells (d_{total} = 960 nm) deposited on Asahi U and texture-etched ZnO:Al

substrate	η [%]	*FF* [%]	V_{oc} [mV]	$J_{sc,top}$ [mA/cm²]	$J_{sc,bot}$ [mA/cm²]
ZnO:Al	10.28	75.0	1429	10.1	10.1
Asahi U	9.95	72.7	1372	9.8	9.7

3.2.5 Summary

The requirements on TCO, e.g., the ability to trap the incoming light, high transmittance and high conductivity, are fulfilled better by texture-etched ZnO:Al over a wide wavelength range. Quantum efficiency and photovoltaic parameters of tandem cells deposited on both substrate types are in correspondence with the optical and morphological properties of the substrates. The smaller structure size of the SnO_2:F surface leads to a lower scatter ability of light in the infrared wavelength region. Additionally, the use of absorbing green glass makes it necessary to use thicker microcrystalline bottom cells to gain the same current density as on ZnO:Al.

It was shown that the performance of the tandem cell on ZnO:Al is better as for the tandem cell on Asahi U. However, the aim of the further studies is to investigate how a reduction of top and bottom cell thickness, simultaneously and individually, influences the device performance. To separate thickness related effects from TCO related effects,

and to ensure the reproducibility of the experiments, Asahi U as a substrate with constant quality was chosen. The properties of the in-house sputtered ZnO:Al is influenced by fluctuations mainly due to the target quality. After investigating the effects occurring in thin tandem cells on Asahi U in detail a transfer to ZnO:Al substrates is not critical.

3.3 Performance of a-Si:H/µc-Si:H tandem cells depending on total thickness

This section presents amorphous and microcrystalline silicon tandem solar cells with different thicknesses in order to investigate the influence of the total i-layer thickness on the cell performance. The resulting photovoltaic parameters are given and discussed with a special focus on the fill factor. Four quantum efficiency characteristics of tandem cells are exemplarily shown. From *EQE* and cell reflectivity measurements the parasitic absorption is calculated. The main results presented in section 3.3 and section 3.4 are published by Schicho et al. [70].

3.3.1 Sample description

A systematic series of a-Si:H/µc-Si:H tandem cells of different thicknesses were deposited on Asahi U substrates. The deposition conditions (pressure, silane concentration, power) were kept constant to ensure equal material quality and growth rates. Only the deposition times of the absorber layers were changed to achieve varying thicknesses. Top and bottom i-layer thicknesses were reduced pairwise. The thickness combinations were chosen according to previous experiments and fine-tuned to approach current matching.

The standard tandem cell on Asahi U substrates is approximately 2300 nm thick with about 390 nm and 1850 nm top- and bottom i-layer, respectively. The thicknesses of the amorphous and microcrystalline absorber layers were gradually reduced. The thinnest tandem cell had a top i-layer of only 110 nm and was combined with a 340 nm

bottom i-layer. Hence, the total thicknesses covered a range from ~ 2300 nm to ~ 520 nm.

3.3.2 Photovoltaic parameters

The deposited tandem cells were measured with a solar simulator under standard condition (AM1.5 illumination at 100 mW/cm², 25°C) to evaluate the photovoltaic parameters, namely efficiency, fill factor, open-circuit voltage and short-circuit current density. The thickness dependence of the values is shown in Figure 3.5 a) – d) and is individually discussed.

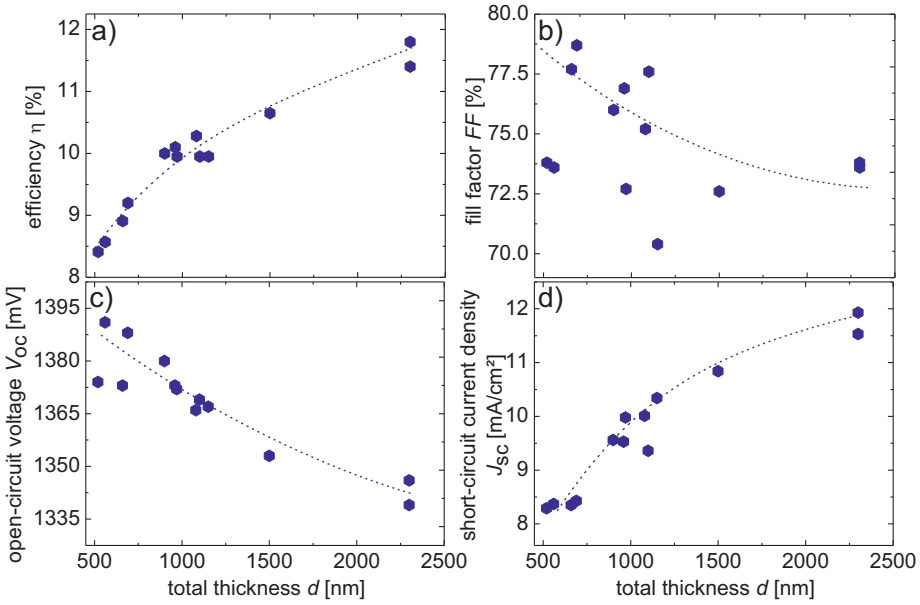

Figure 3.5 Photovoltaic parameters of nearly current matched tandem cells with different total thicknesses. Top and bottom cell thicknesses were varied at the same time. The dashed lines are guides to the eye.

Efficiency η Figure 3.5 a) illustrates the initial efficiency as function of the total thickness. Tandem cells with thicknesses in the range of 2300 – 520 nm achieve efficiencies between 11.4% and 8.4%. Down to a thickness of ~ 1000 nm η decreases

with a rather small slope to a value of ~ 10.1%. That means that with less than 50% of the standard thickness 88.6% of the related efficiency can be accomplished. By further reducing the total thickness, the efficiency drops more rapidly.

Fill factor *FF* The fill factor shows an increasing trend with decreasing thickness (Figure 3.5 b)). This is attributed to improved charge carrier collection due to, first, the smaller distance the charge carriers have to travel before reaching the contacts and, second, the higher average electrical field $\overline{E}$ over both i-layers. The latter is derived from equation 2.2: Since the built-in potential remains unchanged and d decreases, $\overline{E}$ consequently increases.

Open-circuit voltage V_{oc} The open-circuit voltage increases consistently with decreasing layer thickness as shown in Figure 3.5 c). Generally, V_{oc} is influenced by surface and bulk recombination. The latter one is the dominant process in the µc-Si:H bottom cell [71; 72] whereas the recombination in the amorphous top cell is mainly influenced by the recombination at the p/i-interface [73; 74]. By reducing the thickness of the tandem cell, the bulk recombination decreases due to the reduced volume and V_{oc} increases.

Short-circuit current density J_{sc} Figure 3.5 d) displays the dependency of J_{sc} on the total thickness. Due to the decreasing path length of the light in the absorber layer J_{sc} drops with decreasing thickness. The thickness reduction from 2300 nm to 520 nm leads to a severe loss in short-circuit current density of 30.5%. The decrease in short-circuit current density is also responsible for the loss in efficiency, and is only partially compensated by the increase in fill factor and open-circuit voltage.

3.3.3 Influence of matching on fill factor

Besides the thicknesses of the device, the individual *JV*-characteristics of the subcells influence the fill factor. In the following, the origin of the fill factor dependence on subcell limitation and current matching is explained.

Graphical derivation of *FF* in tandem cells The fill factor in Figure 3.5 shows some scattering that is attributed to variations in matching of the tandems cells. The fill factor of a tandem cell is expected to have a minimum in the matched case where $J_{sc,top}=J_{sc,bot}$ and increases for a ratio $J_{sc,top}/J_{sc,bot} \neq 1$. The scheme in Figure 3.6 visualizes the *FF* of the subcells implemented in a tandem cell. The fill factor is mathematically defined by the ratio of the power at the maximum power point P_{MPP}

$$P_{MPP} = V_{MPP}J_{MPP} \tag{3.1}$$

to the virtual power P_V

$$P_V = V_{oc}J_{sc} \tag{3.2}$$

that leads to

$$FF = \frac{V_{MPP}}{V_{oc}}\frac{J_{MPP}}{J_{sc}}. \tag{3.3}$$

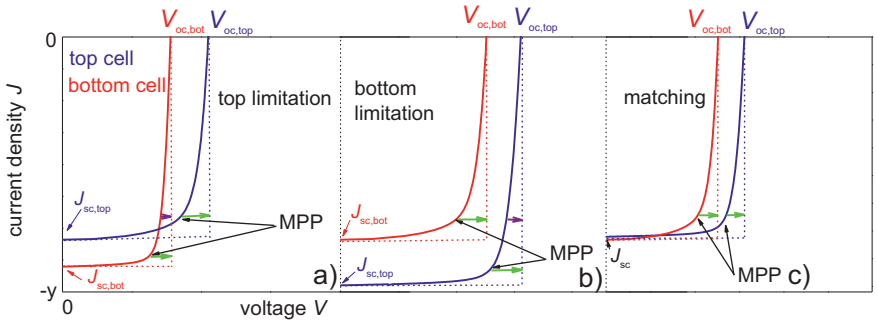

Figure 3.6 Individual subcell fill factors for a) top limited, b) bottom limited and c) matched tandem cells (c))

As shown in Figure 3.6 the ratio V_{MPP}/V_{oc} is larger than J_{MPP}/J_{sc}, given by the distances between the JV – characteristics and the rectangle. Hence, the difference between the voltage at the maximum power point and the open-circuit voltage determines the fill factor loss when the cell is operated at the MPP. The voltage loss is defined as:

$$\Delta V(J) = V_{oc} - V(J) \tag{3.4}$$

whereas $\Delta V(J)$ decreases for lower current densities. In a tandem cell the voltages, and so the ΔV, at a given current of the subcells sum to a total voltage at this current:

$$\Delta V(J)_{tandem} = \Delta V(J)_{top} + \Delta V(J)_{bot}. \tag{3.5}$$

In a top or bottom limited tandem cell one subcell always works at a current below the one at MPP, which means that also $\Delta V(J)$ is lower than at the MPP, indicated by the violet arrow in Figure 3.6 a) and b). Therefore, the sum of $\Delta V(J)$ in a top or bottom limited tandem cell is lower than the $\Delta V(J)$ in the matched case, where both subcells work at the MPP with the maximum in $\Delta V(J)$, indicated by green arrows in Figure 3.6 c). This high $\Delta V(J)$ influences the fill factor directly, leading to low values in the current matched case and increasing fill factors with stronger limitation.

3.3.4 Influence of total thickness on quantum efficiency

Four tandem cells with total thicknesses between 2300 nm and 560 nm were used to study the dependency of top and bottom cell short-circuit current density on the thickness of the subcells. Both, top and bottom i-layer thicknesses, were reduced simultaneously.

Table 3.2 Efficiency and top and bottom short-circuit current densities of the tandem cells displayed in Figure 3.7

	d [nm]	η [%]	$J_{sc,top}$ [mA/cm²]	$J_{sc,bot}$ [mA/cm²]
1	2300	11.8	12.1	11.5
2	1500	10.7	10.6	10.5
3	1050	10.0	10.5	9.7
4	560	8.6	8.8	8.1

In Figure 3.7, the quantum efficiency characteristics of the individual subcells as well as their summation are presented for the four selected tandem cells. The deduced $J_{sc,top}$ and $J_{sc,bot}$ as well as the efficiency, determined by solar simulator measurements are given in Table 3.2.

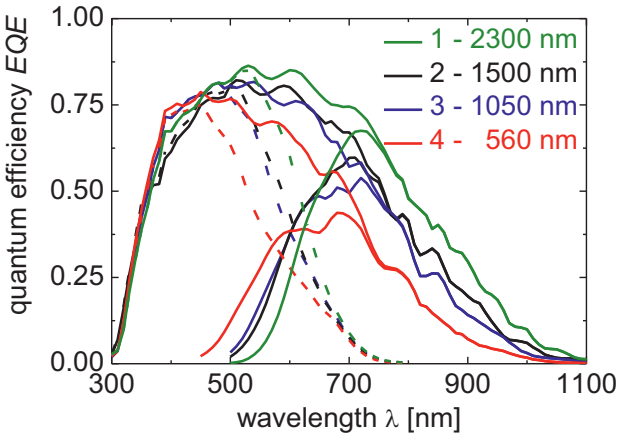

Figure 3.7 EQE curves of tandem cells of varying total thickness given in the right corner

All cells were slightly bottom cell limited. The best matching was realized for Sample 2. The top and bottom cell short-circuit current densities decrease with decreasing thickness in accordance to the *JV*-measurements. The crossing point of the top and bottom *EQE* curves shifts to lower wavelengths with decreasing cell thickness. That means that the light for which the thin top cell is transparent is absorbed in the bottom cell. In addition, one can see that with decreasing top cell thickness the blue response in a wavelength region between 350 nm and 400 nm increases. In this region, the absorption in the p-doped layer plays a major role [75]. The internal electric field extends solely over the thick i-layer and, thus, carriers created in the doped layers are not separated. From the data and the fact, that the p-doped layer is the same for all cells within this thickness series, there must be an additional effect. In general, the electric field is not abruptly created by a sharp transition between doped and intrinsic silicon, so

charge carriers created close to the i-layer might be separated as well. In thin cells the much stronger field in the i-layer might extend much further into the doped layers and this effect is more pronounced.

3.3.5 Parasitic absorption dependent on total thickness of tandem cells

In Figure 3.8, the parasitic absorption for the four tandem cells is depicted. The parasitic absorption A_p is given by

$$A_p = 1 - R_{cell} - EQE \tag{3.6}$$

with R_{cell} as the reflectivity of the cell. In general, the parasitic absorption increases significantly with decreasing i-layer thickness in the spectral range of 450 – 1000 nm. The absorption in the silicon i-layers, which contributes to effective charge carrier generation, decreases due to less absorbing volume. All other (parasitically) absorbing parts of the cell, namely the doped layers, front TCO, ZnO:Al back reflector and glass substrate, remain unchanged. Therefore, the share of parasitically absorbed light compared to the overall absorbed light increases for thinner i-layers.

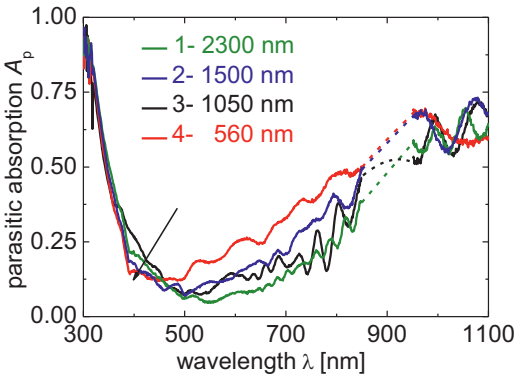

Figure 3.8 The parasitic absorption A_p of the four investigated tandem cell. For the region of the detector change no values are shown, the interpolated region is given by the dashed lines.

The arrow emphasizes the decrease of parasitic absorption for thinner tandem cells in the wavelength region between 350 nm and 400 nm. In this wavelength region,

absorption mainly occurs in the window-p-doped layer. It is assumed that the lower A_p for the thinner tandem cells is caused by charge carriers extracted from the p-type doped layer that contribute to the cell current.

3.3.6 Summary

Tandem cells with thicknesses in the range of 2300 nm to 520 nm were deposited on Asahi U substrates by varying the deposition time of top and bottom i-layer simultaneously to keep the matching condition. A drop in short-circuit current density due to less absorbing material was noticed whereas open-circuit voltage and fill factor increased with decreasing total thickness. The electric field, which increases with decreasing layer thickness, leads to lower bulk recombination and, hence, higher *FF*. Additionally, it enhances the charge carrier extraction out of the p-type doped layer which reduces the parasitic absorption. Due to the lower short-circuit current density the efficiency decreased. However, a tandem cell with less than 50% of the standard thickness achieved 88.6% of the original efficiency.

3.4 Individual influence of top and bottom cell thickness

To investigate the effect of the reduced layer thicknesses in more detail two series were prepared: In Series A, the top cell thickness was kept constant while the bottom cell thickness was varied. In Series B it was preceded vice versa. The quantum efficiencies and derived short-circuit current densities are discussed.

3.4.1 Variation of bottom i-layer thickness

Influence of bottom i-layer thickness on *EQE* Series A consists of three tandem cells with a 250 nm thick top i-layer, which was combined with a 1500 nm (Sample 1), a 900 nm (Sample 2), and a 450 nm (Sample 3) thick bottom i-layer. The individual layer thicknesses were estimated by deposition time and rate, and the total thicknesses were measured by a profilometer.

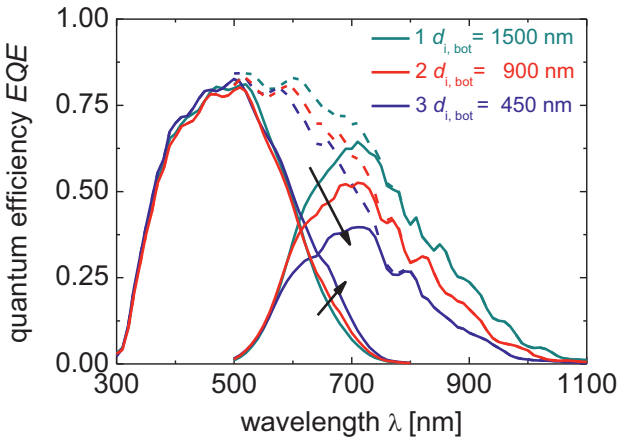

Figure 3.9 Quantum efficiency measurements for Series A for which the bottom i-layer thickness was varied. The top i-layer thickness was kept at 250 nm. The dashed lines represent the summation of top and bottom EQE curves.

In Figure 3.9, the quantum efficiencies of the three devices are compared. The wavelength region in which the bottom cells absorb and the position of the maximum *EQE* in the bottom cell curves are at identical wavelength positions for Samples 1 – 3. According to the reduced thickness, the quantum efficiency decreases indicated by the upper arrow. The number of visible interference fringes decreases also with layer thickness and is roughly proportional the bottom i-layer thickness.

Although the three top cells have the same thickness, the *EQE* curves differ, especially in the wavelength region 600 nm < λ < 750 nm. The effect of the thinner bottom cell on quantum efficiency of the top cell of Sample 1 and 2 is small but a significant higher *EQE* is measured for Sample 3 indicated by the lower arrow. The integrated top cell short-circuit current density amounts to 11.6 mA/cm^2 compared to 11.0 mA/cm² and 10.9 mA/cm² for Sample 1 and 2, respectively. The increase in top cell short-circuit current density is attributed to back reflected photons: Part of the light that is not absorbed during the first way through the cell is reflected by the ZnO:Al/Ag layer at the back of the cell. Because of the reduced bottom i-layer thickness, it transmits these photons so that they can reach the top cell again.

Top and bottom short-circuit current densities $J_{sc,top}$ and $J_{sc,bot}$ Figure 3.10 depicts the top and bottom cell short-circuit current densities for different bottom i-layer thicknesses. The values for $J_{sc,bot}$ increase with increasing layer thickness. The trend is in accordance to the Lambert-Beer law. The intensity of light decreases exponentially with absorber layer thickness and leads to an attenuation of the linear short-circuit current density increase with layer thickness. The top cell short-circuit current density decreases slightly when the bottom cell thickness increases. This effect is attributed to a lower back reflection through the bottom cell.

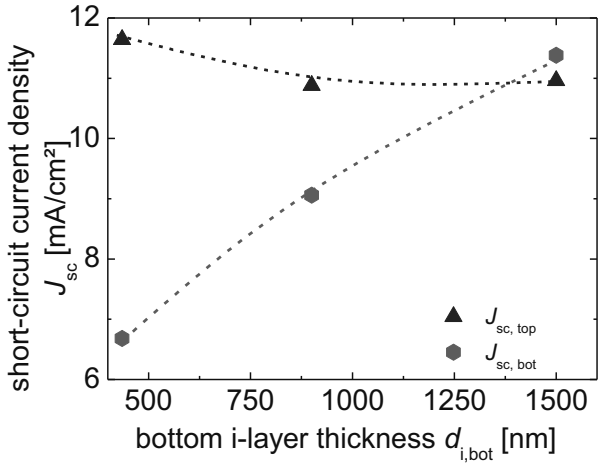

Figure 3.10 Short-circuit current densities determined from the EQE measurements of the subcells of Series A. The dashed lines are guides to the eye.

3.4.2 Variation of top i-layer thickness

Influence of bottom i-layer thickness on *EQE* For Series B, the top i-layer thickness was varied and combined with a bottom cell of 900 nm i-layer thickness. Additionally to Sample 2 (250 nm top i-layer) two cells with a 140 nm (Sample 4) and a 350 nm (Sample 5) thick top i-layer were deposited.

Figure 3.11 depicts the quantum efficiency of the three tandem cells. The subcells are given by the straight lines; the dashed lines refer to the sum of the according

subcells. The top cell short-circuit current density rises from 9.1 mA/cm² for the thinnest device (Sample 4) up to 11.6 mA/cm² for Sample 5 with the thickest top i-layer. This is attributed to an increased optical path length leading to a higher absorption. At the same, time $J_{sc,bot}$ decreases because the thicker top i-layer is less transparent and, consequently, less light reaches the bottom cell. The intersection of the top and bottom curve is in all cases at an *EQE* value of 0.37, and shifts from a wavelength of approximately 570 nm to 640 nm with increasing top cell thickness.

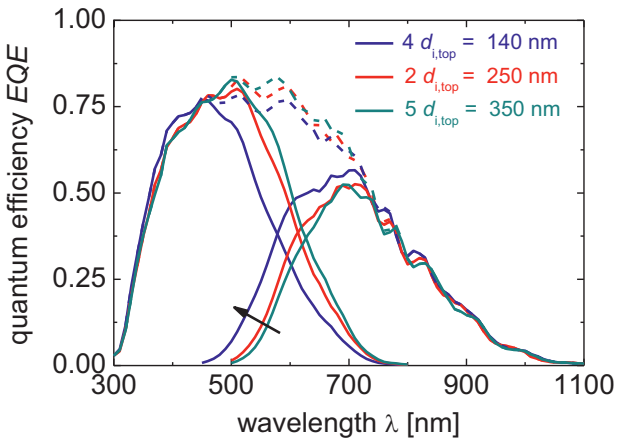

Figure 3.11 Quantum efficiency measurements for Series B for which the top i-layer thickness was varied at constant bottom i-layer thickness of 900 nm. The dashed lines represent the summation of top and bottom EQE curve. The arrow indicates the higher absorption in the bottom cell with decreasing top i-layer thickness.

In the region between 390 nm < λ < 450 nm, the quantum efficiency of the thinnest tandem cell is higher compared to the other two samples. As discussed before, this is attributed to charge carrier extraction out of the window-p-doped layer due to a higher electrical field.

Top and bottom short-current current densities $J_{sc,top}$ and $J_{sc,bot}$ The current densities of top and bottom cell derived from *EQE* measurements on the Series B cells

are shown in Figure 3.12 as a function of the top i-layer thickness. The top cell short-circuit current density increases for thicker amorphous i-layers due to a higher absorption volume, and seems to saturate following the Lambert-Beer law. As the top cell short-circuit current density increases, the bottom cell short-circuit current density decreases because less light reaches the bottom cell.

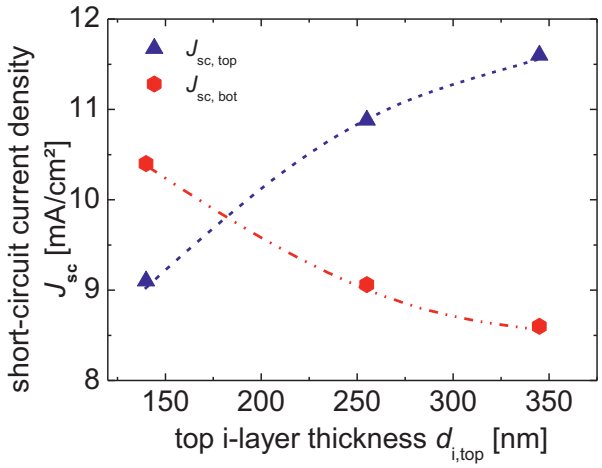

Figure 3.12 Short-circuit current densities determined from the quantum efficiency measurements of the subcells of Series B. The dashed lines are guides to the eye.

3.4.3 Summary

By reducing the bottom i-layer thickness at a constant top cell thickness, on the one hand, the bottom cell short-circuit current density decreases due to less absorbing material. On the other hand, the top cell short-circuit current density increases due to back reflected photons, which are transmitted into the top cell by the thin bottom cell.

The reduction of the top i-layer thickness leads to a reduction in top cell short-circuit current density accompanied with an increase in bottom cell short-circuit current density caused by a higher transparency of the thin top cell. Due to an increased electric field over thinner top cells charge carrier extraction from the window-p-doped layer occurs.

3.5 Thickness dependence of light-induced degradation

Amorphous silicon single junction solar cells are known to degrade under light exposure due to the Staebler-Wronski-effect [7]. Accordingly, also stacked cells with an a-Si:H subcell are affected by degradation. Optimized µc-Si:H bottom cells show a higher stability against light-induced degradation [76]. In a-Si:H single junction solar cells the relative degradation decreases with decreasing layer thickness [77]. Therefore, thin tandem cells having significantly thinner a-Si:H top cells are expected to degrade less than standard tandem devices. To investigate the degradation behaviour five slightly bottom cell limited tandem cells covering a thickness range from 560 nm to 2300 nm underwent the light soaking procedure.

3.5.1 Light-induced degradation of tandem solar cells

Stabilized performances of the tandem cells are evaluated in dependency of the total thickness. The results are discussed in regards to previously achieved module results.

Initial and stabilized photovoltaic parameters Figure 3.13 a) – d) displays the initial and stabilized values of efficiency, fill factor, open-circuit voltage and short-circuit current density, respectively. It can be seen that the standard cell with a total thickness of 2300 nm shows the largest difference between initial and stabilized efficiency. With decreasing thickness the degradation decreases continuously. For the thick standard tandem cell with 2300 nm total thickness the degradation amounts to 16.5%. In contrast, only 7.0% degradation is observed for the 660 nm thick cell leading to a stabilized efficiency of 8.4%.

A similar decrease in degradation with decreasing total cell thickness was previously found by Repmann et al. [78]. A loss in stabilized efficiency of only 21% for a total absorber layer thickness reduction of 75% from 2300 nm to 560 nm is found. The lower degradation rate for thin tandem cells mainly results from the lower degradation in fill factor as shown in Figure 3.13 b). For the 2300 nm thick cell it degraded about 15.3%, whereas the loss in *FF* for the thin 560 nm-cell was only 4.3%. The degradation

of V_{oc} and J_{sc} (Figure 3.13 c) und d)) is small, and virtually independent of the thickness.

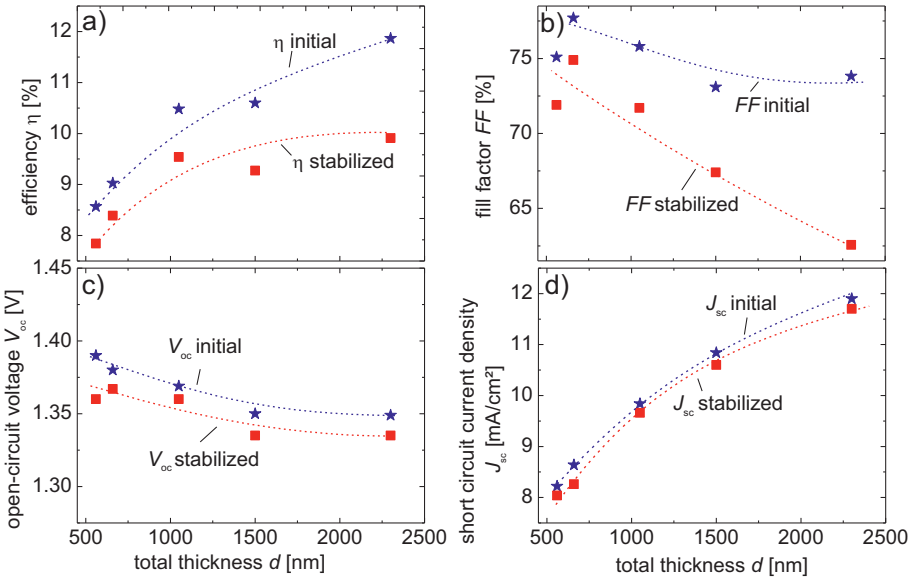

Figure 3.13 Photovoltaic parameters before and after 1000 h of light soaking for tandem cells with different thicknesses. The lines are guides to the eye.

3.5.2 Thin mini-modules on ZnO:Al substrates

Using the deposition conditions with which the cells were deposited 10×10 cm² mini-modules have been produced and investigated analogously to the cells. Their degradation behaviour is similar to that of the cells: A 960 nm thin mini-module on a texture-etched ZnO:Al-coated glass substrate achieved a current density of 9.2 mA/cm² cell area and an open-circuit voltage of 1390 mV per cell. After 1000 h of light soaking, the module efficiency dropped from 9.8% to 9.0%, which equals a degradation of only 8.1%.

3.5.3 Summary

It was shown that the very thin amorphous top i-layers of the thin tandem cells led to a significant reduced degradation compared to a standard thick tandem cell. With a reduced device thickness of 560 nm, which is 75% thinner than the standard thick cell, the stabilized efficiency decreased by only 21% compared to the standard cell.

3.6 Conclusion

Tandem solar cells, consisting of an a-Si:H top and µc-Si:H bottom cell, with considerable thinner i-layers deliver reasonable efficiencies. For example, a thickness reduction of 77% leads to an efficiency loss of only 29%. Due to the smaller bulk recombination, the open-circuit voltage and fill factors increase, and hence, balance the loss in short-circuit current density partially.

A systematical thickness reduction of the bottom i-layer (Series A) reveal a gain in top cell short-circuit current density due to back reflected photons. By reducing the top i-layer thickness (Series B) charge carriers are extracted out of the window-p-doped layer that contribute to the short-circuit current density.

Light soaking experiments evidenced a lower degradation rate due to the use of thinner top cells. Therefore, the loss in stabilized efficiency amounts to only 21% for a thickness reduction of 75%. Especially from the industrial point of view this result is very interesting. Thinner layers are related to, e.g., shorter deposition times and less material consumption that are directly related to less costs.

Chapter 4

Optimization of very thin tandem cells

The following chapter presents different approaches to increase the performance of very thin tandem cells such as the use of high band gap amorphous material, aiming at an increase of open-circuit voltage. The influence of silane concentration and deposition temperature on the band gap of a-Si:H i-layers is investigated, and their ability to improve the open-circuit voltage was tested in a-Si:H single junction solar cells. Initial and stabilized photovoltaic parameters are discussed. For further performance improvement, the window-p-doped layer is adjusted for two different high band gap i-layers. Additionally, the use of thinner doped layers is evaluated for thick and thin tandem cells with standard a-Si:H material and high band gap a-Si:H material in the top cells. These approaches are combined with high deposition rate processes for μc-Si:H and front-ZnO:Al, and the deposition time reduction is evaluated regarding stabilized efficiencies.

4.1 Introduction

The reduced i-layer thicknesses of the previously introduced thin tandem solar cells bear some possibilities for improvement that are not applicable for thick tandem cells. Standard thick tandem cells aim at high short-circuit current densities for which a low band gap and high absorption in the amorphous top cell is necessary. However, the attractiveness of very thin tandem cells is the possibility to achieve high open-circuit voltages that can be further increased by implementing high band gap a-Si:H in the top cell. Such high band gap materials are, e.g., a-SiC:H [79; 80] or a-SiO:H [81] that are achieved by adding carbon or oxygen during the deposition of amorphous silicon. These materials are often defect-rich and lead to a high degradation. By depositing at lower temperatures or silane concentrations, high hydrogen contents in amorphous silicon layers and increased band gaps are accomplished.

When implementing i-layers with higher band gaps into solar cells, it is likely that the band gap of the window-p-doped layer needs to be adjusted, too. A certain band gap difference between p- and i-layer is necessary to separate the created charge carriers sufficiently. In addition, a higher band gap in the window-p-doped layer reduces the parasitic absorption at low wavelengths and is therefore preferable.

The electric potential in tandem cells is built up by the p-type and n-type doped layers at the front and the back contact, respectively, and at the tunnel recombination junction that connects the two subcells. The doping content and the thickness of the doped layers influence the built-in potential and, hence, the electrical field over a given thickness. The use of thinner absorber layers in very thin tandem cells enhances the electric field compared to standard thick devices and may allow reducing the thickness of the doped layers without a deterioration of the fill factor. Consequently, less light is parasitically absorbed in the doped layers and the short-circuit current density increases.

Generally, depositing µc-Si:H at higher deposition rates leads to decreasing cell performance [82; 83; 84]. In very thin tandem cells applying bottom cell i-layer thicknesses of ~ 300 – 500 nm, which is about ¼ of the standard thickness, the impact of the lower material quality on cell performance is supposed to be negligible.

Deposition at high rate can be used to further reduce the deposition time and costs without deteriorating effects. Finally, stabilized efficiencies of different silicon based thin-film devices are evaluated regarding the deposition time.

4.2 Amorphous silicon with high band gap

4.2.1 General aspects

Effect of low deposition temperature Amorphous silicon deposited below 200°C often shows high defect densities and void fractions [85]. Due to a higher sticking coefficient, the surface diffusivity is reduced and the formation of voids and defects becomes likely [27]. Therefore, p-i-n single cells with such a-Si:H i-layers degrade much more than with standard device grade material.

Yang et al. found a Tauc band gap increase of 50 meV when the deposition temperature was reduced from 300°C to 175°C. The open-circuit voltage increased by 20 mV and the light-induced degradation of efficiency rose from 5.7% to 16.7% [86]. Saha et al. observed a similar increase of the Tauc band gap from 1.70 eV to 1.79 eV after reducing the substrate temperature from 200°C to 80°C [87].

Effect of silane concentration Another approach to increase the hydrogen content in amorphous material is to reduce the silane concentration by increasing the hydrogen flow [27]. Depositing with a lower silane concentration (*SC*) leads to denser material since the hydrogen plasma etches weak bonds in an amorphous network. Additionally, incorporated hydrogen passivates dangling bonds that otherwise act as defects and, thus, recombination sites. However, this also results in low deposition rates.

Yang et al. showed that a decrease of silane concentration together with a reduction of the substrate temperature during the deposition leads to a significant decrease in degradation, and a high stabilized open-circuit voltage [86]. This was also reported by Deng et al. and Saha et al. [85; 87].

Transition material High open-circuit voltages accompanied with sufficiently high J_{sc}-values were reported by Muthmann et al. [88] when so-called transition material

with medium-range order is implemented in a-Si:H single cells. Such material is deposited with a very low silane concentration at the beginning of the deposition that increases stepwise throughout the process. This kind of grading or profiling of silane concentration leads to amorphous silicon close to the phase transition to μc-Si:H for which a higher stability against light-induced degradation was found [89; 90].

The higher band gap of the material goes along with a lower absorption. Hence, thicker layers are required compared to standard material for reaching the same short-circuit current density. A critical point is the lower deposition rate due to the high hydrogen dilution, which can be overcome by increasing the power.

4.2.2 Material studies on high band gap amorphous silicon

Based on the summarized studies amorphous materials were deposited at reduced substrate temperatures and silane concentrations with the aim to increase the optical band gap. Electrical and optical properties were measured to evaluate the material quality and optical band gap, respectively.

Deposition details The Corning Glass substrates underwent an argon plasma treatment to roughen the surface and enhance the attachment of the silicon layers on glass. For the studies on high band gap material the temperature was set to 140°C and 110°C, which is 60 K and 90 K below the standard deposition temperature. For these two temperatures silane concentrations (*SC*) in the range of 4.9% to 1.0% were applied which are significantly lower than the standard value of 10.7%. The silane concentration was varied by increasing the hydrogen flow. Therefore, the total gas flow changed from 736 sccm to 2386 sccm whereas 336 sccm are used in the standard regime.

The “grading”-layers were deposited in a regime that was adapted from the work of Muthmann et al. [90]. The silane concentration starts at a low value and increases stepwise by increasing the silane flow every 240 s. The average *SC* amounts to approximately 3%.

To keep the deposition rate similar the power was adjusted. The layer thicknesses of the different samples varied between 280 – 400 nm.

Electrical properties Dark conductivity (σ_{dark}) and photoconductivity (σ_{ph}) of the prepared layers were investigated. Figure 4.1 a) displays the dark conductivity for the silane concentration series at 110°C and 140°C. At 110°C the dark conductivity increases with decreasing *SC*. At $SC = 1\%$ it reaches a very high value of 2.7×10^{-7} S/cm, which indicates a poor material quality and high defect density. No trend is found for the series at 140°C but the values are comparable to standard material for which σ_{dark} amounts to 2.5×10^{-11} S/cm. A low σ_{dark} pointed out by the green arrow in Figure 4.1 confirms good material quality when applying a silane grading.

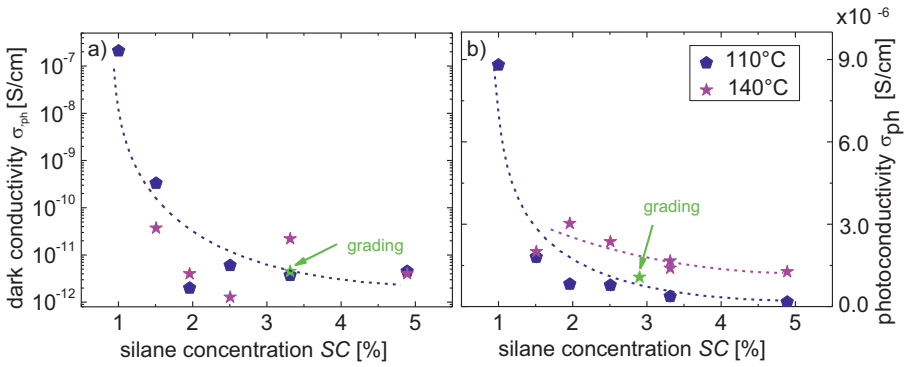

Figure 4.1 Dark (a)) and photoconductivity (b)) as function of the silane concentration for a-Si:H layers deposited at 110°C and 140°C. The lines are guides to the eye.

The photoconductivity σ_{ph} increases for both temperatures with similar trends with decreasing silane concentration. The values of the series at 140°C are higher compared to the values of samples deposited at 110°C. For the standard amorphous material a photoconductivity as high as 1.5×10^{-5} S/cm is found.

For application in solar cells high photoconductivities accompanied with low dark conductivities, which refers to high photosensitivities, are favoured. This was obtained for most of the materials in the *SC* range from 4.9 – 2%. A strong increase in dark conductivity was observed for *SC* below 2% indicating a deterioration of the material quality.

Optical properties Different definitions are used to describe the band gap of amorphous silicon based materials. The Tauc band gap E_T, which can be derived from equation 2.1, is often used to compare different materials. In this study, the "E_{04} band gap" was used as introduced in subsection 2.1.1 to evaluate the band gap of the previously described amorphous layers and standard material [27].

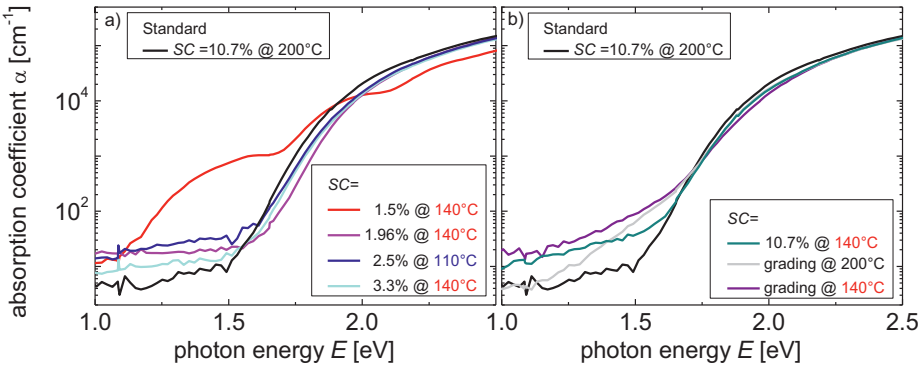

Figure 4.2 Spectra of PDS measurements on different high band gap and standard a-Si:H layers, deposited at different temperatures

The PDS spectra that were used to derive the E_{04} band gaps are plotted in Figure 4.2. The absorption curve shifts to higher energies for samples prepared at lower silane concentrations and lower deposition temperature. The latter can be seen by comparing the grading samples and the samples deposited at standard concentration at 200°C and 140°C (Figure 4.2 b)). In the region below 1.2 eV the absorption is in general attributed to defects. An increase in absorption in this region is observed with decreasing silane concentration, which suggests an increase in defect density. A noticeable crystalline contribution is found when a silane concentration of 1.5% is used indicating that the transition to microcrystalline material has already taken place.

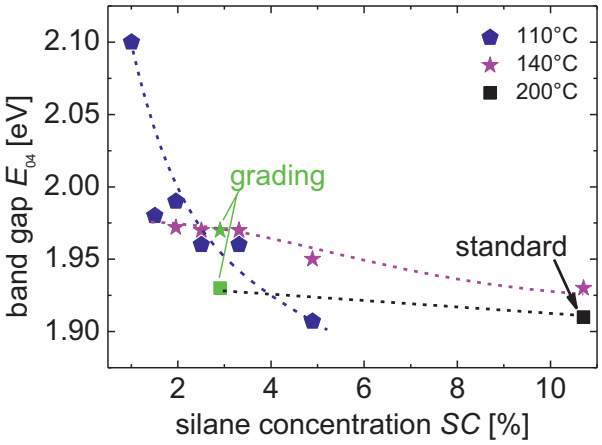

Figure 4.3 Optical band gap E_{04} plotted against silane concentration for different temperatures. The dashed lines are guides to the eye.

For a better comparison, the actual E_{04}-values derived from the curves in Figure 4.2 are plotted as a function of silane concentration in Figure 4.3. The standard material deposited with SC = 10.7% at 200°C has a band gap of 1.91 eV. It increases to 1.93 eV when a lower deposition temperature of 140°C is used. A similar effect is observed for the grading samples (green symbols): the band gap rises from 1.93 eV at 200°C up to 1.97 eV at 140°C.

For both silane concentration series, at 110°C and 140°C, an increase of E_{04} with decreasing silane concentration is observed. In the region of moderate SC (2.5 – 4.9%) samples prepared at the higher temperature show a higher band gap value, which is not expected from the studies presented in subsection 4.2.1. Below a silane concentration of 2.5% the E_{04} values of the samples deposited at 110°C exceed the E_{04} values of those deposited at 140°C and reach a maximum value of 2.1 eV at SC = 1.0%.

All a-Si:H-layers deposited with lower SC have higher E_{04} compared to the standard layer. Therefore, it is derived that not only lower temperatures lead to higher hydrogen contents in the layer. Also a higher hydrogen dilution (or lower silane concentration) of the deposition gas mixture facilitates the incorporation of hydrogen. The combination of

both, lower T_{depo} and *SC*, leads to an E_{04} band gap as high as 2.1 eV, which is 190 meV higher than E_{04} band gap of the standard material.

4.2.3 Summary

With decreasing deposition temperature and increasing applied silane concentration a decrease in photoconductivity is observed for a-Si:H material. An increase in dark conductivity for samples deposited with $SC < 1.5\%$ is noticed indicating a transition to microcrystalline silicon.

According to the PDS spectra the defect density increases for reduced deposition temperatures. A lower silane concentration was not able to balance this effect, which is contrary to Yang et al. [86] and Saha et al. [87].

Significantly higher E_{04} band gaps up to 2.1 eV are reached by decreasing the silane concentration due to the incorporation of hydrogen into the amorphous network. Over a wide range of *SC* the layers deposited at 140°C show higher band gaps compared to the layers deposited at 110°C with the same *SC,* which is not in agreement to the previously mentioned consideration.

4.3 Single cells with high band gap a-Si:H

To evaluate the applicability of the previously described high band gap materials in top cells of thin tandem cells, first, they were tested as amorphous single junction cells. Increased open-circuit voltages were observed accompanied with reduced short-circuit current densities. This made an adjustment of the layer thicknesses necessary in order to compare the different materials at equal J_{sc}. The photovoltaic parameters of the a-Si:H single junction cells are presented with special focus on the stabilized values after light-induced degradation. The results are discussed in dependence of the used silane concentration and the E_{04} band gap.

4.3.1 Fabrication of high band gap solar cells

Apriori consideration The high band gap amorphous silicon was investigated to substitute the standard i-layer in the top cell of very thin tandem cells. Therefore, the high band gap top cell has to deliver the same J_{sc} as the standard top cell to fulfill the matching condition. A standard single a-Si:H cell with an i-layer thickness of approximately 150 nm as in the thin tandem cell was deposited. With Ag as back reflector/contact this reference cell had a short-circuit current density of 10.1 mA/cm². It was aimed to reach this value with high band gap material by adjusting the deposition time and, consequently, the layer thickness.

After finding suitable layer thicknesses for each of the considered deposition regimes, single cells with a ZnO:Al/Ag stack as back reflector/contact were deposited. The additional ZnO:Al layer is supposed to increase the stability of the electrical contacts during the light soaking experiments without affecting the open-circuit voltage on which the focus lay.

Deposition details The amorphous single junction solar cells were deposited on Asahi U substrates. The p-and n-type doped layers were not changed compared to the standard cell. Only for the samples that were deposited with silane grading a 25% higher deposition time was used for p-doped layer. Since the deposition starts with a very low silane concentration, the hydrogen plasma etches already deposited silicon. From previous experience, an initially thicker p-doped layer had proven of value.

After adjusting the thickness of the different solar cells to roughly J_{sc} ~ 10 mA/cm², the deposition was repeated under the same conditions. This time, an additional ZnO:Al layer was deposited on the cells before the Ag layer to ensure higher contact stability during the light soaking procedure.

Since the deposition parameters for the individual i-layers were the same as for the material studies, it is reasonable to assume that the optical band gap of the i-layers in the solar cells are similar to the ones found for the according materials. Slight differences might be possible due to the difference in the used substrate types that might introduce a slight difference in growth of the amorphous silicon.

4.3.2 Initial photovoltaic-parameters

The cell performance of the deposited amorphous single junction solar cells was measured by the solar simulator under standard conditions. The initial η, *FF,* V_{oc} and J_{sc} are presented by the close symbols in Figure 4.4 in dependence of the used silane concentration. The symbol shape refers to the used deposition temperature.

Efficiency η Figure 4.4 a) shows a slight decrease for the efficiencies of the high band gap cells with lower applied silane concentrations. With 8.1% and 8.6% the highest values were achieved by grading cells deposited at 200°C and 140°C, respectively. The lowest η of 7.1% was measured for the sample prepared at 140°C and *SC* = 1.5%. However, this value was still higher than the efficiency of the standard cell that achieved, due to the low open-circuit voltage, only 6.7%.

Fill factor *FF* As depicted in Figure 4.4 b) the fill factor decreases with applied silane concentration. Generally, the used lower *SC* made thicker i-layers necessary, which could cause the decrease in *FF*. The highest *FF* ~ 75% are reached by the two grading cells and the solar cell deposited with *SC* = 3.3%, which have similar thicknesses as the standard cell. The lowest value, which was found for the thickest sample deposited at the lowest *SC,* still amounts to ~ 68%.

Open-circuit voltage V_{oc} Significantly higher open-circuit voltages (Figure 4.4 c) are achieved by all high band gap solar cells compared to the standard cell, for which only 865 mV were measured. With decreasing silane concentration, V_{oc} increases continuously from 888 mV to 924 mV for solar cells deposited at 140°C and 110°C. Outstanding high values are reached by two grading cells (green symbols); the maximum open-circuit voltage of 937 mV is reached by combining the silane grading with a lower deposition temperature of 140°C.

Short-circuit current density J_{sc} Despite the previous thickness adjustment the short-circuit current density of the cells with ZnO:Al/Ag back reflector varied. The initial values ranged from 11.2 mA/cm² to 12.4 mA/cm² for the high band gap solar cells, but

only 10.6 mA/cm² were achieved by the standard cell. The small increase in J_{sc} compared to the sample with Ag-back reflector indicates that some other deteriorating effect, e.g., a not optimal ZnO:Al layer, occurred, which would also explain the low fill factor.

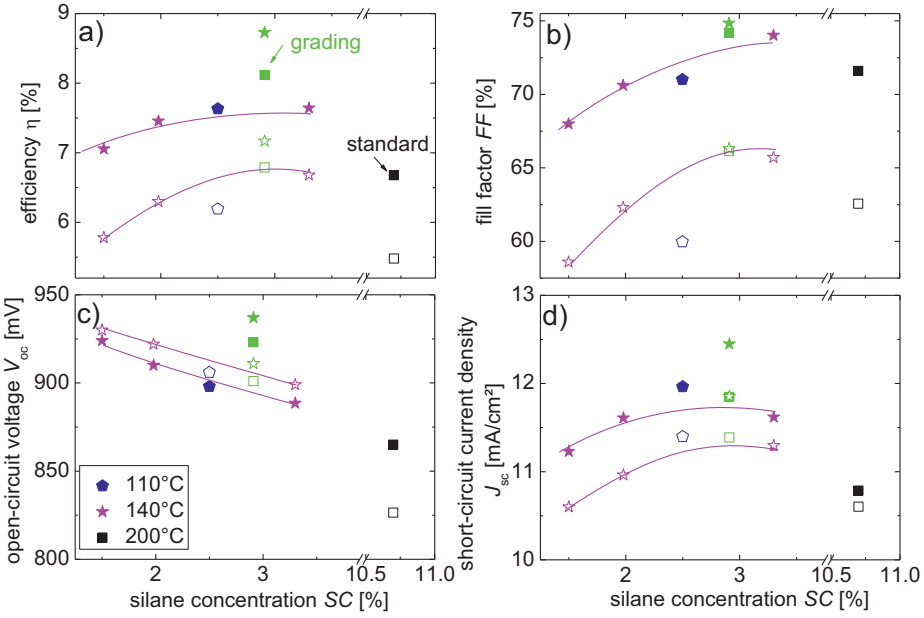

Figure 4.4 Initial (full symbols) and stabilized (open symbols) photovoltaic parameters for single a-Si:H cells with high band gap material as i-layer. The layer thicknesses and deposition conditions varied. Cells prepared with a silane grading are displayed by the green symbols. The dashed lines are guides to the eye.

4.3.3 Photovoltaic parameters after light-induced degradation

After light soaking for 1000 h under standard conditions the cell performance was measured with a solar simulator. Figure 4.4 a) – d) shows the results by open symbols.

Stabilized efficiency η_{stab} The grading cells, deposited at 200°C and 140°C stabilize to efficiencies of 6.8% and 7.2%, respectively, and exceed all other considered cells.

Due to a high degradation in fill factor and open-circuit voltage, the efficiency of the standard cell is only 5.5%.

The degradation rate for the three samples deposited at 140°C increases with decreasing silane concentration. The initial values of the sample deposited at 110°C fitted well into the 140°C-series. However, the values after light soaking are significantly lower indicating a higher degradation rate for the 110°C-sample which is in accordance to the theoretical consideration.

Stabilized fill factor FF_{stab} The fill factors, depicted in Figure 4.4 b) of the cells in the degraded state follow the trend of the initial values. A significant drop in *FF* is observed for the sample deposited at 110°C.

Stabilized open-circuit voltage $V_{oc,stab}$ The open-circuit voltages of the high band gap cells with constant *SC* increased after light soaking. The highest measured stabilized value of 930 mV was reached by the sample deposited with the lowest silane concentration of $SC = 1.5\%$ at 140°C. The stabilized values of the grading cells decreased after light soaking so that they fitted well into the *SC*-series although the initial open-circuit voltages were much higher. For the standard cell deposited at 200°C a high degradation was found leading to a stabilized open-circuit voltage of only 826 mV.

Increased, stabilized voltages for cells deposited at lower temperatures or low silane concentrations were previously reported by Rech [22], Wieder et al. [91] and Siamchai et al. [92], respectively. Rech reported on a suppressed surface recombination at the p/i-interface due to the higher band gap of the i-layer that acts as a barrier for electrons diffusing reverse to the photocurrent. Hence, the open-circuit voltage is increased. This enhancement, however, is limited by the hole recombination current. After degradation, the defect density in the bulk increases and the bulk recombination becomes V_{oc}-determined. The relation of surface to bulk recombination defines whether an increase or decrease of V_{oc} is observed.

Stabilized short-circuit current density $J_{sc,stab}$ The stabilized short-circuit current densities follow the same trend as the initial values as shown in Figure 4.4 d). The

lowest degradation rate is observed for the standard cell, however, due to a very low initial value the stabilized value is below all other considered solar cells.

Efficiency η depending on optical band gap E_{04} In Figure 4.5 the initial and stabilized efficiencies of the discussed cells are plotted as a function of the optical band gap E_{04}, which was determined for the i-layer material previously. As shown, it is possible to deposit a-Si:H solar cells with significantly higher band gaps compared to standard (E_{04} = 1.91 eV) that achieve high initial and stabilized efficiencies. Although the i-layers of the solar cells varied in thickness from 150 nm for the standard sample with E_{04} = 1.91 eV to 320 nm for E_{04} = 1.94 eV the degradation rate is very similar for all solar cells, which is derived from the difference between the initial and stabilized efficiencies.

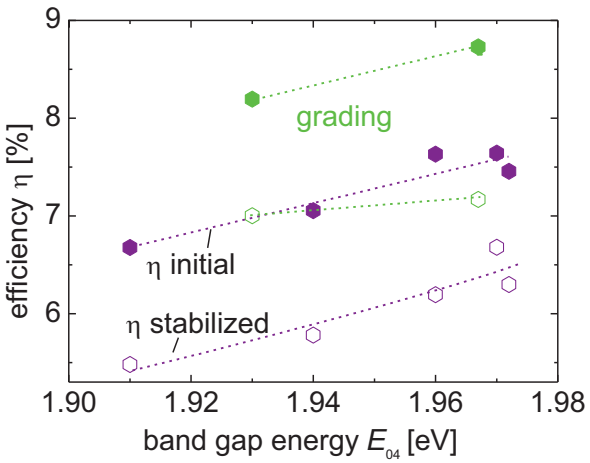

Figure 4.5 Initial (full symbols) and stabilized (open symbols) efficiencies for solar cells deposited under varying deposition conditions. The cells deposited with a SC-grading are pointed out by green symbols. The dashed lines are guides to the eye.

4.3.4 Summary

Amorphous single junction solar cells with high band gap (E_{04}) i-layer material that reach high stabilized open-circuit voltages and efficiencies were fabricated. The stabilized efficiency of the standard cell, which acted as reference, is 1.3% absolute lower than the stabilized efficiency of the grading cell at 200°C. At a deposition temperature of 140°C a sufficiently low degradation is kept when a low silane concentration ($SC < 3.3\%$) is used. With a further reduction to 110°C a high degradation rate is observed which, however, is still lower than the degradation rate determined for the standard cell. Outstanding high stabilized efficiencies of 7.2% and 6.8% are reached when applying silane grading at 140°C and 200°C.

For the thin solar cells with high band gap i-layers no increase in degradation rate is observed. The open-circuit voltage even increased for the solar cells deposited with constant low *SC* at lower temperatures after light-induced degradation.

In general, the stabilized values show the same trends as the initial ones: Efficiency, fill factor and short-circuit current density are at their maximum around a silane concentration of 3%, and the open-circuit voltage increases with decreasing *SC*. Although the layer thicknesses of the considered high gap solar cells increased from 160 nm to 320 nm with decreasing silane concentration the degradation rates for η, *FF,* and J_{sc} increase only slightly for lower silane concentrations.

4.4 Variation of window-p-doped layer

The following paragraph describes an adjustment of the window-p-doped layer in solar cells with high optical band gap absorber layers. Two i-layer deposition regimes were chosen for which the p-doped layer was adjusted individually by varying the deposition temperature and gas flow rates of the doping gases trimethylborane (TMB) and methane (CH_4). Initial and stabilized photovoltaic parameters are discussed.

Often, the deposition temperature of the i-layer, which is usually ~ 200°C, limits a reduction of the p-doped layer deposition temperature. The underlying p-doped layer is exposed to this temperature inevitable throughout the process. Therefore, a significant

reduction of the p-doped layer deposition temperature might be ineffective. A lower i-layer deposition temperature of 140°C bears the possibility to study the effect of a reduced p-doped layer deposition temperature.

4.4.1 Window-p-doped layer adjustment in thin high band gap single cells

The properties that a sufficiently working p-doped layer should exhibit are briefly discussed with special focus on the thin high band gap solar cells, followed by a description of the experiments that were carried out to adjust the p-doped to the i-layer.

Window-p-doped layer requirements The p-doped layer in a thin-film solar cell has to fulfill several important requirements. First, a high transparency is necessary to reduce parasitic absorption in the window-p-doped layer. Secondly, the electrical conductivity must be high in order to minimize the series resistance to the front-TCO. Thirdly, together with the n-doped layer an electric field must be built over the i-layer to extract the photogenerated charge carriers from there. The latter two demands are achieved by p-type doping by boron with adding Trimethylborane (TMB) or Diborane to the deposition gas mixture. High transparency, in turn, is achieved by high optical band gaps that are realized by the incorporation of oxygen or carbon when adding carbon dioxide (CO_2) or methane (CH_4) to the gas mixture. Also, a reduced deposition temperature leads to a higher band gap as it is predicted from the deposition of intrinsic a-Si:H. A balance between the boron doping, carbon alloying and deposition temperature must be found to realize an optimal window-p-doped layer.

Experimental details Based on the results in section 4.3 two different high band gap deposition regimes were chosen for p-doped layer studies. One cell, referred to as “Type A”, was deposited at 200°C with a silane grading during the deposition. For the second cell type (Type B) a constant silane concentration of 3.3% was used; the deposition temperature was 140°C. Some main properties of these two cell types are summarized in Table 4.1. The given band gap E_{04} values refer to the according i-layer material. The light-induced degradation rate of the efficiency is given by $\Delta\eta$.

Table 4.1 Summary of the main properties and deposition parameters for single junction a-Si:H cells with Type A and Type B i-layers that were used for the p-doped layer adjustment. The values for the standard cell are given as reference.

a-Si:H type	*SC* [%]	E_{04} [eV]	Δη [%]	$V_{oc,stab}$ [mV]	*d* [nm]	T_{depo} [°C]
standard	10.7	1.91	17.9	826	150	200
A	grad (2.9)	1.93	16.0	901	150	200
B	3.3	1.97	11.0	899	175	140

The following samples had only Ag-back contacts, which might have influenced the stability of the contacts during the light soaking procedure. Without the ZnO:Al layer the probability that the thin silver layers peel off increases. In addition, damage of the contact pads by the measuring tips is often observed and results easily in short-circuit for the very thin devices.

4.4.2 Temperature variation

As mentioned before a 25% longer deposition time of the p-doped layer for the grading cells has proven of value, and was also applied for the following experiments. An i-layer deposition temperature 60 K lower than standard had led to an increase in optical band gap energy and suggested a reduction of 60 K for the p-doped layer deposition temperature. Hence, a variation of TMB-flow rate (Q_{TMB}) and CH_4-flow rate (Q_{CH_4}) was carried out at 220°C, which is the standard deposition temperature, and at 160°C. For these first studies Type A i-layers were used. The results are displayed in Figure 4.6. The doping gas flow rates are normalized to the standard values.

Although fewer solar cells were fabricated with a p-doped layer deposited at 220°C a clear increase in open-circuit voltage is observed when the p-doped layer deposition temperature is reduced to 160°C. This applies for all combinations of TMB- and CH_4-flow rates. Using the standard flow rates at 220°C and 160°C during the p-doped layer deposition led to a V_{oc}-increase from 903 mV to 930 mV for Type A cells and an

increase from 865 mV to 888 mV for a 150 nm thick standard cell. Therefore, it is concluded that a decrease of p-doped layer deposition temperature leads to an increase in V_{oc}, and no deteriorating effect occurs when the following i-layer is deposited at higher temperatures.

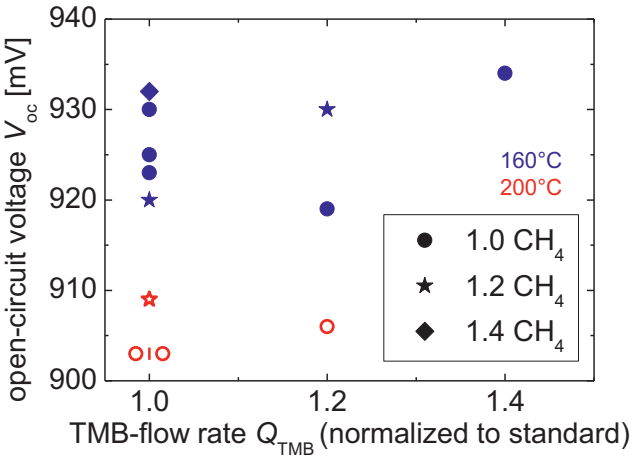

Figure 4.6 Open-circuit voltages for Type A solar cells with p-doped layers deposited at 220°C (red, open symbols) and 160°C (blue, full symbols) with different gas flow rates Q of CH_4 and TMB.

It is difficult to determine a trend in the behaviour of V_{oc} depending on TMB- or CH_4-flow rates. At a p-doped layer deposition temperature of 160°C the open-circuit voltages varied between 919 mV to 934 mV, whereas the highest value was reached when only the TMB-flow rate was increased by 40% (1.4 times the standard value). Also high values of 932 mV and 930 mV were achieved by only increasing the CH_4-flow rate and with the standard flow rates, respectively.

4.4.3 Influence of doping variation on initial and stabilized open-circuit voltage

The flow rates of the doping and alloying gases TMB and CH_4, respectively, were varied during the p-doped layer deposition at 160°C for Type A and Type B solar cells. The cells underwent the light soaking procedure for 1000 h. For comparison, a Type A

solar cell with a standard p-doped layer was investigated. Initial and stabilized open-circuit voltages are presented and discussed in the following section.

TMB-flow rate variation for Type A and Type B cells at 160°C The unclear trends of the initial values of V_{oc} for Type A i-layer were already discussed. The highest initial V_{oc} of 935 mV was reached when the highest TMB-flow rate was applied. After degradation, almost equal values of 903 mV, 904 mV and 908 mV are reached when the TMB-flow rate increased at standard CH_4-flow rate as shown in Figure 4.7. With the standard TMB-flow rate a stabilized efficiency of only 6.0% is reached whereas 6.75% are obtained at a TMB-flow rate 1.2 times higher than the standard value. The open-circuit voltage for the solar cell with Type A i-layer and standard p-doped layer at 220°C degraded from 903 mV to 890 mV due to light soaking.

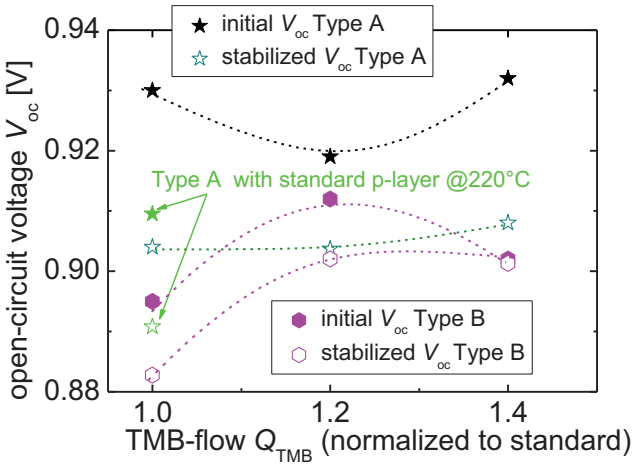

Figure 4.7 Initial (full symbols) and stabilized (open symbols) V_{oc} values for varying Q_{TMB} at standard CH_4-flow rate at 160°C for Type A (stars) and Type B (hexagon) a-Si:H cells. The green stars refer to the Type A cell with standard p-doped layer at 220°C. The lines are guides to the eye.

For Type B cells the highest open-circuit voltage of 912 mV and 902 mV in the initial and stabilized state, respectively, is achieved with a p-doped layer deposited at a 20% (1.2) higher Q_{TMB}. For a further increase to 1.4 times the standard flow rate V_{oc}

decreased to 902 mV and stabilizes with almost no degradation to 901 mV (Figure 4.7). A lower degradation rate of V_{oc} in the case of applying highly doped p-doped layers was also reported by Isomura [73]. After light soaking, the efficiency of the latter cell had decreased from 6.9% to 6.0%, which is the highest observed stabilized η-value for Type B cells. The Type B cell with a p-doped layer at standard flow rates reached only 895 mV initially, and showed the highest degradation rate, reaching a stabilized value of 882 mV.

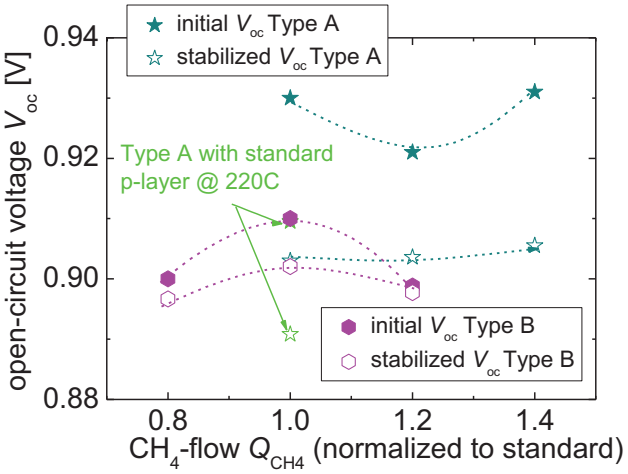

Figure 4.8 Initial (full symbols) and stabilized (open symbols) V_{oc} values for varying Q_{CH_4} at standard TMB-flow at 160°C for Type A (stars) and 1.2 times TMB-flow for Type B (hexagon) a-Si:H cells. The green stars refer to the Type A cell with standard p-doped layer at 220°C. The lines are guides to the eye

CH_4-flow rate variation for Type A and Type B cells at 160°C Using the standard TMB-flow rate Q_{CH_4} was varied from standard (1.0) up to a 40% (1.4) higher flow rates for Type A solar cells. It can be seen in Figure 4.8 that the open-circuit voltages follow no clear trend. High values of 931 mV were achieved when the CH_4-flow rate rose by 40% (1.4). The stabilized values of the CH_4- and TMB-flow rate variation are almost identical and reach values between 903 mV and 908 mV. The highest stabilized

efficiency is reached with Q_{CH_4} 1.2 times the standard value, amounting to 6.8% due to a high short-circuit current density.

For Type B cells, the CH_4-flow rate was varied by ± 20% at a 20% (1.2) higher TMB-flow rate based on the previously shown results. A decrease of V_{oc} from 910 mV to ~ 900 mV was observed, no matter if Q_{CH_4} was decreased or increased, but almost no degradation is noticed in the latter case. The highest (in the CH_4-flow rate series) stabilized efficiency of 5.9% was found for this cell.

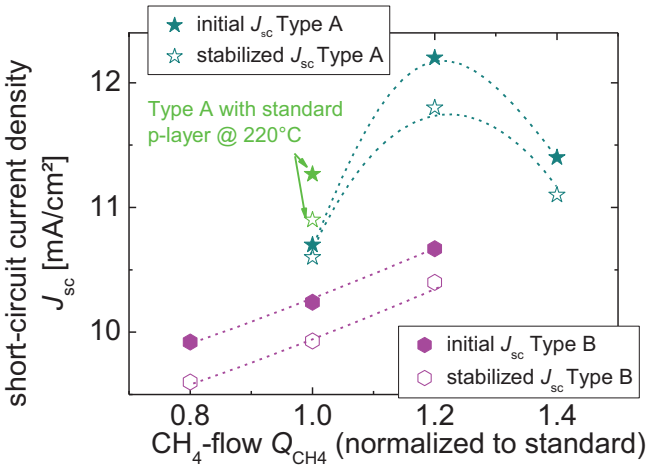

Figure 4.9. Initial (full symbols) and stabilized (open symbols) J_{sc} values for varying Q_{CH_4} at standard TMB-flow rate at 160°C for Type A (stars) and Type B (hexagon) a-Si:H cells. The green stars refer to the Type A cell with standard p-doped layer at 220°C. The lines are guides to the eye.

Figure 4.9 displays the short-circuit current density as function of the CH_4-flow rate for the solar cells presented in Figure 4.8. For the Type B cells, a clear linear increase in initial and stabilized J_{sc} with increasing Q_{CH_4} is observed. For Type A solar cells, first, an increase in J_{sc} for higher Q_{CH_4} is noticed, but at the highest flow rate J_{sc} decreases again.

The higher short-circuit current densities are explained by a widening of the band gap due to a higher carbon content. Consequently, the transparency of the p-doped layer increases and more light reaches the i-layer where more charge carriers are created and J_{sc} increases. The behaviour of the cell with the standard p-doped layer cannot be explained by its optical band gap. Due to the higher deposition temperature of the p-doped layer, the band gap should be lower and the parasitic absorption in the p-doped layer higher. Consequently, a lower J_{sc} would be expected.

For choosing the most suitable p-doped layer for Type A and Type B cells for further experiments it was focused on high stabilized open-circuit voltages combined with reasonable short-circuit current densities and fill factors. For Type A solar cells the highest stabilized V_{oc} and FF of 908 mV and 70.0%, respectively, were reached by using a p-doped layer with a 40% (1.4) higher TMB-flow rate at standard CH_4-flow rate. This p-doped layer was regarded as “optimized” for the Type A deposition regime.

The optimal p-doped layer for Type B solar cells was achieved with TMB- and CH_4-flow rates 1.2 times the standard. The lowest degradation in V_{oc}, accompanied with high stabilized η and J_{sc} of 5.9% and 10.4 mA/cm², respectively, were achieved.

In the following, the notation “Type A” and “Type B” solar or top cells include the adjusted p-doped layer if not mentioned unlike.

Comparison of optical band gaps The previous results show that an individual adjustment of the p-doped layer for the different i-layers leads to higher open-circuit voltages. It is assumed that one important determining factor is the difference in the optical band gap between the p-doped and i-layer. Therefore, the improved p-doped layers for Type A and Type B cells as well as the standard p-doped layer were deposited on Corning Glass for PDS measurements to determine the optical band gap. Besides the E_{04} band gaps the Tauc band gaps were determined graphically by the approach explained in subsection 2.1.1. The deposition time was the same as during the solar cell deposition.

The band gaps of the different p-doped and i-layers derived from the PDS-measurements are given in Table 4.2. The adjusted deposition parameters for Type A and Type B p-doped layers led to wider E_{04} and Tauc band gaps in comparison to the

standard p-doped layer. The higher CH_4-flow rate, compared to the deposition regimes for standard and Type A p-doped layers, explains the widest band gap of Type B p-doped layer.

Table 4.2 E_{04} and Tauc band gap of p-doped and i-layer for standard, Type A and Type B i-layers

Band gap	**Standard a-Si:H**	**Type A**	**Type B**
E_{04} p-doped layer [eV]	2.05	2.14	2.21
E_{04} i-layer [eV]	1.91	1.93	1.97
ΔE_{04} p-i-layer [eV]	0.14	0.21	0.24
Tauc band gap p-doped layer [eV]	1.80	1.90	1.94
Tauc band gap i-layer [eV]	1.76	1.79	0.11
ΔTauc band gap p-i layer [eV]	0.04	0.11	0.13

The differences of the p-doped and i-layer band gaps, ΔE_{04}- and ΔTauc, are given in the table as well. Their absolute values differs, but it can be seen that the differences in the band gaps of p-doped and i-layers are much smaller for the standard cell with the lowest stabilized open-circuit voltage (826 mV). In case of the Type A and Type B solar cells the differences were significantly higher which is assumed to be related to the higher stabilized V_{oc} values of 908 mV and 899 mV, respectively.

When the standard p-doped layer is combined with the Type A i-layer, the difference in Tauc band gap is only 0.01 eV. The solar cell that was deposited with this p-i-layer combination had a V_{oc} of 890 mV, almost 20 mV lower than with the adjusted p-doped layer. For the Type B i-layer the Tauc band gap is even higher than for the standard p-doped layer which is likely to cause a poor charge carrier separation.

The differences in the band gap between p-doped and i-layer have to be sufficiently high to reach high V_{oc} values. This barrier prevents photogenerated electrons to diffuse back into the i-layer and recombination is suppressed at the p/i-interface, V_{oc} increases [93]. Note that for the standard cell a thin undoped buffer layer with a *SC* of 3.85% is

used between the p-doped and i-layer to achieve this effect. This buffer layer was not used for high band gap solar cells.

4.4.4 Tandem cells with the optimized high band gap top cells

Deposition details The developed high band gap amorphous silicon solar cell of Type A and Type B were implemented into thin tandem cells, substituting a standard amorphous i-layer of ~ 80 nm. Based on the top cell short-circuit current density of the matched standard cell the i-layer of Type A and Type B top cells were adjusted in thickness. Since the optical properties of the different top cells vary, the bottom i-layer thickness had to be changed as well to find matching conditions. Slightly higher total cell thicknesses resulted from the adjustment of top and bottom i-layer thicknesses.

The tandem cells were characterized by the solar simulator and quantum efficiency measurements. The individual thicknesses of top and bottom i-layer were derived from the growth rate whereas the total thicknesses were measured by a profilometer.

Photovoltaic parameters Table 4.3 summarizes the photovoltaic parameters and the top and bottom cell short-circuit current densities, derived from *EQE* measurements. By exchanging the standard reference top cell with a Type A top cell V_{oc} of the tandem cell increases from 1369 mV to 1439 mV. This gain is similar to a V_{oc}-increase of 75 mV for the single a-Si:H cells, presented in subsection 4.3.2. A further V_{oc}-increase due to the use of the adjusted p-doped layer was probably inhibited by the use of thicker i-layers. When using a Type B top cell the V_{oc}-increase amounted only to 28 mV. The difference between the two according single solar cells had been 35 mV.

The tandem cells with high band gap top cells have higher $J_{sc,top}$, $J_{sc,bot}$ and J_{sc} than the tandem cell with standard top cell. This cannot be solely attributed to the different thicknesses since the bottom cell thickness of Type B tandem cell and the standard cell are similar. Despite having a higher band gap in the amorphous top cell, which usually leads to less absorption, the top cell current densities for Type A and Type B tandem cells were slightly higher. The high fill factor of the standard cell is attributed to the strong bottom cell limitation as explained in subsection 3.3.3.

Table 4.3 Photovoltaic parameters and short-circuit current densities derived from EQE measurements for a standard, thin tandem cell, compared to thin tandem cells with Type A and B top cells, optimized for high open-circuit voltages

Top cell type	η [%]	*FF* [%]	V_{oc} [mV]	J_{sc} [mA/cm²]	*d* [nm]	$J_{sc,top}$ [mA/cm²]	$J_{sc,bot}$ [mA/cm²]
Standard	8.15	74.4	1369	8.0	500	8.3	7.6
A	8.69	68.1	1439	8.87	590	8.6	8.5
B	8.56	70.9	1397	8.63	540	8.6	8.1

4.4.5 Summary

All deposited solar cells gained from the lower deposition temperature of the p-doped layer regarding the open-circuit voltage. A stabilized V_{oc} of ~ 905 mV for Type A solar cells was achieved independent on the doping gas flow rates. The most suitable p-doped layer in regards to the η, *FF* and J_{sc} was deposited with a 40% higher TMB- and standard CH_4-flow rate at a deposition temperature of 160°C.

Due to a low degradation rate of V_{oc} accompanied with high stabilized efficiencies and short-circuit current densities a p-doped layer deposited at 20% higher gas flow rates for TMB and CH_4 was regarded as optimized for Type B solar cells.

The E_{04} and Tauc band gaps of Type A and Type B p-doped and i-layers reveal higher values when the deposition temperature is reduced and, in case of the p-doped layers, the CH_4-flow is increased compared to the standard regimes. According to the present studies, it is assumed that higher differences between p-doped and i-layer band gaps for both, E_{04}- and Tauc, are preferable to reach high open-circuit voltages.

The aim to increase in the open-circuit voltage in thin tandem solar cells significantly by using a high band gap material is reached. An increase of ~ 70 mV and ~ 28 mV is accomplished when Type A and Type B top cells, respectively, substitute the standard top cell in a thin tandem cell with a thickness of < 600nm.

4.5 Influence of doped layer thickness on tandem cells

The following paragraph deals with the effect of reduced doped layer thicknesses on the performance of standard thick and different thin tandem cells. By reducing the thickness of the doped layers, on the one hand, the parasitic absorption is reduced and the short-circuit current density increases but, on the other hand, the built-in potential might be lowered. For thin devices, a lower built-in potential might still be high enough to separate photogenerated charge carriers and higher short-circuit current densities are observed without a considerable deterioration of open-circuit voltage and fill factor.

Four tandem cells with varying thicknesses and top cell designs were used to investigate the influence of reduced doped layers. First, only layers at the tunnel recombination junction (TRJ) are considered. Second, all doped layers including the front and back side were reduced.

4.5.1 Tunnel recombination junction (TRJ)

General aspects The tunnel recombination junction (TRJ) in a multijunction solar cell, briefly introduced in subsection 2.1.3, connects the two subcells, and consists of an n-type doped and a p-type doped part. In a-Si:H/μc-Si:H tandem cells photogenerated electrons created in the top cell are separated by the electrical field over the a-Si:H i-layer and drift to the n-doped layer. In the same way photogenerated holes are extracted in the μc-Si:H bottom cell and drift to the p-doped layer driven by the electric field. The inner n/p contact works as a back diode. The n-and p-doped layer at the tunnel recombination junction are heavily doped resulting in a broken band gap where conduction band electron states on the n-side are more or less aligned with valence band hole states on the p-side. In Figure 2.7, the band diagram of the tunnel recombination junction was already shown. Oppositely charged carriers tunnel through mid-gap or band tail defects and recombine [94]. This process is called non-localized recombination since both charge carrier types have to overcome part of the energy gap to reach the defect state where they recombine. A sufficiently high defect density is therefore required in the mid-gap to maintain a high recombination rate. Otherwise

dipoles are created by trapped electrons and holes leading to a weakening of the built-in potential over the i-layer [47]. Further demands on an optimized TRJ are ohmic behaviour under reverse bias and a low optical absorption.

The tunnel recombination junction in our standard a-Si:H/µc-Si:H tandem cell consists of an amorphous n-doped layer, a microcrystalline n-doped layer and a microcrystalline p-doped layer. Microcrystalline silicon has a higher doping efficiency and conductivity so that the requirements of a high doping and an ohmic-like behaviour are fulfilled. The amorphous n-doped layer is used to prevent the a-Si:H i-layer to be etched by the low silane containing hydrogen plasma during the µc-Si:H n-doped layer deposition.

Solar cell types for doped layer investigation In order to study the effect of a thickness reduction of the doped layers at the tunnel recombination junction four different tandem cell designs were investigated. Table 4.4 summarizes the differences in cell designs.

Table 4.4 Summary of the four tandem cell designs

Type	**p-doped layer**	**top i-layer**	d_{total} **[nm]**
Standard thick	Standard, $Q_{TMB,std}$, $Q_{CH_4,std}$	Standard a-Si:H	2300
Standard thin	Standard, $Q_{TMB,std}$, $Q_{CH_4,std}$	Standard a-Si:H	500
Type A	160°C, $Q_{TMB,A}$ =1.4 $Q_{TMB,std}$ $t_{depo,A}$= 1.25 $t_{depo,std}$	grading (2.9%)	590
Type B	160°C, $Q_{TMB,B}$ =1.2 $Q_{TMB,std}$, $Q_{CH_4,B}$ =1.4 $Q_{CH_4,std}$	SC = 3.3%	540

The bottom i-layer was deposited under identical conditions with varying deposition times. First, as references, the four tandem cells were equipped with a standard thick TRJ. Second, the deposition time of the three doped layers at the TRJ was reduced by 40%. The thickness of each doped layer, estimated by the deposition rate, was approximately ~ 20 nm for all types of doped layers. Consequently, a thickness

reduction by 40% should have led to a 24 nm thinner TRJ. Window-p-doped layer and the back n-doped layer remained unchanged. For the last experiment all doped layers, including the window-p-doped layer and the back-n-doped layer, were reduced by 40%. The total thickness reduction added up to 40 nm.

4.5.2 Influence of thinner doped layers on the performance of different tandem cell designs

Twelve different tandem cells were fabricated and analyzed in terms of η, *FF*, V_{oc} and J_{sc}. Figure 4.10 a) – d) summarizes the results. The numbers at the x-coordinate refer to the following cases:

case 1 – standard doped layers

case 2 – doped layers at TRJ reduced by 40%

case 3 – all doped layers reduced by 40%

Efficiency η As shown in Figure 4.10 a) the efficiency of the thick standard cell is unaffected by a thickness reduction of the doped layers. All thin tandem cells show higher efficiencies when only the TRJ thickness is reduced. For Type A tandem cells η increase even further when all doped layers are thinner. An efficiency increase from 8.7% to 8.9% was obtained; in both cases the matching condition was fulfilled.

Fill factor *FF* The behaviour of the fill factor, shown in Figure 4.10 b), for different tandem cell types is difficult to interpret. The reduction of the doped layers enhances the top and bottom cell current density individually. Therefore, the relation of $J_{sc,top}/J_{sc,bot}$ is changed which strongly influences the matching and, hence, the fill factor as it was explained in subsection 3.3.3. Considering bottom cell short-circuit current density limited tandem cells the thinner TRJ leads to an increase in $J_{sc,bot}$ and the ratio $J_{sc,top}/J_{sc,bot}$ is reduced. This leads to a shift towards matching, which would result in a decrease in *FF*, or even top cell short-circuit current density limitation, for which *FF* would increase. Since all four cells varied in matching at the starting point *FF* is influenced differently for each tandem cell design.

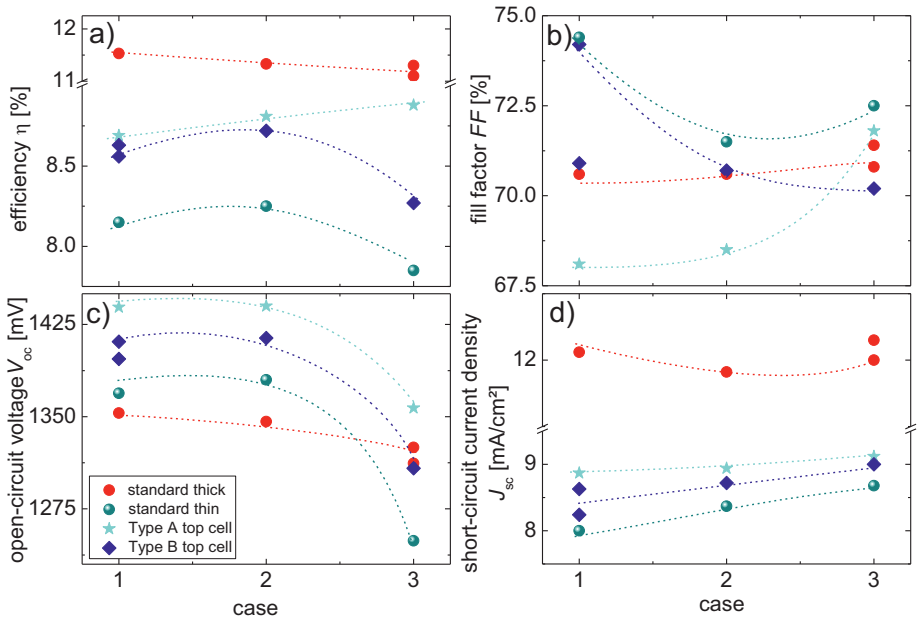

Figure 4.10 Photovoltaic parameters of four different tandem cell designs deposited with variation in doped layer thickness: standard (case 1), TRJ 40% reduced (case 2) and all doped layers 40% reduced (case 3). The dashed lines are guides to the eye.

Open-circuit voltage V_{oc} The behaviour of the open-circuit voltage for the four cell types depending on the different doped layer thicknesses (case 1 – 3) is depicted in Figure 4.10 c). For case 2, V_{oc} of the thin tandem cells does not change considerably but drops tremendously for case 3 when the window-p-doped layer and back-n-doped layer are reduced, too. The thin standard cell was affected most by the thickness reduction of the doped layers noticeable by a decrease in V_{oc} of $\Delta V_{oc} = 120$ mV. For Type A and Type B ΔV_{oc} amounted to 82 mV and 103 mV, respectively. The open-circuit voltages of the thick standard cells decrease slightly but continuously for case 2 and 3 with $\Delta V_{oc} = 28$ mV.

Short-circuit current density J_{sc} In general, due to the reduced doped layers more light reaches the i-layers, resulting in higher J_{sc} in the top and bottom cells. As it can be

seen in Figure 4.10 d) this effect applies for all thin tandem cell designs whereas for the thick standard cell no clear trend in J_{sc} is observed. As discussed already in subsection 3.3.5, the parasitic absorption, e.g., in doped layers, has a higher share for thin tandem cells than for thicker tandem cells. Therefore, a thickness reduction of the doped layers, to which a high parasitic absorption is attributed, affects the thin tandem cells much more than the thick one.

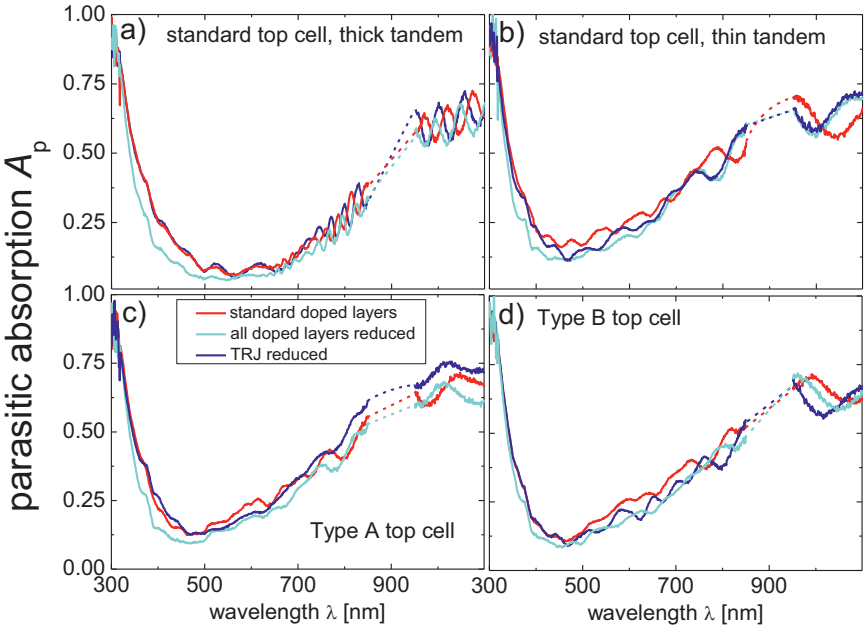

Figure 4.11 Parasitic absorption of four different tandem cell types that were deposited with a variation in doped layer thicknesses. For the region of the detector change no values are shown, the region is interpolated by the dashed lines.

Effect of thinner doped layers on parasitic absorption The parasitic absorption is attributed to absorption in the glass substrate, front-TCO, ZnO:Al back reflector and the doped layers. By reducing the thickness of the doped layers, a lower parasitic absorption A_p is expected. Figure 4.11 a) – d) displays the parasitic absorption derived from reflectivity and quantum efficiency measurements for the investigated four different tandem cell designs with varied doped layer thicknesses.

The effect of a reduced TRJ thickness on A_p is most visible in the wavelength range from 500 – 750 nm. For all three thin tandem cells a smaller parasitic absorption is found compared to the standard TRJ. However, the difference in parasitic absorption for the thick tandem cell is negligible. This is explained by the enhanced absorption in the i-layers and a small dependence on A_p in the doped layers. These observations go along with the results for $J_{sc,}$ discussed previously.

The decrease of the window-p-doped layer thickness leads to significant reduction of A_p in the low wavelength region (300 – 500 nm). For the Type B tandem cell, this decrease is less striking due to an already low parasitic absorption resulting from the high band gap of the p-doped layer (Table 4.2).

4.5.3 Summary

The influence of thinner doped layers on the performance of four different tandem cell designs was investigated. For a standard thick tandem cell with a total thickness of 2300 nm no significant deteriorating effect is observed, no matter if only the TRJ was 40% thinner or all doped layers. This is explained by the low dependence of the short-circuit current density on parasitic absorption.

For the thin tandem cells, the open-circuit voltage drops significantly when all doped layers are reduced by 40% which is not compensated by a higher short-circuit current density. However, by reducing only the doped layers at the tunnel recombination junction no deterioration in cell performance was observed.

The parasitic absorption is in agreement with the measurements of J_{sc}. The thin tandem cells exhibit a stronger reduction in A_p with decreasing doped layer thicknesses, indicating a stronger dependence on the doped layer thicknesses.

4.6 Thin tandem cells at high deposition rate

Besides reducing layer thicknesses, higher deposition rates lead to significant lower deposition times and, therefore, lower costs. The tandem cells presented in the following section are all prepared on texture-etched ZnO:Al, deposited on Corning Glass. The potential of several deposition time reducing approaches, e.g., application of

very thin absorber layers, high band gap a-Si:H top cells and adjusted doped layers, are combined with high deposition rate processes for microcrystalline silicon and the front-ZnO:Al. The studies of this section are partially published by Gordijn et al. [95; 96].

4.6.1 High deposition rate process for ZnO:Al and µc-Si:H

Deposition parameters and properties of ZnO:Al Both, standard ZnO:Al and high rate ZnO:Al were deposited at the IEF5-Photovoltaik. A radio frequency (RF)-process at 13.56 MHz was used to sputter the standard ZnO:Al from planar targets. The resulting deposition rate reached ~ 6 nm × m/min.

Furthermore, high deposition rate ZnO:Al layers were sputtered from a rotatable dual magnetron target (RDM), and deposited at a rate of R_d > 100 nm × m/min. An excitation frequency of 40.68 MHz was applied. The discharge power amounted to 10 kW/m. Compared to the standard ZnO:Al, which uses an 1 wt% Al_2O_3 target, a target with a lower Al_2O_3 concentration of 0.5 wt% was used to fabricate stoichiometric high deposition rate ZnO:Al.

In contrast to the standard ZnO:Al films, for which the rms-roughness lies between 130 – 150 nm, the rms-values for the films deposited at higher rates were only ~ 58 nm. Optical measurements showed a resulting lower haze but the total transmittance was slightly higher than for the standard films due to a lower doping concentration. Detailed information about ZnO:Al deposited at a high deposition rate is given by Zhu et al [97].

Deposition parameters of high rate µc-Si:H films The high deposition rate process for microcrystalline silicon was adapted from a previously developed process by Kilper et al. [98]. An excitation frequency of 40.68 MHz was applied which is three times the standard (13.56 MHz). It was observed that the process parameter for obtaining high quality µc-Si:H films shifted to higher silane concentrations and lower pressure compared to the 13.56 MHz standard process [83]. With a decreased pressure of 7 Torr and an increased power of 1 W/cm² a high deposition rate of ~ 1 nm/s without any deterioration of the material properties was achieved. For example, an efficiency of

9.2% accompanied with a high open-circuit voltage of 536 mV was achieved by a µc-Si:H single junction cell deposited at R_d = 1 nm/s [44].

4.6.2 Deposition details

The tandem cells which are discussed in the following were deposited on ZnO:Al due to the better performance compared to Asahi U, as it was shown in section 3.3. Texture-etched standard ZnO:Al and the described high deposition rate ZnO:Al were used as substrates. All µc-Si:H bottom cells were deposited applying the introduced high rate process at 40.68 MHz.

Four different thin tandem cells were investigated. In Table 4.5 the characteristic deposition parameters are summarized. As reference, a 600 nm thick tandem cell was deposited on standard ZnO:Al (1) and compared to a tandem cell on high rate ZnO:Al (2). Two more samples were deposited on standard ZnO:Al: one cell for which all doped layers were reduced by 40% (3) and a cell with a Type A top i-layer (without the adjusted p-doped layer according to section 4.4) (4).

The deposition times for sample (1) and (2) amounted to only ~ 36 min. A further reduction to 32 min was possible for sample (3) due to the use of thinner doped layers. Caused by the low silane concentration used for the Type A top i-layer the deposition rate was only 1 Å/s and, consequently, the deposition time increased to ~51 min. The total thicknesses for the cells ranged from 550 – 620 nm.

Table 4.5 Deposition conditions and properties of thin tandem cells with high rate bottom cells

	substrate	**doped layers**	**top i-layer**	**bottom i-layer**	t_{depo} **[hh:ss]**	d_{total} **[nm]**
1	std ZnO:Al	std	std	high rate	36:10	600
2	high rate ZnO:Al	std	std	high rate	36:10	600
3	std ZnO:Al	40% thinner	std	high rate	32:00	550
4	std ZnO:Al	std	Type A	high rate	51:10	620

4.6.3 Photovoltaic parameters before and after light soaking procedure

Initial photovoltaic parameters of fast deposited tandem cells For the reference cell on standard ZnO:Al, an open-circuit voltage of 1440 mV accompanied with a high fill factor of 75% was obtained resulting in an initial efficiency of 9.5%. A lower V_{oc} and *FF* was measured on the high rate ZnO:Al which was balanced by a much higher short-circuit current density leading to a slightly higher efficiency of 9.6%. The same high J_{sc} was achieved by sample (3) due to a lower parasitic absorption in the thinner doped layers. The thickness reduction of the doped layers had only a small deteriorating effect on V_{oc} and *FF*, consequently η rose from 9.5% to 9.9%, compared to sample (1).

Due to the high band gap of the in Type A i-layer (4) a significantly higher V_{oc} of 1462 mV was accomplished leading to an initial efficiency of 9.7%. Comparing the performance of sample (4) with a tandem cell of similar thickness having Type A top cell (including adjusted p-doped layer) (comparing Table 4.3) a gain of ~ 20 mV in V_{oc} is noticed. The same J_{sc} were found on ZnO:Al and Asahi U for these two samples which confirms that the cell performance can be maintained if high rate μc-Si:H in thin tandem cells is used. It is also derived that the use of ZnO:Al instead of Asahi U as substrate enhances V_{oc} which led to an increase in efficiency from 8.7% on Asahi U to 9.7% on ZnO:Al in the discussed case.

Table 4.6 Initial photovoltaic parameters of different fast deposited tandem cells with a high rate μc-Si:H bottom cell

Remarks	**η [%]**	***FF* [%]**	**V_{oc} [mV]**	**J_{sc} [mA/cm²]**
(1) On std ZnO:Al	9.5	74.9	1440	8.8
(2) On high rate ZnO:Al	9.6	70.9	1410	9.6
(3) 40% thinner doped layer	9.9	71.7	1422	9.7
(4) Type A top i-layer	9.6	72.2	1462	9.1

Due to the high rate deposition process for the µc-Si:H bottom cell and the very thin doped and intrinsic layers a significant deposition time reduction was achieved with low losses in efficiency compared to the standard thick device. For example, only 9% less efficiency was noticed for a remarkable silicon deposition time reduction of 70%. By taking the reduced deposition time for the front-TCO in consideration the preparation time for the whole device decreases even further.

Stabilized photovoltaic parameters of the fast deposited cells The described solar cells underwent the light soaking procedure carried out under standard conditions. The photovoltaic parameters were monitored regularly in logarithmic time steps for 1000 h. The degradation behaviour of the tandem cells can be seen in Figure 4.12 a) – d).

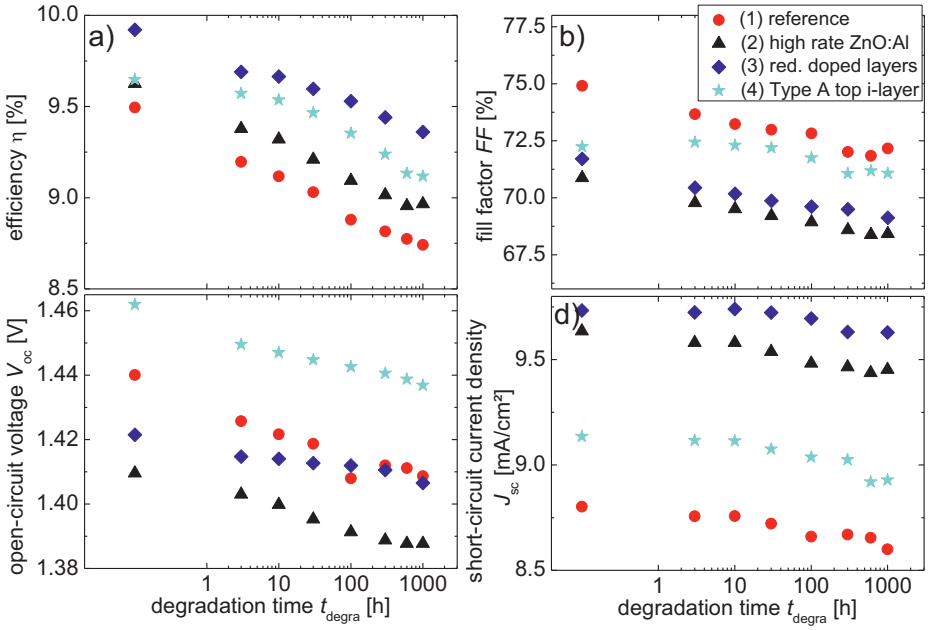

Figure 4.12 Degradation behaviour of four fast deposited thin tandem cells with high rate µc-Si:H bottom cells

The degradation of the 600 nm thick tandem cells on ZnO:Al exhibited a low value of only 7% – 8%, no matter if standard or high rate type was used. The efficiencies stabilized to 8.7% and 9.0%, respectively.

After degradation, still no deteriorating effect of thinner doped layers on V_{oc} and FF is found by comparing sample (3) with the reference sample (1). A low degradation of 5.6% leads to a stabilized efficiency of 9.4%.

With 1437 mV the highest stabilized V_{oc} was reached by the Type A top i-layer tandem cell which is ascribed to the higher band gap of the amorphous silicon. Noteworthy is the low degradation rate of 5.5% resulting in an efficiency of 9.1% after light soaking. The stabilized photovoltaic parameters are summarized in Table 4.7.

Table 4.7 Stabilized photovoltaic parameters of different fast deposited tandem cells with high rate µc-Si:H bottom i-layers

Remarks	**$\Delta\eta$ [%]**	**η_{stab} [%]**	**FF_{stab} [%]**	**$V_{oc,stab}$ [mV]**	**$J_{sc,stab}$ [mA/cm²]**
(1) On std ZnO:Al	7.9	8.7	72	1409	8.6
(2) On high rate ZnO:Al	6.9	9.0	68	1388	9.5
(3) 40% thinner doped layer	5.6	9.4	69	1407	9.6
(4) Type A top i-layer	5.5	9.1	71	1437	8.9

4.6.4 Summary

All four thin tandem cells on ZnO:Al show very low degradation rates between 5.5% and 8% compared to ~ 15% for standard thick tandem cells.

The high rate deposition of microcrystalline silicon had no negative influence on the device performance, which was confirmed by high stabilized efficiencies in the range of 8.7% – 9.4%. In case of very thin devices the bulk recombination is reduced and the influence of a higher defect density in high deposition rate µc-Si:H is assumed to be negligible.

By optimizing the doped layer thicknesses for a thin device, an increase in short-circuit current density accompanied with a maintained high V_{oc} results in an increase in stabilized efficiency from 8.7% to 9.4%

The reduction of deposition time, achieved by the use of very thin absorber layers, high rate sputter process for ZnO:Al, high rate deposition process for µc-Si:H and the optimization of the doped layers is successfully shown. A significant decrease in deposition time was found without deteriorating effects on the device performance.

4.7 Conclusion

Very thin a-Si:H/µc-Si:H tandem solar cells with total thicknesses below 600 nm were introduced in chapter 3. The tremendously reduced i-layer thicknesses of top and bottom cell compared to the standard thick tandem device opened up different ways to improve the cell performance or to reduce the deposition time that both lead to cost reduction.

Thick tandem cells aim at high short-circuit current densities and the use of high band gap material would make very thick amorphous layers necessary that show high degradation. Thin tandem cells, however, bear the potential of very high open-circuit voltages and high band gap a-Si:H material was suggested for the implementation as absorber material in the top cell. Reducing the deposition temperature by 60 K and 90 K, and simultaneously applying much lower silane concentrations led to device-quality a-Si:H with higher optical band gaps. The latter was confirmed by PDS and conductivity measurements on a-Si:H intrinsic layers. Single junction solar cells with high band gap material as i-layer exhibited high open-circuit voltages, which partially increased after degradation. The highest stabilized open-circuit voltage of V_{oc} = 930 mV was reached for a cell with a band gap of 1.97 eV. Cells deposited with a non-constant silane concentration (“grading”) show outstanding good cell performances with stabilized efficiencies up to 7.2% having a thickness of 160 nm.

An individual adjustment of the window-p-doped layer leads to an additional improvement in open-circuit voltage, which was exemplarily shown for two high band gap deposition regimes.

Finally, the two top cell types including adjusted p-doped layers were implemented in thin tandem cells with total thicknesses below 600 nm. An increase in open-circuit voltage of 70 mV compared to a thin tandem cell with a standard a-Si:H top cell was achieved. Besides the standard thickness of the doped layers, the influence of thinner doped layers was presented for three different thin tandem cells and a thick reference cell. It was found that a thickness decrease of the tunnel recombination junction by 40% results in slightly higher efficiencies in the thin tandem cells due to a reduced parasitic absorption in the tunnel recombination junction. The effect on the thick cells was negligible because of their low sensitivity on parasitic absorption.

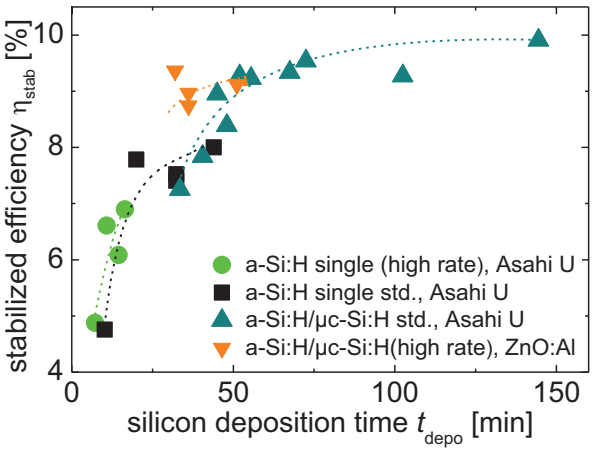

Figure 4.13 Comparison of different cell concepts regarding stabilized efficiencies depending on deposition time

Different approaches to reduced the deposition time such as applying significantly thickness reduced i-layers, reduced doped layer thicknesses and high deposition rate processes for microcrystalline silicon and the as front-TCO used ZnO:Al were combined. Promising results are achieved: A cell with a total thickness of only 550 nm with a significantly reduced deposition time by ~ 70% had a stabilized efficiency of 9.4%.

Since deposition time is directly related to the production costs, it is a crucial factor from industrial point of view. In Figure 4.13 the discussed thin tandem cells on Asahi U and ZnO:Al are compared with amorphous silicon based single junction cells prepared by the same deposition system regarding stabilized efficiencies and deposition times. The highest stabilized efficiencies are reached at deposition times around ~ 40 min by a-Si:H/µc-Si:H tandem cells with at high rate deposited µc-Si:H and very thin silicon layers. Tandem cells with the high gap top cells, which were partially deposited at lower temperatures, are not considered in this graphic. A further decrease in preparation time due to shorter heating up times with an increase in efficiency is possible.

Very thin a-Si:H/µc-Si:H tandem cells show much smaller sensitivity against defect-rich materials than standard thick cells. which makes the application of high rate microcrystalline silicon deposition and a reduction of deposition temperature possible. This, in turn, offers the possibility to reduce the production cost of solar modules.

Chapter 5

Thin n-i-p tandem cells on different substrates

The principle of very thin absorber layer thicknesses was applied on glass based, randomly structured substrates, and periodically structured aluminum plates in the n-i-p configuration. The anodization process that was used to structure the Al plates is described. The application of these Al substrates in n-i-p solar cells is evaluated by means of morphology and reflectivity measurements on all substrates. Exemplarily, the performance of tandem cells with total i-layer thicknesses of $d \sim 1350$ nm and $d \sim 650$ nm on the three substrate types is presented and the matching behaviour is discussed. Structural investigations revealed possible reasons for the significantly lower open-circuit voltages of thin tandem cells on Al. Finally, the influence of a reduced crystallinity of the µc-Si:H i-layer is investigated, and the suitability of structured Al plates as substrate for thin tandem cells in the n-i-p configuration is evaluated.
The experiments were carried out during a six month stay at AIST, Tsukuba, Japan.

5.1 Introduction

The deposition sequence of n-i-p solar cells starts facing the side from which the light enters the device. Therefore, a wider field of possible substrates opens up and in addition non-transparent materials can be used. Often, metal foils or low-cost organic polymers, e.g., polyimide (PI), polyethylene terephtalate (PET), polyethylene naphtalate (PEN) [99] are applied which are also flexible and lightweight [100]. Thus, the roll-to-roll-technique is applicable which allows a high throughput [101]. A drawback of the plastic materials is their low melting point that limits the deposition temperature, which is usually around 200°C for amorphous and microcrystalline silicon.

As back reflector, a combination of a metal layer (e.g. Al or Ag) and a ZnO layer is often deposited on the substrate. To ensure sufficient light trapping this stack has to have a certain roughness, which can be introduced by etching the ZnO or by structuring the substrate itself. For example, a random surface structure on PET is realized by an oxygen plasma treatment and a subsequent deposition of Ag/ZnO:Al [102].

Besides random structures, periodical gratings are suggested for efficient light trapping [103; 104; 105]. For example, pyramids and inverted pyramids were tested successfully as back reflector. Also, square-step gratings etched on glass by a photolithographic process and covered by Al/ZnO:Al were investigated [102]. However, there is still controversy about the optimum morphology of the back reflector and if the substrate should exhibit a random or a periodical structure. However, it is known that there has to be a trade-off between light scattering and the losses on the back reflector due to surface plasmon absorption in rough metallic films [106]. Nevertheless, on PEN, which exhibits a periodical, pyramidal surface after being structured by a hot embossing process, a stabilized efficiency of 9.8% for a tandem cell with a 2.5 μm thick bottom cell was demonstrated [107].

Recently, a new periodically textured back reflector for microcrystalline single junction solar cells in the n-i-p configuration was presented [108]. Aluminum substrates are patterned by anodic oxidation with the advantage that the period size of the structure is process controlled. The good light trapping and usability of these substrates had

already been proven for single junction cells, confirmed by an increase in J_{sc} from 22.5 mA/cm² on Asahi U to 24 mA/cm² on Al for a microcrystalline i-layer thickness of 1 µm [108]. According to this result, textured Al is suggested as substrate for thin tandem solar cells. Especially cells with very thin absorber layers require good light trapping to achieve sufficiently high short-circuit current densities.

Therefore, the concept of applying very thin absorber layers in tandem cells, transformed in n-i-p configuration, might benefit from the excellent light trapping ability of the structured Al, leading to a high short-circuit current density and efficiency.

5.2 Substrate preparation and characterization

Tandem cells were deposited on coated Asahi U, texture-etched ZnO:Al (fabricated at IEF5-Photovoltaik) and textured Al plates. The anodization process, which induces a self-ordered texture on polished aluminum plates, is presented in the following. Aluminum doped zinc oxide substrates were wet-etched in hydrochloric acid solution. After structuring the substrates were covered with a layer stack consisting of silver (Ag) and gallium doped zinc oxide (ZnO:Ga) as back reflector. The DC-sputter process is described and the morphological and optical properties of the so prepared substrates are discussed concerning solar cell application.

5.2.1 Substrate preparation

Structuring of Al The electrochemically polished Al sheets underwent an anodic oxidization process. Different electrolytic solutions, e.g., oxalic, phosphoric or citric acid, were used. For the anodization processes, constant voltages between 40 V and 370 V were applied and the temperature was controlled. At random positions on the Al-surface pores with a broad size distribution start to nucleate. The pore structure is attributed to mechanical stress: During the formation of alumina (Al_2O_3) the volume expands by almost a factor of two since the atomic density of Al in Al_2O_3 is lower than in metallic Al. The oxidation takes place at the whole surface so that an expansion can only occur vertically. The existing pore walls push upwards and due to repulsive forces between neighbouring pores, a two-dimensional, hexagonal, densely packed pore array

develops. The applied voltage and the type of electrolyte solution influence the pore size, namely period Λ, during the anodization [109; 110; 111]. Since the formation of the structure is self-ordered, a high uniformity over large areas is achieved.

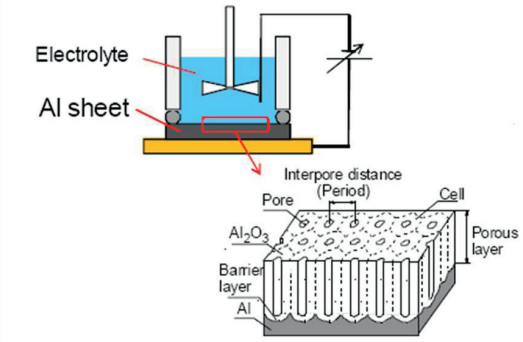

Figure 5.1 Scheme of the anodization process of the Al plates and the resulting pore array [112]

At the Al/Al_2O_3 interface, a self-ordered dimple pattern is formed as it can be seen in Figure 5.1. The Al_2O_3 layer is etched off with a chromium and phosphoric acid solution leaving a periodically structured Al surface.

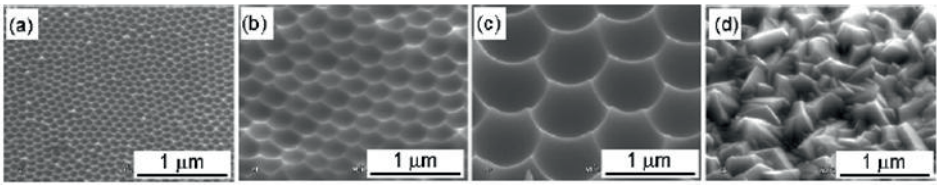

Figure 5.2 SEM images of structured Al substrates prepared with different applied voltages during the anodization. Different period sizes Λ are obtained. a) 40 V, Λ=0.1 µm b) 120 V, Λ=0.3 µm c) 370 V, Λ=0.9 µm d) Asahi U [113]

The SEM images in Figure 5.2 a – c) illustrate the increase of Λ with increasing voltages. Consequently, a preferred period is gained by adjusting the applied voltage and the type of electrolyte. For comparison, the random pyramidal structure of Asahi U is shown Figure 5.2 d).

The investigated tandem cells were deposited on Al substrates with a feature width (period) of Λ = 0.9 µm and feature height h =0.18 µm leading to an aspect ratio h/Λ of 0.2. The rms-roughness amounted to ~ 70 nm. These values are shown in Table 5.1 together with the values for Asahi U and texture-etched ZnO:Al. Since the latter two substrate types exhibit random structures feature height and width vary in the given ranges, and they are characterized by statistic values like rms-roughness. The opening angle θ includes the surface normal and the growth direction. Due to the U-shape morphology of the Al dimples, no opening angle can be determined.

Table 5.1 Structural properties for blank Asahi U, texture-etched ZnO:Al and patterned Al

	feature height *h* [µm]	**feature width Λ [µm]**	**roughness rms [nm]**	**opening angle θ [°]**
Asahi U	~ 0.1	~0.2 - 0.3	~ 40 nm	~ 37°
tex.-etch. ZnO:Al	~ 0.1 - 0.5	~0.5 - 2.0	~ 120 nm	~ 20°
patterned Al	0.18	0.9	~ 70 nm	

Substrate coating Besides the described Al plates, texture-etched ZnO:Al and Asahi U were used as substrates for tandem solar cells in n-i-p configuration. The ZnO:Al substrates were wet-etched by 0.5% HCl as described in subsection 2.2.1. Asahi U substrates were cleaned with SemiconClean (Tetramethylammoniumhydrat) for 10 min in an ultrasonic bath. After rinsing with deionized water and another 10 min in deionized water in an ultrasonic bath the substrates were dried by gaseous nitrogen and, wrapped in Al-foil, in an oven. Before the silicon deposition, all three substrate types were coated with a Ag/ZnO:Ga back reflector. For thick n-i-p cells (d_i = 1350 nm) 200 nm Ag and 40 nm ZnO:Ga were deposited without vacuum break by DC-sputtering. The very thin tandem and single junction cells required a thicker ZnO:Ga layer of 100 nm because a high shunt density was observed when only 40 nm ZnO:Ga were used. The substrates were mounted in a horizontal rotating table facing the target below. The process was carried out at room temperature. Argon was used as sputter gas.

The applied power amounted to 100 W and 200 W for sputtering Ag and ZnO:Ga, respectively.

5.2.2 Substrate properties

Surface morphology The surfaces of the Ag/ZnO:Ga coated Asahi U, ZnO:Al and Al substrates were investigated by means of SEM images. For this purpose, it was necessary to sputter a very thin platinum layer on the top of the 100 nm thick ZnO:Ga layer to avoid accumulation of electrical charges.

Table 5.2 SEM images of Asahi U, texture-etched ZnO:Al and patterned Al: blank, covered with 200 nm Ag/40 nm ZnO:Ga and 200 nm/100 ZnO:Ga [112]

	Asahi U	**texture-etched ZnO:Al**	**patterned Al**
*	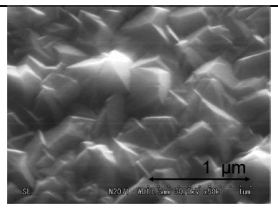	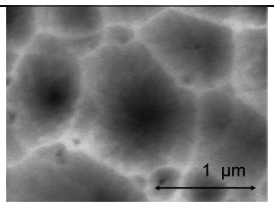	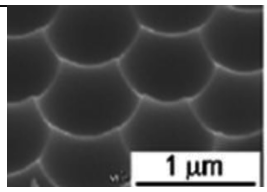
**	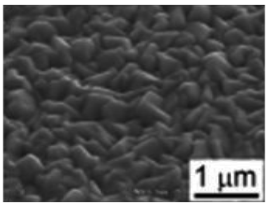		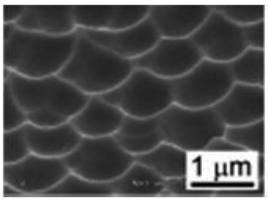
***	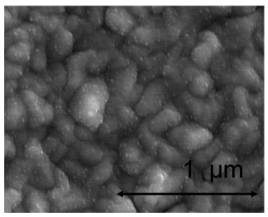	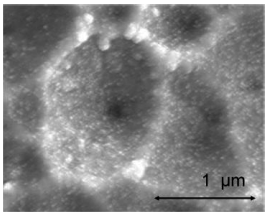	

* uncoated; ** 200 nm Ag/40 nm ZnO:Ga; *** 200 nm Ag/100 nm ZnO:Ga

In Table 5.2, the morphologies of blank Asahi U, texture-etched ZnO:Al and patterned Al are compared to morphologies of the substrates coated with 200 nm Ag/40 nm ZnO:Ga and 200 nm Ag/100 nm ZnO:Ga. In case of Asahi U, the deposition of the back reflector led to a rounding of the previously shown structure of sharp pyramids, which is more pronounced when a thicker ZnO:Ga layer is deposited. For the ZnO:Al substrate, the crater-like structure of the blank substrate is still visible and shows only a minor change when 200 nm Ag/100 nm ZnO:Ga are sputtered on the surface. But similar to the Asahi U substrate the sharp edges of the craters are rounded due to the Ag/ZnO:Ga layer.

The SEM image of the Al substrate as it was used for thick tandem cells (coated with 200 nm Ag/40 nm ZnO:Ga) exhibits a dimple structure very similar to the uncovered substrate. Due to the wide structure it is assumed that also with additional 60 nm ZnO:Ga layer, as used for the thin solar cells, the morphology is not strongly affected. However, when comparing the cell performance on Asahi U substrates the different ZnO:Ga thicknesses have to be considered.

Reflectivity of coated ZnO:Al, Asahi U and Al substrates The total and diffuse reflectivity (R_{total}, R_{diff},) were measured for the three different substrate types coated with 200 nm Ag/100 nm ZnO:Ga, and are presented in Figure 5.3. The curves show the reflectivity for the interface ZnO:Ga/air, which is not the actual situation that appears in the solar cell. The low diffuse reflectivity of the Asahi U substrate is attributed to internal light trapping. Due to the low refractive index of air (n = 1), light is diffracted at the steep side walls of the pyramid into the ZnO:Ga layer. However, in a solar cell where the adjacent layer is silicon with a refractive index of n = 3.5 this internal light trapping does not occur and the light is scattered into the silicon layer. The feature sizes of ZnO:Al and Al are much larger and the angles of the craters less steep. No internal light trapping occurs. The highest total reflectivity over the whole considered wavelength range is observed for the texture-etched ZnO:Al substrate with a high share of diffusely reflected light, which is preferable to increase the optical path length in thin μc-Si:H layers [113].

The aluminum substrate reflects about 80% of the incident light with a high amount of diffusely reflected light. Eye-catching is the steep ascent in the infrared region in total reflectivity for the Asahi U substrate accompanied with a strong decrease of diffuse reflectivity. This behaviour can be attributed to the small feature size. Light is most effectively scattered by structures that have feature sizes in the wavelength region of the light [106].

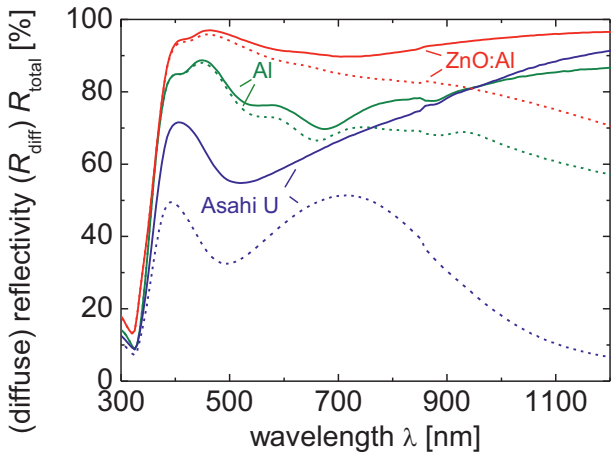

Figure 5.3 Diffuse (dashed curves) and total (straight curves) reflectivity of the substrates used for thin n-i-p tandem cells (coated with 200 nm Ag/100 nm ZnO:Ga)

According to optical simulation a period of $\Lambda > 0.3$ µm is required to generate diffracted light inside µc-Si:H in the near-infrared region. [114]. This requirement applies for Al and ZnO:Al substrates since their period amounts to ~ 0.9 µm and 0.5 – 2 µm, respectively, whereas Asahi U exhibits a lateral size of only 0.2 – 0.3 µm. Thus, the light scattering effect in Asahi U is assumed to be less effective as for the Al and ZnO:Al substrates.

5.2.3 Summary

The coating of the substrates with the Ag/ZnO:Ga back reflector rounded the sharp etches of all three introduced substrate types. The influence of the coating on the

morphology is low for ZnO:Al and Al substrates while the rounding of the sharp pyramids of Asahi U substrates resulted in a significant change in appearance.

According to the reflectivity measurements a sufficient light scattering ability over a wide wavelength range is found for self-orderly textured Al and texture-etched ZnO:Al, which should lead to high light trapping in the bottom cell.

5.3 Tandem cells in n-i-p configuration on different substrates

Tandem cells with different i-layer thicknesses were deposited on the three introduced substrate types. The influence of a periodically structured back reflector on thin (total i-layer thickness $d_i \sim 650$ nm) and standard thick (total i-layer thickness $d_i \sim 1350$ nm) tandem solar cells is evaluated and discussed in the following. A comparison to randomly structured back reflectors, one with a similar (ZnO:Al) and a much smaller (Asahi U) feature size is made.

5.3.1 Sample description

Preparation of tandem cells Based on previous results on tandem cells fabricated at AIST a combination of top and bottom cells with i-layer thicknesses of 350 nm and 1000 nm, respectively, was chosen as standard thick device. By reducing the deposition time for the i-layers, thin tandem cells were deposited under the same conditions. The thicknesses were derived from the deposition rate and time, and amounted to 150 nm and 500 nm for top and bottom i-layer, respectively. The deposition on Asahi U, ZnO:Al and Al plates were carried out in the same deposition run. The substrates were coated with 200 nm Ag and 40 nm or 100 nm ZnO:Ga for thick and thin tandem cells, respectively.

Silicon deposition by cluster tool PECVD The preparation of the n-i-p tandem cells were carried out in a cluster tool PECVD system at AIST suitable for four 5×5 cm² substrates, which were horizontally aligned between two electrodes. The deposition parameters were adapted from the standard processes used at AIST for the individual

layers since they had proven of value. Intrinsic, n-type and p-type doped layers were fabricated in different chambers to prevent cross contamination. Amorphous and microcrystalline i-layers were deposited with an excitation frequency of 13.56 MHz at 180°C. The process gases were let into the 20 mm wide electrode gap by cross flow. The deposition parameters are summarized in Table 5.3.

Table 5.3 Deposition parameters for a-Si:H and µc-Si:H intrinsic layers

deposition parameter	**a-Si:H**	**µc-Si:H**
pressure p [Torr]	1	1.5
power density P/A [W/cm²]	0.024	0.4
deposition rate R_d [Å/s]	2.5	1.4
silane concentration SC [%]	16.7	2.68
electrode gap d_e [mm]	20	20
excitation frequency ν [MHz]	13.56	13.56
temperature T [°C]	180	180

Antireflection coating and contacting Subsequently after the Si deposition a ~ 75 nm layer of indium tin oxide (ITO) was RF-sputtered through a shadow mask as antireflection coating on the samples. The overlapping silicon was etched off by a Reactive Ion Beam (RIE) process with O_2/SF_6-plasma to avoid current collection from outside of the defined solar cell area when determining the photovoltaic parameters. After the RIE process, Ag grids were sputtered through a shadow mask onto the ITO-covered areas yielding eight solar cell areas of 1×1 cm². One pad, which was not contacted by silver, was used for cell reflectivity measurements.

To improve the conductivity to the back contact it was metalized with platinum at the edges by applying a soldering gun. Finally, the solar cells were annealed for 2 h 10 min at 200°C in vacuum. A typical test cell configuration is displayed in Figure 5.4.

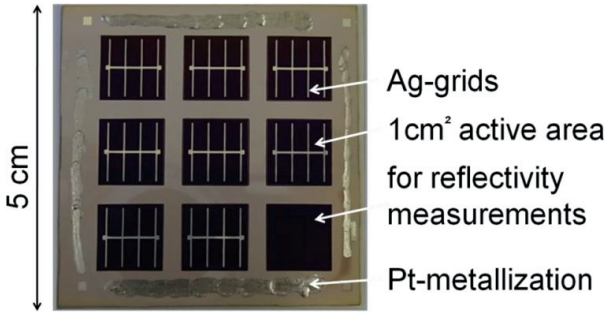

Figure 5.4 Top view of n-i-p test solar cell after processing

5.3.2 Tandem cell performance

After the final annealing step, the photovoltaic parameters and quantum efficiency of the tandem solar cells were determined under standard conditions (AM1.5, 100 mW/cm², 25°C). The *EQE* curves are presented in Figure 5.5. The according subcell short-circuit current densities are summarized together with the photovoltaic parameters in Table 5.3.

Influence of substrate morphology and i-layer thickness on short-circuit current density Figure 5.5 shows the top and bottom quantum efficiency characteristics, as well as their summation for the thick (Figure 5.5 a)) and thin (Figure 5.5 b)) tandem cells on coated Asahi U, texture-etched ZnO:Al and patterned Al. Almost identical top cell quantum efficiency curves were measured for the standard thick tandem cell on the different substrates. Top cell short-circuit current densities of ~ 11.5 mA/cm² were determined. Clearly higher bottom cell quantum efficiencies for both tandem cells on Al are observed, which indicates good response in the infrared region. A broader variation in top cell short-circuit current densities between 8.6 mA/cm² and 9.2 mA/cm² is observed for thin tandem cells. The *EQE* characteristic of the top cell on Al runs significantly below the characteristics for top cells on Asahi U and ZnO:Al.

The sum of $J_{sc,top}$ and $J_{sc,bot}$ amounts to 18.3 mA/cm² on Al which is slightly higher compared to Asahi U (18.2 mA/cm²) and ZnO:Al (18.0 mA/cm²). For the thick devices the gain in $J_{sc,top} + J_{sc,bot}$ on Al substrates was more pronounced and amounted to

1 mA/cm² and 0.7 mA/cm² compared to tandem cells on ZnO:Al and Asahi U, respectively. The higher current generation in the bottom cell on Al substrates might be due to better light trapping, caused by the U-shaped surface, or by a higher crystalline volume fraction in the µc-Si:H absorber material.

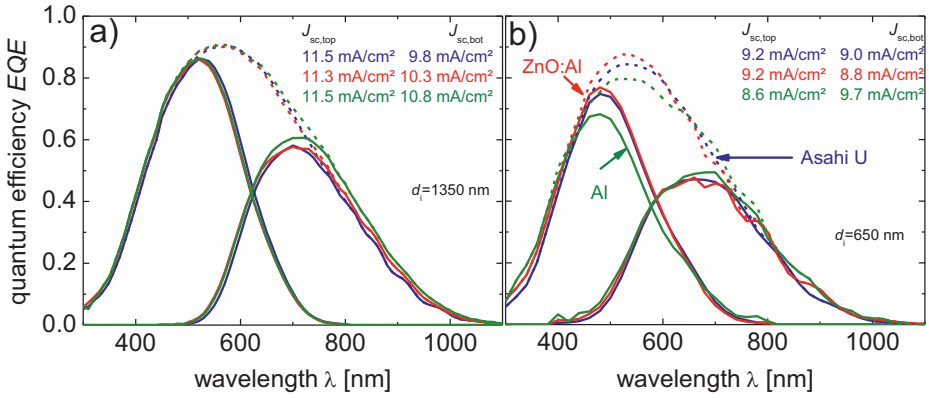

Figure 5.5 Quantum efficiency of a) standard thick and b) thin tandem cell on Asahi U, ZnO:Al and Al substrates. Top and bottom cell quantum efficiencies are given by the straight lines; the dashed lines refer to the summation.

Influence of substrate morphology and i-layer thickness on open-circuit voltage In Table 5.4, the photovoltaic parameters of the respective best performing pads are exemplarily listed. A significantly lower open-circuit voltage was observed for both tandem cells on the Al substrate, which supports the idea of high crystallinity in the µc-Si:H bottom i-layer on Al. Only 1300 mV and 1325 mV were reached for the thick and thin device, respectively. Values as high as 1380 mV were achieved on ZnO:Al for the thick tandem cell and 1390 mV when using thinner i-layers. With a gain in open-circuit voltage of 50 mV the thin tandem cell deposited on Asahi U benefitted most from the thickness reduction. An increase in V_{oc} for reduced device thicknesses was already discussed for the p-i-n cells in subsection 3.3.2, and is attributed to a reduced bulk recombination in the thinner applied absorber layers.

Table 5.4 Photovoltaic parameters measured by a solar simulator, top and bottom short-circuit current densities, derived from EQE measurements, of n-i-p- tandem cells on Ag/ZnO:Ga covered Asahi U, ZnO:Al and Al substrates for standard thick and thin i-layers.

Top/bottom i-layer thickness	**Substrate**	V_{oc} **[mV]**	**η [%]**	***FF*** **[%]**	J_{sc} **[mA/cm²]**
350/1000 nm	Asahi U	1340	9.8	77.0	9.5
	ZnO:Al	1380	10.6	76.7	10.4
	Al	1300	10.4	75.3	10.6
150/500 nm	Asahi U	1390	8.8	68.6	9.2
	ZnO:Al	1390	8.7	69.4	9.9
	Al	1325	6.8	53.0	8.6

Influence of substrate morphology and i-layer thickness on fill factor High fill factors between 75.3% and 77.0% are found for the thick tandem cells. However, different from what would be expected based on the results for the thin tandem cells in p-i-n configuration, *FF* drops about 8% absolute after the i-layer thicknesses were reduced. This drop is partially explained by the matching: The thick tandem cells are bottom cell limited leading to a high *FF*. The thin tandem cells on ZnO:Al and Asahi U are closer to matching, which leads according to subsection 3.3.3 to a decrease in fill factor. However, the very low value of only 53.0% on Al might be caused by shunts. High-energetic particles impinge on the very thin silicon layers during the sputtering of ITO and silver may penetrate down to the back contact.

Influence of substrate morphology and i-layer thickness on efficiency The highest efficiency of 10.6% is obtained on the ZnO:Al substrate with an i-layer thickness of 1350 nm. The efficiency decreased by ~ 19% when the i-layer thickness decreased by

50%. A value of 12% was found for p-i-n solar cells when the total thickness was reduced from 2300 nm to 1050 nm. A significantly higher efficiency decrease of 35% was observed for the tandem cells on Al, which is attributed to a low *FF* and V_{oc} of the thin tandem cell.

5.3.3 Summary

High short-circuit current densities on Al were observed for a thin and thick tandem cell. According to the optical measurements, this can be attributed to good light trapping in the infrared region, or to a higher crystallinity of the µc-Si:H bottom cell, which would also explain the significant lower open-circuit voltages. For the thin tandem cell, the open-circuit voltages increased compared to the thick devices. However, only 1325 mV were reached on Al compared to 1390 mV and 1380 mV on ZnO:Al and Asahi U substrates.

The decrease in fill factor for the thinner cells, which is not in agreement with the trend observed for the p-i-n tandem cells, is supposed to stem from shunts caused by the high energy of impinging particles during the sputtering of the ITO on top of the silicon layers. Accompanied with a low fill factor of 53% the low V_{oc} led to a significantly lower efficiency of only 6.8% for the thin tandem cell on Al compared to efficiencies of 8.8% and 8.7 % on Asahi U and ZnO:Al, respectively.

5.4 Matching behaviour for different substrates

Although having the same i-layer thicknesses different top and bottom cell short-circuit current densities are observed for tandem cells on the three different substrates, as it was shown in Table 5.4. To investigate the matching conditions depending on the substrate and total i-layer thickness in more details additional tandem cells with more top and bottom cell thickness combinations were investigated on Ag/ZnO:Ga covered Al, ZnO:Al and Asahi U substrates. The total i-layer thicknesses were in a range from 650 nm up to 1350 nm.

Experiment By changing the deposition time, different top and bottom cell thicknesses were realized. The layer thicknesses were derived from the deposition time and rate. *EQE* measurements were used to determine the top and bottom short-circuit current densities. In general, short-circuit current density ratios slightly above unity are favoured (slightly bottom cell limited) to reach matching (short-circuit current density ratio ≈ 1) after degradation. Values farther above or below unity indicate bottom or top limitation, respectively.

Matching for thin tandem cells In Figure 5.6 the thickness and short-circuit current density ratios of different top and bottom cell combinations deposited on the three substrate types are shown. With increasing d_{top}/d_{bot} ratio an increasing trend for the ratio of $J_{sc,top}/J_{sc,bot}$ is observed. That shows that a shift from top cell limitation to bottom cell limitation occurs when the ratio top to bottom cell thickness increases, either by decreasing the bottom cell thickness or increasing the top cell thickness. The matching condition is roughly fulfilled for cells with a thickness ratio of about ~ 0.3 in case of ZnO:Al and Asahi U substrates. At this thickness ratio the cell on Al is top cell limited, which indicates that thinner µc-Si:H bottom cells can be used to match with a certain a-Si:H top cell short-circuit current density.

Influence of back reflection However, for the thick tandem cells on Asahi U and ZnO:Al the $J_{sc,top}/J_{sc,bot}$ ratio decreases for an increased d_{top}/d_{bot} ratio of 0.35. At this thickness ratio, tandem cells on Al are slightly top cell limited. The matching condition seems to be influenced by total thickness. It is assumed that the top cells on ZnO:Al and Asahi U benefit from back reflected photons as long as the bottom i-layer is thin enough to transmit these photons. This is not fulfilled anymore when the bottom cell i-layer thickness exceeds a certain value. Back reflection is suppressed and a thicker top i-layer is necessary to match with the bottom cell short-circuit current density and $J_{sc,top}/J_{sc,bot}$ decreases. For tandem cells on Al, back reflection seems to play a minor role, which is attributed to a high light trapping or a higher crystallinity. Therefore, thinner bottom cells are needed to match with a certain top cell short-circuit current density compared to cells on Asahi U and ZnO:Al substrates.

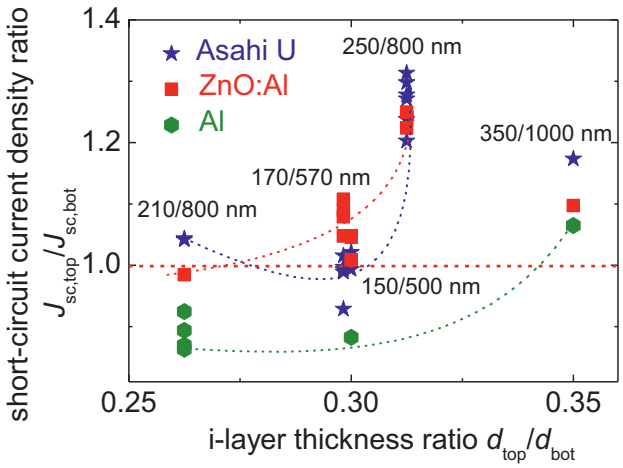

Figure 5.6 Short-circuit current density ratios depending on the thickness ratios of top and bottom i-layer for Al, Asahi U and ZnO:Al substrates

5.5 Investigation on µc-Si:H bottom i-layer

The previous results showed that the open-circuit voltages on the aluminum substrates are significantly lower than on Asahi U and texture-etched ZnO:Al, coated with 200 nm Ag/100 nm ZnO:Ga. It has been reported that rougher surfaces, on the one hand, enhance light trapping and current densities. On the other hand, a decrease in open-circuit voltage and fill factor are observed [115; 116; 117].

By means of Raman measurements, the material properties of the microcrystalline bottom i-layers were evaluated in order to explain the low observed open-circuit voltages and higher short-circuit current densities.

5.5.1 Effect of surface morphology on open-circuit voltage

Crystal growth depending on surface morphology The growth direction of crystals is perpendicular to the local surface such as the crater walls in case of ZnO:Al substrates or the faces of the pyramids in case of Asahi U. For a texture with very steep angles θ

between the substrate surface normal and the growth direction, the growing crystals soon collide and the columnar growth is limited. This occurs, e.g., on Asahi U with $\theta \sim 37°$ leading to a high density of grain boundaries. For ZnO:Al with an angle $\theta \approx 20°$ the slope of the local surfaces it much smaller and a collision of the grains occurs less frequent. Consequently, less grain boundaries are formed. Grain boundaries act as recombination sites and therefore are responsible for a reduction in open-circuit voltage and fill factor. Nasuno et al. suggested that with increasing tan θ the open-circuit voltage and fill factor decrease [117]. It was shown in Table 5.2 that the Asahi U morphology is smoothened due to the ZnO:Ga deposition. This is especially found when 100 nm ZnO:Ga were applied which may lead to less grain boundaries and improved open-circuit voltage and fill factor compared to uncovered Asahi U.

For the U-shape morphology of Al substrates, an angle θ cannot be defined. However, the texture exhibits a very steep slope at the dimple edge, which decreases towards the dimple bottom. Python et al. showed that U-shaped surface structures help to prevent the formation of cracks in the µc-Si:H layers. It is not clear which structure feature, the steep slope or the wide U-shape, has the greater influence on the crystal growth on Al. Additionally, the anodization process at high voltages that is used for structuring the Al surface is subject of fluctuations and the reproducibility needs to be improved. Accordingly, the observed low open-circuit voltages may be a result of non-optimized substrate morphologies. In any case, Sai et al. had shown that high open-circuit voltages are possible on Al: a 0.5 µm thick single junction solar cell achieved 522 mV accompanied with a short-circuit current density of 20.6 mA/cm² [108].

Thickness dependence of V_{oc} In Figure 5.7, the open-circuit voltages of several tandem cells with different thicknesses are depicted. In agreement with the thin p-i-n tandem cells the open-circuit voltage increases when the i-layer thickness is reduced. However, the increasing trend for Al samples is not significant and the highest V_{oc} of 1340 mV was found at a total i-layer thickness of $d_i = 1000$ nm. On Asahi U and ZnO:Al high V_{oc} values as high as 1430 mV and 1420 mV, respectively, were reached with an i-layer thickness of 740 nm. The thin tandem cells on Asahi U seem to benefit from the smoothening due to the thicker ZnO:Ga layer since the open-circuit voltages

are comparable to those on ZnO:Al which is not expected according to Nasuno et al. [117].

The reason for the V_{oc} limitation on Al might partially be explained by the surface morphology and the formed grain boundaries. As it can be seen in Nasuno et al. [118], the deteriorating influence of the grain boundaries occurs mostly in the initial growth region. For thicker bottom cells, a more columnar growth develops after a certain layer thickness with less grain boundaries, and the influence of the grain boundaries in the initial growth region on V_{oc} becomes less pronounced [118]. This could explain the increase in open-circuit voltage for the total i-layer thickness increase from d_i = 650 nm to 1000 nm, also for the Asahi U and ZnO:Al. A further thickness increase does not lead to an improvement in the columnar structure but higher recombination volume and V_{oc} decreases.

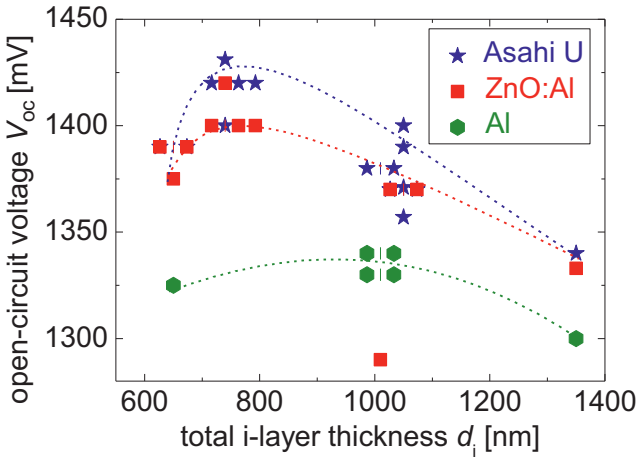

Figure 5.7 Open-circuit voltages as function of total i-layer thickness of n-i-p tandem cells deposited on Ag/ZnO:Ga covered Asahi U, ZnO:Al and Al

5.5.2 Estimation of Raman crystallinity of bottom i-layer

Raman experiment description It is widely known that the open-circuit voltage depends on the crystallinity of µc-Si:H [32; 119]. Hence, Raman measurements were

carried out on the tandem cells in order to estimate the crystallinity of the bottom cell. The measurement was performed through the ~ 150 nm thick amorphous top cell with its µc-Si:H p-doped layer which has to be taken into consideration. Actual values are not accessible. Nevertheless, since the conditions are the same for all measurements and the main focus had laid on the relative comparison between the µc-Si:H layers on Ag/ZnO:Ga covered ZnO:Al, Asahi U and Al the experiment is reliable for this purpose and gives an idea about the crystalline volume fraction in the bottom i-layer.

Before the measurements, the Raman setup (at AIST) was calibrated with a crystalline Si-wafer exhibiting a very narrow peak at 520 cm^{-1}. The wavelength of the probing laser amounted to 633 nm. An amorphous reference spectrum was used to fit the amorphous phase in the taken spectra. The ratio $I_c/(I_c+I_a)$ with I_c and I_a as the integrated intensities of the crystalline and amorphous components, respectively, is used to estimate the crystalline volume fraction X_c^{Raman}, which is proportional to the peak intensity ratio $I_c/(I_c+I_a)$ determined from the spectra of the µc-Si:H i-layer in the tandem cells.

For the data evaluation, it is assumed that the absorption of the 633 nm laser light was similar in the material above the bottom cells on the different substrates and influenced the spectra in the same way.

Crystallinity of µc-Si:H bottom cells on different substrates Raman spectra of the tandem cells deposited on ZnO:Al, Asahi U and Al are depicted in Figure 5.8. In the region between 450 – 500 cm^{-1} where the amorphous contribution appears the measured spectrum for the tandem cells deposited on Al runs significantly below the measuring curves of the ZnO:Al and Asahi U samples indicating less amorphous phase. Accordingly, the derived ratios $I_c/(I_c+I_a) \cdot 100\%$ were ~ 56% on Al, ~ 48% on ZnO:Al and ~ 45% on Asahi U substrates.

The different substrate morphologies influence the crystal growth during the deposition of the µc-Si:H bottom cell which would explain varying the crystallinity. In addition, the influence of the different thermal properties needs to be considered. The heat capacity of aluminum amounts to 897 J/(kg K), which is slightly higher than the thermal capacity of Corning Glass (840 J/(kg K) [120]. The heating due to the plasma

might influence the surface temperature of Al substrates more than the glass-based substrates. Since only the heater temperature can be controlled, the actual substrate temperature on Al plates might be a slightly higher than on the other two substrates, supporting the microcrystalline growth.

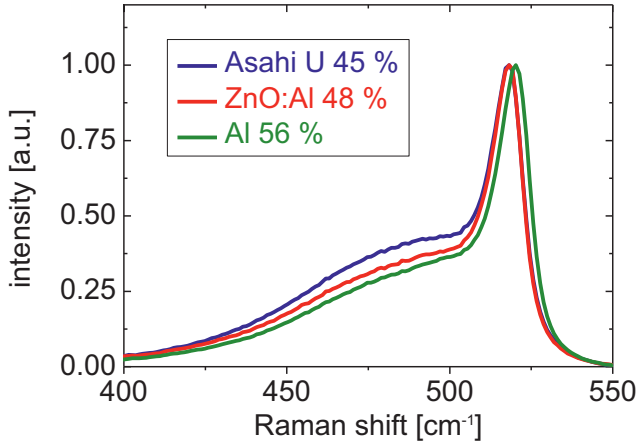

Figure 5.8 Raman measurements on tandem cells on different substrates.

The higher crystalline fraction of the bottom i-layer on Al substrates can explain the lower open-circuit voltage compared to the samples on ZnO:Al and Asahi U deposited under the same conditions. Note that the open-circuit voltage of the top cells is not taken into consideration. However, the substrate influence on $V_{oc,top}$ is assumed to be negligible.

5.5.3 Peak shift in Raman spectra

Origin of peak shift Another noteworthy result derived from the Raman spectra is the different position of the crystalline silicon peak shown in Figure 5.8. A significant shift of about 2 cm^{-1} to higher wave numbers appears for the curve referring to the Al sample in respect to the two curves referring to the Asahi U and ZnO:Al samples. Figure 5.9 shows the Raman spectra from Figure 5.8 at a higher resolution to emphasize the peak shift.

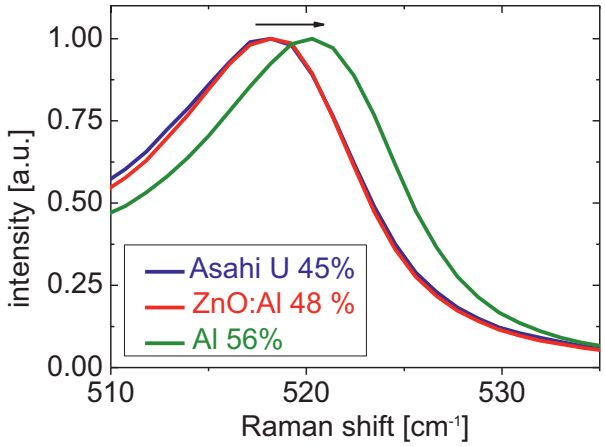

Figure 5.9 Raman peak position of tandem cells on coated ZnO:Al, Asahi U and Al

A shifted peak position is related to small crystal size, lattice anharmonicity, local heating (caused by the laser) or to stress in the layer [121]. These effects may coexist making an interpretation of the Raman spectra is not trivial.

The wave number upshift, caused by compressive stress, can be reduced, or overcompensated by a downshift due to finite crystal sizes or local heating. The crystalline phonon referring to the peak at 520 cm^{-1} remains a well-behaved lattice phonon down to the lowest size limit of ~ 3 nm for which silicon can exist in a cubic lattice. Below this crystal size, a transition to amorphous phase occurs [122]. With decreasing crystal size, the crystalline phonon peak shifts to lower wave numbers down to ~ 512 cm^{-1} for a crystal size of ~ 3 nm. This shift is attributed to a localization of phonons of quasi-isolated crystallites [123]. High compressive stress in the range of 3 GPa can eliminate this quasi-isolation and compensates the peak shift [124].

Local heating effects can be excluded to have a considerable influence on the peak shift since all samples were measured in the same manner and were exposed to the laser the same short data acquisition time. Additionally, a shift caused by local heating would have influenced the measurement on Al substrate the most due to the higher heat capacity and higher thermal conductivity. Since an upshift is observed heating effects, if

at all present, are negligible. A peak shift contribution due to small crystal sizes is not likely, too. Standard μc-Si:H was used in the regarded bottom cells which is supposed to have crystal sizes of about ~ 20 nm and would not cause any downshift. Therefore, the peak shift is attributed to stress in the μc-Si:H layer.

The in-plane stress is given by $\sigma(\text{MPa}) = -250\Delta\omega\ (\text{cm}^{-1})$ with $\Delta\omega = \omega_s - \omega_0$ and ω_0 as the optical phonon wave number of the stress free single crystal and ω_s as the measured value of the stressed layer. Negative or positive values refer to compressive and tensile stress, respectively [125]. In the here regarded case the compressive stress amounts to 500 MPa if no crystal size and local heating effects are considered.

The stress in the layer is supposed to stem from the higher thermal expansion coefficient of aluminum. With $2.4 \times 10^{-5}\ \text{K}^{-1}$ at 20°C [126] it is considerable higher than the thermal expansion coefficient of Corning Glass ($0.355 \times 10^{-5}\ \text{K}^{-1}$) and silicon ($0.3 \times 10^{-5}\ \text{K}^{-1}$). The microcrystalline silicon is deposited at 200°C on the heated and, therefore expanded, Al substrate. After cooling, the Al substrate contracts much more than the deposited silicon layer on top, which results in a residual compressive stress in the μc-Si:H. The effect is negligible for silicon layers on Asahi U and ZnO:Al substrates because the expansion coefficients of silicon and glass are very similar.

Influence of deposition temperature on peak shift The peak shift in Raman spectra taken on tandem cells on Al was attributed to residual compressive stress in Si resulting from the different thermal expansion coefficients. Hence, the peak shift should decrease when the deposition temperature is reduced. To confirm this assumption single junction cells with a μc-Si:H i-layer thickness of 500 nm were deposited at 100°C, 130°C and 160°C on 200 nm Ag/100 nm ZnO:Ga covered Corning Glass and flat Al sheets. The use of non-structured substrates hinders the initial microcrystalline growth and results in a reduced total crystalline fraction, but the peak shift dependence on the deposition temperature for Al and glass-based substrates is accessible.

Figure 5.10 displays the Raman measurements on the three deposited layers on Al measured through the μc-Si:H p-doped layer. The two arrows indicate a) the increasing crystallinity and b) the peak shift to higher wave numbers for higher deposition

temperatures. Whereas the crystallinity of the µc-Si:H layers on glass were similar to those on the Al plates a much smaller peak shift was noticed (not shown).

Iqbal et al. found a red shift (downshift) of the crystalline peak when depositing at decreased temperatures, which he related to a reduction in crystal size [123]. If a reduced crystal size is assumed in the discussed case here, the upshift due to compressive stress for µc-Si:H on Al plates is even more pronounced.

According to these additional results, the residual compressive stress in the microcrystalline layer most likely stems from the higher thermal expansion of Al compared to Si or glass. Stress is accompanied with a higher defect density and a lower hole mobility which enhance the bulk recombination and the lower open-circuit voltage observed on Al substrates can be partially explained [127].

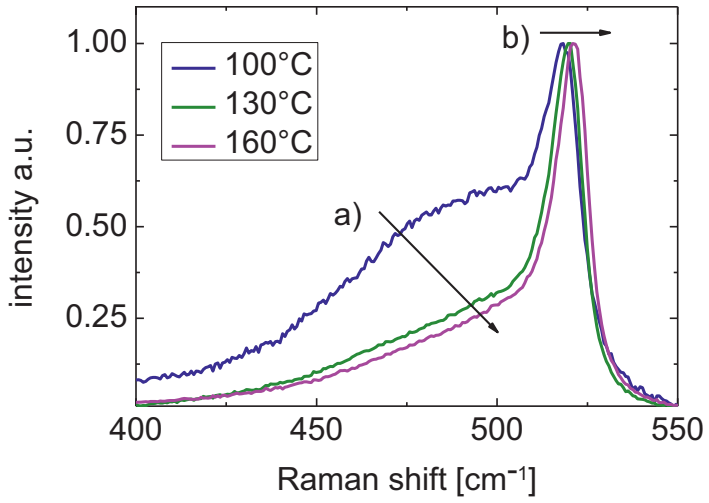

Figure 5.10 Raman spectra of µc-Si:H on flat Al sheets at different deposition temperatures. The arrows indicate a) the increasing crystalline fraction and b) the peak shift to higher wave numbers.

5.5.4 Summary

From Raman spectra measured on tandem cells through the amorphous top cells a higher crystallinity was determined for the µc-Si:H bottom i-layer on Al compared to Asahi U and ZnO:Al substrates. Besides the different surface morphologies the slightly higher heat capacity of Al compared to glass is assumed to support the crystal growth on Al. A significant upshift of the crystalline phonon peak in the Raman spectra is attributed to residual compressive stress in the microcrystalline layers deposited on Al, which was explained by a higher thermal expansion of Al compared to Corning Glass and silicon. The higher crystallinity and occurring stress of microcrystalline layers on Al substrates can explain the observed low open-circuit voltages.

5.6 Bottom cells deposited at higher silane concentration

The low open-circuit voltage for tandem cells on Al was attributed to a high crystallinity of the tandem cell and residual compressive stress in the µc-Si:H layer. Hence, to increase V_{oc} the crystallinity or the stress needs to be reduced. The latter can be achieved, e.g., by reducing the deposition temperature which would deteriorate the material properties significantly. The crystallinity can be controlled by adjusting the silane concentration during the deposition process.

In the following experiments tandem cells were deposited on Ag/ZnO:Ga covered ZnO:Al and Asahi U, for which various silane concentrations were applied for the bottom i-layer deposition in order to reduce the crystallinity in the bottom cell and increase the open-circuit voltage. Raman measurements were carried out under the same conditions as previously reported. The obtained values are related to the measured open-circuit voltages and short-circuit current densities.

Deposition details for *SC*-variation for µc-Si:H bottom cells Thin tandem cells with a top and bottom i-layer thickness of 150 nm and 500 nm, respectively, were deposited under standard conditions; only the silane concentration during the bottom i-layer deposition was varied. As substrate Ag/ZnO:Ga covered Asahi U, texture-etched

ZnO:Al and self-orderly textured Al sheets were used. The silane concentration *SC* was increased from 2.68%, which is the standard value, to 2.86% and 2.99% by changing the hydrogen and the silane gas flow. The total gas flow increase was negligible.

5.6.1 Influence of silane concentration on crystallinity

All microcrystalline layers were examined by Raman measurements through the amorphous top cell. Hence, the determined value can only give an idea of the crystalline volume fraction of the µc-Si:H bottom cell. Nevertheless, due to the same measuring conditions for all tandem cells the values are comparable to the measurements in Figure 5.8 and to each other in this silane concentration series. The determined crystallinity of the tandem cells deposited at different silane concentrations on the three substrate types are summarized in Table 5.5.

Table 5.5 Ratio of integrated peak intensities $I_c/(I_c+I_a)$ of µc-Si:H layers in thin tandem cells depending on silane concentration and substrate type

Substrate Ag/ZnO:Ga covered	**$I_c/(I_c+I_a)$ @ *SC* = 2.68%**	***SC* = 2.86%**	***SC* = 2.99%**
Al	56	47	30
Asahi U	45	43	25
ZnO:Al	49	40	36

The crystallinity of the tandem cells on all three substrates decreases continuously when using higher *SC.* According to the Raman spectra the biggest structure change is observed for tandem cells on Al for which a drop in $I_c/(I_c+I_a)$ from 56% to 30% was observed for a silane concentration increase from 2.68% to 2.99%. For the tandem cells on ZnO:Al a slight decrease in crystallinity was observed, which suggests a certain stability against gas mixture fluctuations caused by process drifts. The structure change in µc-Si:H on Asahi U for a silane concentration of 2.86% is negligible. For a further increase to 2.99% $I_c/(I_c+I_a)$ drops considerably to the lowest determined value of 25%.

By applying a silane concentration of 2.86% the crystallinity on Al reaches a value similar to the crystallinity values for standard material (SC = 2.68%) on ZnO:Al and Asahi U. Thus, similar high open-circuit voltages were expected for the tandem cell.

5.6.2 Tandem cell performance

Open-circuit voltage V_{oc} Figure 5.11 a) and b) displays the open-circuit voltage as a function of the applied silane concentration for the bottom cell deposition and the determined crystallinity on different substrates. The values of V_{oc} of the Asahi U samples increase slightly from 1390 mV to 1410 mV when the silane concentration increases from 2.68% to 2.99%, even though a rather strong change in crystallinity was observed. The increase in open-circuit voltage for the ZnO:Al samples is moderate peaking in a value of 1420 mV and is in accordance to the small change of $I_c/(I_c+I_a)$.

With a silane concentration of 2.86% the Al sample exhibits a crystallinity value similar to the values of the ZnO:Al and Asahi U samples under standard deposition conditions for which V_{oc} values were up to 1380 mV. However, the open-circuit voltage on Al remains as low as for the standard regime, which indicates that the higher crystallinity cannot be the only reason for the low V_{oc} under standard conditions. By further increasing SC to 2.99% a high open-circuit voltage of 1405 mV was achieved.

Short-circuit current density J_{sc} Microcrystalline i-layers, exhibiting a decreased crystallinity, generally generate lower J_{sc}, which can be observed for the investigated tandem cells in Figure 5.11 c) and d). For all three substrate types J_{sc} decreases for higher silane concentrations or lower crystallinity.

The J_{sc} of the Asahi U sample deposited with SC = 2.86% is higher than for the lower standard concentration, which is attributed to a better matching. For a further SC increase, J_{sc} drops as expected.

A small change in crystallinity and V_{oc} is observed for the sample on ZnO:Al. Also the short-circuit current density shows only a slight decrease from which it is derived that the cell performance is fairly stable against silane concentration fluctuations.

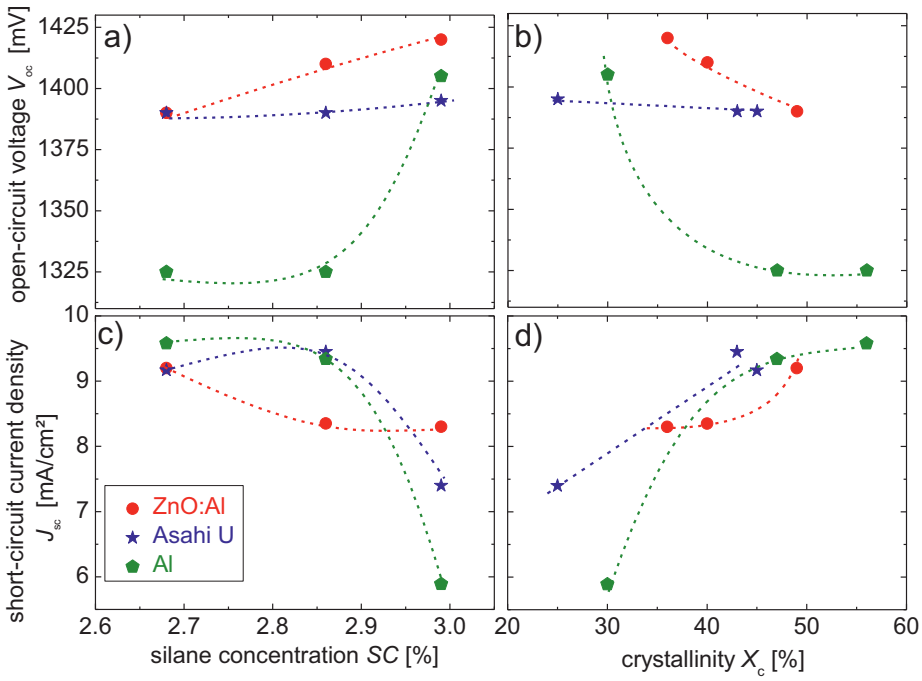

Figure 5.11 Open-circuit voltage and short-circuit current density dependent on the applied silane concentration and the crystallinity of tandem cells deposited on Al, ZnO:Al and Asahi U. The dashed lines are guides to the eye.

Unfortunately, the high V_{oc}, which is achieved on Al with a silane concentration of 2.99% during the µc-Si:H-i-layer deposition, came along with a tremendous decrease of J_{sc}. This low value of 5.9 mA/cm² is not balanced by the high open-circuit voltage and, consequently, leads to a low efficiency of 4.6%.

Having even a lower $I_c/(I_c+I_a)$ as the tandem cell on Al, the tandem cell on Asahi U exhibits a much higher J_{sc} of 7.3 mA/cm² accompanied with an open-circuit voltage of 1390 mV. The efficiency amounts to 6.9%. With similar crystallinity between 42 – 50% the tandem cells on three different substrates achieve similar short-circuit current densities. Accordingly, the assumed high light trapping ability of Al substrates is questionable. The thicknesses of top and bottom i-layer in this experiment were not adjusted, which resulted in differently matched tandem cells. By adjusting the top and

bottom cell thicknesses the lower short-circuit current densities are supposed to improve slightly.

5.6.3 Summary

By increasing the silane concentration from 2.68% to 2.99% during the deposition of the µc-Si:H bottom i-layer a reduction in crystallinity was observed for layers on all three substrate types. The small structure change observed for material on ZnO:Al did not affect the performance of the tandem cell considerably, which can be interpreted as a fairly high stability against deviations or changes in the process gas mixture.

On the textured aluminum plates, the increased *SC* caused a rather big crystallinity decrease resulting in an increase in V_{oc} up to 1405 mV. However, this increase came along with a remarkable drop in short-circuit current density from 9.6 mA/cm² to 5.9 mA/cm² and a low efficiency of 4.6%. With an even lower crystallinity the tandem cells on Asahi U reached a short-circuit current density of 7.4%. Since similar high short-current densities are achieved on Asahi U and ZnO:Al substrates when similar crystallinity as on Al substrates are observed the better light trapping which was assumed for Al substrates is questionable and needs further investigation

5.7 Conclusion

In this chapter, the application of self-orderly textured aluminum sheets as substrates for n-i-p tandem cells was evaluated. Special focus lay on very thin tandem cells with a total i-layer thickness below 700 nm.

As reference to the aluminum plates, Asahi U and texture-etched ZnO:Al were used as substrates, which were all covered with Ag/ZnO:Ga by a DC-sputter process. High diffuse reflectivity for the Al substrate indicated good light trapping, especially in the infrared region.

Tandem cells in the n-i-p configuration with total i-layer thicknesses of 1350 nm (standard thick cell) and 650 nm (thin cell) were deposited on the three investigated substrate types and compared regarding their photovoltaic parameters and quantum efficiencies. For both thicknesses, the cells on Al substrates showed the highest bottom

cell short-circuit current densities. However, the open-circuit voltages were significantly lower than for tandem cells on Asahi U and ZnO:Al substrates and led to a fairly low efficiency for the thin device.

On all three substrates the $J_{sc,top}/J_{sc,bot}$ increases with increasing d_{top}/d_{bot}. The matching condition on ZnO:Al and Asahi U is fulfilled at a lower thickness ratio than on Al. It was assumed that top cells benefit from back reflection whereas on the Al substrate the light trapping in the bottom cell seems to prevent back reflection. According to this study, much thinner bottom i-layers can be used on Al compared to Asahi U and ZnO:Al to match with a top cell of a given thickness. This makes it possible to decrease deposition time and costs.

Lower open-circuit voltages on Al samples compared to Asahi U and ZnO:Al were partially attributed to a higher crystallinity. Since the heat capacity of Al is slightly higher than for the glass substrates, the effect of plasma heating might be more pronounced. A higher effective temperature may occur that promote the crystalline growth.

Additional, a Raman peak shift to higher wave numbers was found for tandem cells on Al indicating compressive stress in the µc-Si:H layers. Due to a stronger contraction of Al compared to silicon residual compressive stress remains in the µc-Si:H layer. Further experiments showed that the peak upshift increases with deposition temperature and is significantly stronger on Al than on glass. Stress in the µc-Si:H layer enhances the defect density that may lead to lower open-circuit voltages. Therefore, the higher crystallinity and the compressive stress in the silicon layers were assumed to cause the low observed open-circuit voltages. In order to increase V_{oc} thin tandem cells were deposited with bottom i-layers prepared with higher *SC*. The crystallinity on Al decreased from 56% to 30%, which resulted, on the one hand, in an increase in V_{oc} from 1325 mV to 1405 mV. On the other hand, unfortunately, J_{sc} dropped tremendously, resulting in low efficiencies.

The performance of thin tandem cells on self-orderly textured aluminum plates cannot compete with the tandem cells deposited on Asahi U or ZnO:Al substrates.

However, by adjusting the deposition parameters sufficiently high open-circuit voltages accompanied with high short-circuit current densities might be possible.

Chapter 6

Structure analysis on μc-Si:H by X-ray diffraction and Raman spectroscopy

In this chapter the crystallinity of μc-Si:H layers deposited with various silane concentrations is investigated by Raman spectroscopy and X-ray diffraction (XRD), and is related to the performance of solar cells deposited together with the μc-Si:H layers. After an initial characterization of the prepared i-layers by means of Raman spectroscopy, the derived crystallinity values are compared to XRD measurements taken with two scattering geometries. The appearance of stacking faults and twins is investigated by evaluating the hexagonal contribution in the diffractograms of μc-Si:H. The existence and degree of a preferential orientation (so-called "texture") of cubic silicon crystals along the [110] axis is investigated and discussed. Incident angle dependent XRD measurements and Raman measurements taken along an etch crater were carried out to study the phase transition in three μc-Si:H layers deposited with constant and non-constant silane concentration.

6.1 Introduction

Microcrystalline silicon exhibits a complex appearance with different microstructural forms that strongly depend on the precise deposition conditions [35; 128]. Only material with certain structural properties is suitable for photovoltaic application. The best solar cell performance is observed for µc-Si:H material close to the transition to amorphous silicon [34; 119; 128]. A detailed characterization of the µc-Si:H material used in solar cells is therefore necessary.

Raman spectroscopy and XRD are the most commonly used methods to investigate structural properties of microcrystalline silicon. Due to the fast data acquisition time semi-quantitative Raman spectra are usually used to approach the crystalline volume fraction of µc-Si:H material. A detailed study on µc-Si:H and a-Si:H by means of Raman spectroscopy including e.g., grain size and temperature effects was done by Iqbal et al. [123] and Vepřek et al. [124]. X-ray diffraction allows an accurate investigation of crystal size, texture, and crystallinity but is time-consuming.

Generally, the silicon crystals in microcrystalline silicon are randomly oriented. However, several authors report that a preferential crystal orientation along the [110] axis is beneficial regarding an improved charge carrier transport [129; 130]. Vallat-Sauvain found an increase in preferential orientation when approaching the transition region [132].

Besides the most intense diffraction peaks associated with the {111}, {220} and {311} lattice planes of cubic silicon crystals additional peaks on the low angle shoulder of the {111} and {311} peaks were observed. These peaks were attributed to stacking faults and a high density of twin planes [35; 133; 134; 135].

The following chapter focuses on the characterization of µc-Si:H intrinsic layers deposited at IEF5 by Raman spectroscopy and XRD. The occurrence of a preferential orientation or a high stacking fault and twin density is discussed and compared to results published by other research groups. Furthermore, depth resolved crystallinity determinations by XRD and Raman spectroscopy are presented.

6.2 Initial characterization of µc-Si:H prepared with different silane concentrations

For the investigation of microcrystalline silicon deposited at IEF5-Photovoltaik samples with different silane concentrations were deposited. The crystallinity of these layers was initially determined by a reference measurement with Raman spectroscopy to ensure that highly crystalline and amorphous material was achieved for further studies. Two different laser wavelengths were used to probe the layers into different depths in order to gain first information about the homogeneity of the layers. The values were related to open-circuit voltage and fill factor of solar cells, which were deposited together with the investigated material.

6.2.1 Sample fabrication

It was aimed to gain knowledge about the µc-Si:H material as it occurs in solar cells. Since the structure of the underlying material influences the crystal growth tremendously all intrinsic µc-Si:H layers were deposited on top of a microcrystalline p-doped layer on texture-etched ZnO:Al. The standard deposition conditions for µc-Si:H were used, only the silane concentration was varied. A series of µc-Si:H solar cells with an i-layer thickness of ~ 1 µm was deposited with silane concentrations varying from 0.71% to 1.04%. Before the amorphous n-type doped layer was deposited, one substrate per deposition run was locked out and used for Raman and XRD measurements. The photovoltaic parameters of the processed solar cells were related to the determined crystalline volume fractions and, later on, microstructural properties.

6.2.2 Influence of silane concentration on Raman crystallinity

The Raman spectra were measured and evaluated according to the routine described in subsection 2.3.5. The near backscattering setup was used.

Influence of excitation laser wavelength on Raman measurements The penetration depth of the laser with λ_{laser} = 647 nm amounts roughly to ~ 1 µm whereas the higher

absorption for laser light with λ_{laser} = 488 nm in µc-Si:H leads to a penetration depth of ~ 0.1 µm. Consequently, information about the crystallinity of the layers in two different depths is accessible.

Since the µc-Si:H layer thicknesses of all investigated samples was in the range of the penetration depth of the 647 nm laser the light of both lasers is fully absorbed. Hence, measurements with the 488 nm and 647 nm laser should reveal similar crystallinity values. However, the different cross section of amorphous and microcrystalline silicon has to be considered. In case of 488 nm laser light the scatter cross section of µc-Si:H is higher than for amorphous material whereas for laser light with a wavelength of 647 nm both cross sections are the same. Accordingly, the crystallinity values derived from the 488 nm measurements overestimate the crystalline volume fraction slightly [35; 135]. Additionally, the scattered Raman light experiences a slightly different wavelength shift when scattered by amorphous phase than by crystalline phase. However, in general this effect is negligible.

Silane concentration range The investigated microcrystalline silicon layers were deposited with different silane concentrations (*SC*) in the range between 0.71% and 1.04%. The range was chosen according to the determined crystallinity: With 1.04% the transition to amorphous material had already taken place while the crystallinity seemed to saturate at 85% for a silane concentration of ~ 0.71%. For the standard material a silane concentration of 1.02% is used.

Raman crystallinity $X_c^{Raman,\,488}$ depending on *SC* Figure 6.1 shows that the crystallinity (derived from measurements with 488 nm laser) $X_c^{Raman,\,488}$ decreases from 85% to 76% when the silane concentration increases from 0.71% to 1.0%. For higher silane concentrations the crystalline volume fraction decreases with a steep slope until at 1.04% almost no crystalline phase is detectable. According to this result, the standard material with a crystalline volume fraction of $X_c^{Raman,\,488}$ = 65%, deposited at *SC* = 1.02%, is close to the transition to amorphous material and should exhibit the best device-quality regarding solar cell application.

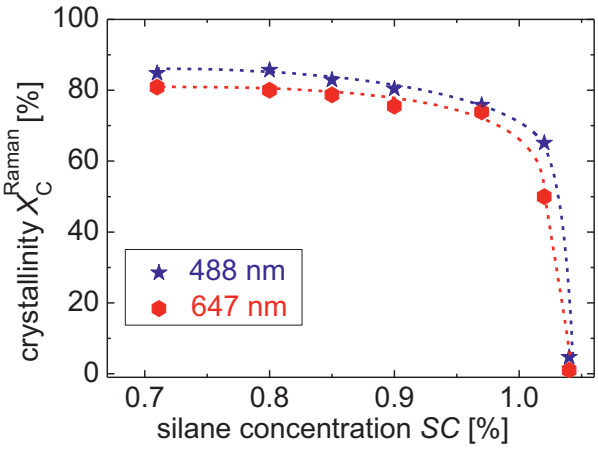

Figure 6.1 Raman crystallinity of µc-Si:H layer stacks deposited at various silane concentrations, determined by using two different laser wavelengths. The dashed lines are guides to the eye.

Raman crystallinity $X_c^{Raman,647}$ depending on *SC* The crystallinity values derived from measurements with the 647 nm laser, probing the layer into ~ 1 µm depth, are between 2 – 6% (absolute) lower compared to values probing with the 488 nm laser. This difference is ascribed to the different scatter cross sections: Taken the slight higher sensitivity for crystalline material of the 488 nm measurement into account a homogeneous crystal growth is observed µc-Si:H layers deposited with low silane concentrations up to ~ 1.0%.

When the silane concentration increases to *SC* = 1.02% a crystallinity difference of 15% (absolute) between the measurements with the 647 nm and 488 nm laser is found which cannot solely be explained by the Raman cross section difference. It is assumed that due to the higher applied silane concentration the crystal growth might be slightly inhibited during the first phase of deposition. With increasing layer thickness, the crystalline structure evolves and the crystallinity increases.

6.2.3 Influence of silane concentration and Raman crystallinity on V_{oc} and *FF*

Silane concentration In Figure 6.2 a) and c) fill factor and open-circuit voltage of the µc:Si:H single junction solar cells are shown as function of the applied silane concentration. Both, *FF* and V_{oc}, increase almost linearly with increasing silane concentration. The standard solar cell deposited at a silane concentration of 1.02% achieved the highest fill factor of $FF = 72.6\%$ and open-circuit voltage of $V_{oc} = 513$ mV.

No solar cell was deposited with $SC = 1.04\%$, but since the material was almost amorphous a further increase in open-circuit voltage and a drop in fill factor are expected.

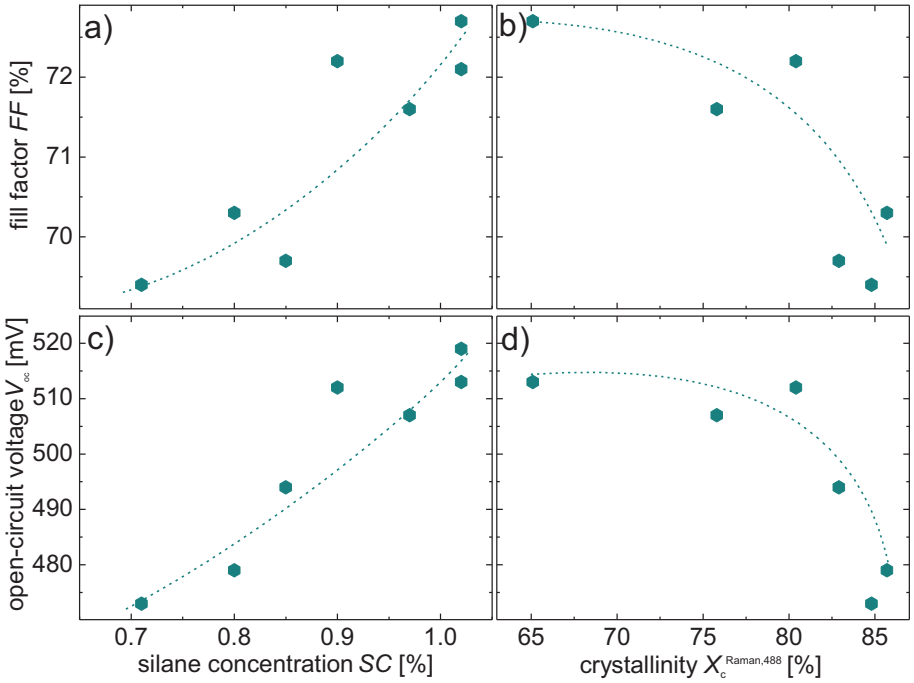

Figure 6.2 Fill factor and open-circuit voltage depending on silane concentration and Raman crystallinity. The dashed lines are guides to the eye.

Raman crystallinity In Figure 6.2 b) and d) fill factor and the open-circuit voltage of the µc-Si:H solar cells are presented as a function of Raman crystallinity $X_c^{\text{Raman, 488}}$ of the related µc-Si:H i-layers. With increasing crystallinity, *FF* and V_{oc} show a decreasing trend. Solar cells with a high i-layer crystallinity up to ~ 80% are able to achieve high V_{oc} above 500 mV accompanied with high *FF* ~ 72%. However, both solar cell parameters decrease abruptly for higher crystallinity values. The solar cell deposited under standard condition, which also showed the best solar cell performance, has an i-layer crystallinity of 65%. According to Figure 6.1, this material was close to the transition to amorphous silicon where the best device-quality material is supposed to be found.

6.2.4 Summary

Microcrystalline silicon layer stacks were deposited together with single junction solar cells at various silane concentrations. Raman measurements showed that with *SC* from 0.71% to 1.04% material with high crystallinity and almost amorphous material is achieved. The standard material at *SC* = 1.02% exhibits a noteworthy crystallinity difference when probing into 0.1 µm and 1 µm depth which indicates an inhibited crystal growth during the initial deposition phase. Above crystalline volume fractions of 80% which refers to a silane concentration of 0.9% V_{oc} and *FF* decrease abruptly. The standard material with $X_c^{\text{Raman}} = 65\%$ reached an open-circuit voltage and fill factor of 513 mV and 72.7%, respectively, which were the highest observed values in this series, leading to the highest solar cell efficiency. This result is in accordance to literature, where the optimal crystalline volume fraction regarding solar cell performance is expected between 60% and 70%.

6.3 Correlation between Raman and XRD crystallinity

In section 6.2 the Raman crystallinity of µc-Si:H i-layers was determined in two different depths. For further studies, the correlation between the crystallinity derived from Raman and XRD measurements was of interest. Therefore, the crystallinity

obtained by Grazing Incidence and Bragg-Brentano XRD is compared to the Raman crystallinity derived from measurements with a 488 nm and 647 nm laser. The different values for the crystalline volume fraction are compared with respect to the silane concentration. Occurring variations are discussed taking the different probing depth of the methods into account.

6.3.1 XRD in Grazing Incidence geometry

Grazing Incidence XRD was measured and evaluated according to the routine described in subsection 2.3.6. An incident angle α was chosen so that the X-ray probed the layer in a way that ensured a sufficient high scatter intensity from the sample without any contribution from the glass substrate.

In Figure 6.3, the crystallinity values derived from the diffractograms are plotted against the Raman crystallinity values that were determined for the layer stacks previously. Additional values from a former sample series are included into the graphics by open symbols.

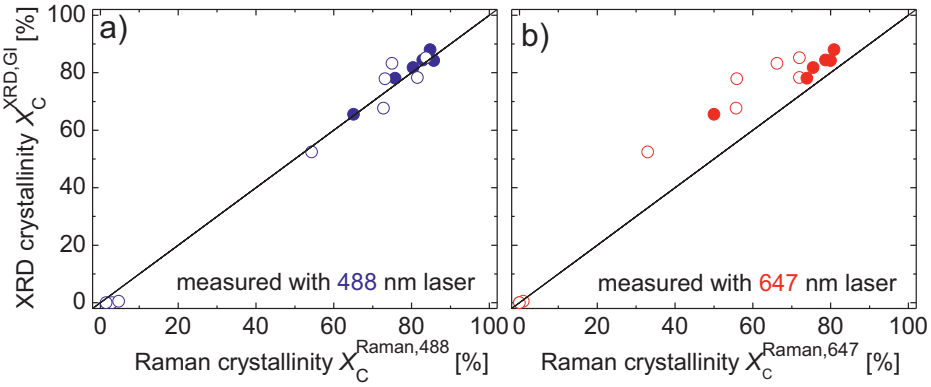

Figure 6.3 Correlation of GI-XRD and Raman crystallinity, determined from measurements with the 488 nm and 647 nm laser. The lines represent equality.

Figure 6.3 a) displays the GI-XRD crystallinity as a function of the crystallinity derived from Raman measurements carried out with the 488 nm laser. The values are

very close to the unity line which shows a very good correlation between GI-XRD and Raman (at 488 nm measured) crystallinity.

Figure 6.3 b) displays the relation between the GI-XRD crystallinity and values derived from Raman measurements with the 647 nm laser. The observed deviation from unity towards lower crystalline volume fractions reflects the difference between the two wavelengths in the Raman experiment. This difference was attributed to a slightly lower crystalline volume fraction at the initial growth region and an occurring overestimation of crystalline phase due to a higher scattering cross section of μc-Si:H for laser light with a wavelength of 488 nm.

For Raman and GI-XRD measurements, the inaccuracies of the crystallinity values depend on the crystallinity of the layer. For highly crystalline samples, the error is estimated to < 5% whereas it increases for more amorphous layers. GI-XRD and Raman crystallinity show a good agreement taken this inaccuracy into account.

XRD in Bragg-Brentano geometry Additional to GI-XRD, measurements in the symmetrical Bragg-Brentano geometry were performed. Incident and refracted angle change in the same manner so that the X-ray penetrates the whole sample. On the one hand, it is possible to gain information about the whole layer. On the other hand, a contribution of the glass substrate and the ZnO:Al layer has to be considered. Measuring routine and data evaluation are described in subsection 2.3.6.

6.3.2 Comparison of methods for the determination of crystallinity

Figure 6.4 depicts the crystalline volume fraction of μc-Si:H layers as a function of the used silane concentration. The good correlation between the crystallinity values of GI-XRD and Raman measurements taken with the 488 nm laser was already pointed out.

The crystallinity derived from Raman measurements at 647 nm was slightly lower compared to values derived from GI-XRD and 488 nm Raman measurements as discussed before. A significant lower crystallinity was found by evaluating the Bragg-Brentano measurements. According to Figure 6.4, the difference to all other data looks

rather systematically. The high scatter contribution of the glass background that superposed with the signal from the crystalline and amorphous silicon obstructed an accurate data evaluation. Part of the glass background might have been assigned by mistake to the amorphous silicon phase and, consequently, led to an underestimation of the crystallinity. The crystalline volume fractions determined by BB-XRD have therefore a higher measurement inaccuracy as values derived from GI-XRD.

For all methods the transition regime between microcrystalline and amorphous material was found at the same silane concentration of $SC > 1.02\%$. When the silane concentration increases only slightly to $SC = 1.04\%$ an abrupt drop from values between 65% and 50% for the 488 nm and 647 nm Raman measurements down to 4% and 0%, respectively, occurs. This shows the high sensitivity of the microcrystalline growth to silane concentration.

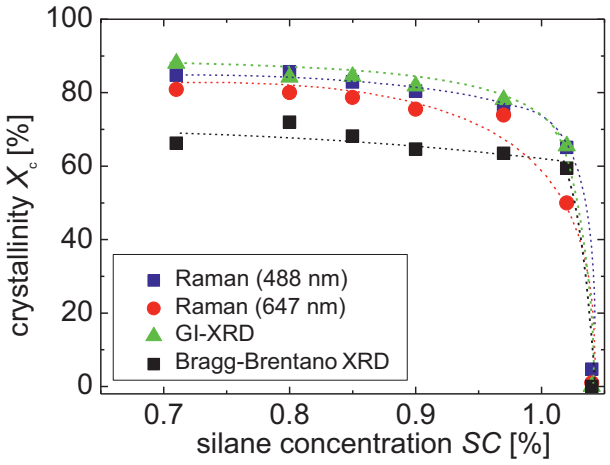

Figure 6.4 Crystalline volume fraction determined by XRD and Raman spectroscopy dependent on silane concentration. The dashed lines are guides to the eye.

6.3.3 Summary

The crystallinity of µc-Si:H layer stacks deposited with different silane concentrations was investigated. A good correlation between GI-XRD values and

Raman crystallinity derived from spectra taken with the 488 nm laser is found. The overestimation of crystalline phase and material inhomogeneities explained the slightly higher crystallinity compared to values derived from the measurement with the 647 nm laser. The Bragg-Brentano XRD crystallinity is even lower which is attributed to the underestimation of the glass substrate contribution and mistakenly assigning it to the amorphous phase. All methods find the transition to amorphous material at the same silane concentration.

6.4 Hexagonal phase in µc-Si:H

Besides reflections that stem from cubic silicon a reflection with varying intensity adjacent to the {111} peak is noticeable in both, Grazing Incidence and Bragg-Brentano diffractograms. Houben et al. and Hendriks et al. attributed this peak to stacking faults and twins in the crystals of µc-Si:H i-layers which appear as hexagonal phase of silicon in XRD scans [133; 134].

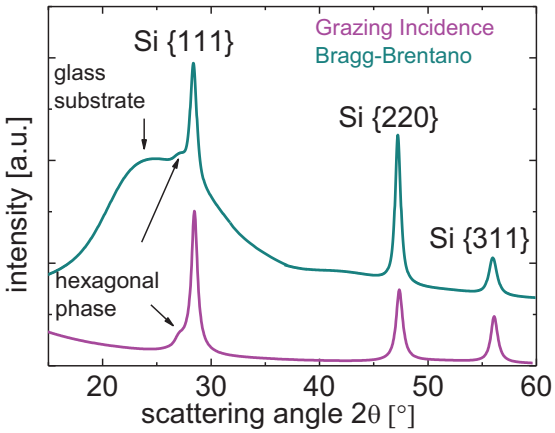

Figure 6.5 Grazing Incidence and Bragg-Brentano diffractograms of a µc-Si:H layer with an additional peak at ~ 27° that is attributed to a hexagonal phase induced by stacking faults and twins.

In Figure 6.5, two diffractograms of a µc-Si:H layer in GI and BB geometry are shown with a clearly visible peak on the low angle shoulder of the {111} reflection. This peak is evaluated by means of Grazing Incidence and Bragg-Brentano XRD measurements to gain information about the existence of stacking faults and twins. The share of hexagonal contribution is related to crystallinity and silane concentration.

6.4.1 Origin of the hexagonal phase

An explanation for the appearance of the peak at ~ 27° is based on the presence of polytypic silicon modifications. Polytypism is characterized by a stacking sequence with a large spacing along the stacking axis. These modifications are closely related to a high density of planar faults in the microcrystalline silicon layers. Silicon crystallizes in the face-centred cubic structure shown in Figure 6.6. The stacking sequence is ABCABC. Stacking faults can occur in a way that the stacking order changes locally to ABAB [136]. Such a stacking sequence is characteristic for the hexagonal close-packed crystal structure (also called "wurtzite") displayed in Figure 6.7. The atoms are still tedrahedrally coordinated.

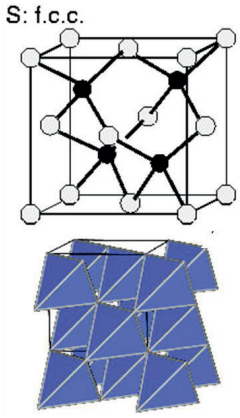

Figure 6.6 The face-centered cubic structure

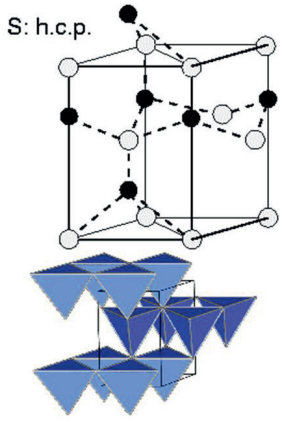

Figure 6.7 The hexagonal close-packed structure

Depending on the periodicity, the polytypic modifications have different lattice spacings in the direction along the growth axis and appear as reflections at different positions. The additional peak at ~ 27° near the $\{111\}_{cub}$ is assumed to stem from the $\{100\}_{hex}$ reflection. A detailed study on the cause of this additional peak in the diffractograms of µc-Si:H is given by Hendriks et al. [134], and is supported by Houben et al. [133] and Luysberg et al. [135].

6.4.2 Hexagonal fraction investigated by XRD

The diffractograms of the µc-Si:H layers deposited with different *SC* were evaluated with special focus on the hexagonal phase. It has to be taken into consideration that the intensities that were determined for the cubic phase for the {111}, {220} and {311} reflections contain a considerable fraction of hexagonal phase, too. Besides the $\{100\}_{hex}$ reflection at ~27° the powder standard of hexagonal silicon shows scatter intensity at angles of 2θ = 28.4°, 47.8° and 56.6°. These reflections correspond to {002}, {110} and {112} reflections of hexagonal silicon and exhibit an intensity ratio in regards to the $\{100\}_{hex}$ reflection of 0.56 : 0.605 : 0.33. Accordingly, the hexagonal phase is given by:

$$I_{hex} = I_{100,hex} + I_{002,hex} + I_{110,hex} + I_{112,hex}. \quad (6.1)$$

By taken the intensity ratios into account, assuming a randomly oriented hexagonal phase, it changes to:

$$I_{hex} = I_{100,hex}\,(1 + 0.56 + 0.605 + 0.33) \quad (6.2)$$

and finally, the hexagonal fraction X_c^{hex} is calculated by:

$$X_c^{hex} = I_{hex}/(I_{111} + I_{220} + I_{311} + I_{100,hex}. \quad (6.3)$$

Figure 6.8 shows the hexagonal fraction X_c^{hex} as function of the Raman crystallinity derived from the measurements with 488 nm. The values derived from Grazing Incidence XRD are considerably lower than the values found by Bragg-Brentano scans. In contrast to GI-XRD, in the Bragg-Brentano geometry only lattice planes parallel to the sample surface contribute to the reflection signal. Therefore, it is assumed that more stacking faults and twins appear on planes parallel to the surface. The hexagonal contribution to the crystalline phase increases with increasing total crystallinity for both XRD geometries. This suggests that more imperfections in the cubic crystal structure of silicon occur when the crystallinity increases.

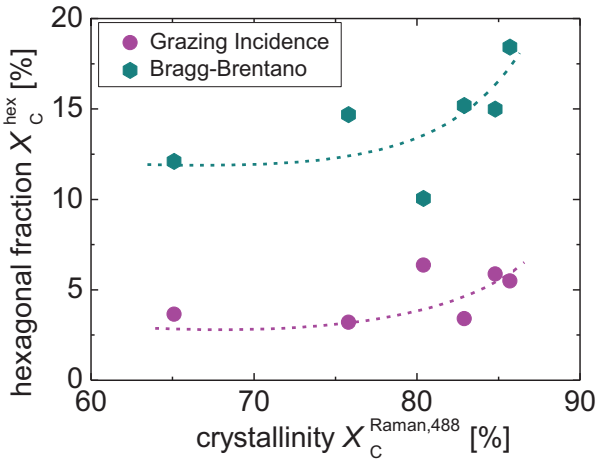

Figure 6.8 Hexagonal fraction as function of Raman crystallinity (with 488 nm)

6.4.3 Summary

The emergence of an additional peak at ~ 27° was attributed to stacking faults and twins in the cubic silicon crystals of. These crystal imperfections induce local structure changes that appear as $\{100\}_{hex}$ peak in the diffractograms.

With increasing crystalline volume fraction $X_c^{Raman,488}$,the share of hexagonal phase on the crystalline phase increases. The stacking faults and twins appear more pronounced at planes parallel to the surface which was derived from the higher

hexagonal fractions determined by Bragg-Brentano compared to GI-XRD measurements.

6.5 Preferential orientation in µc-Si:H

The following part deals with the evaluation of the taken XRD diffractograms in order to appraise if a preferential growth direction occurs in the microcrystalline layers. Asymmetrical Grazing Incidence and symmetrical Bragg-Brentano XRD are considered. The integrated intensity ratio of the {220} reflection to the {111} reflection is compared to the powder standard of cubic silicon.

General aspects Usually, microcrystalline silicon exhibits a random orientation which means that the crystal growth appears in all possible directions with the same probability. Each grain in a polycrystalline formation has a crystallographic orientation different from an adjacent grain [132]. The observed intensity ratios of the cubic reflections referring to these grains are consistent with those of the powder standard of cubic silicon which are {111}:{220}:{311} = 1:0.55:0.30 [137].

Under certain deposition conditions, the random orientation vanishes and the crystal growth occurs along a preferred axis. By choosing adequate deposition conditions, e.g., applying high hydrogen dilution during the initial growth a preferential crystal growth in the [110] direction is achieved, as it was reported by Wang et al. [138]. Toyama et al. reported a (111) preferential orientation of isolated grains in the early growth state of µc-Si:H whereas µc-Si:H films with columnar grains exhibit a (220) preferential orientation. Sugano et al. claimed an increase in the intensity ratio of the {220} to {111} reflection (I_{220}/I_{111}) for lower silane concentration [139]. In contrast, Vallat-Sauvain et al. found a decrease in I_{220}/I_{111} from ~ 3.5 to 0.55 with decreasing silane concentration which refers to a strong (220) texture in µc-Si:H material close to the transition to amorphous silicon and random orientation for highly crystalline material [132]. Besides deposition method and hydrogen dilution, ion damaging of the surface of the growing layer seems to influence the orientation. However, the process that determines the orientation is not fully understood yet [140; 141; 142].

The appearance of a (220) texture is of interest because several research groups claim that such μc-Si:H material leads to higher solar cell efficiencies due to an improved transport of photogenerated charge carriers along the [110] axis [129; 130].

6.5.1 Influence of silane concentration on the integrated intensity ratio I_{220}/I_{111}

To investigate if the deposited layers exhibit a texture or are randomly oriented the integrated intensities of the {111} and {220} peaks appearing in Bragg-Brentano and Grazing Incidence XRD scans were evaluated. The ratio I_{220}/I_{111} was calculated and compared to ratio of the powder standard of cubic silicon.

The ratio I_{220}/I_{111} derived from Bragg-Brentano measurements evaluates crystals with a growth direction normal to the sample surface regarding a preferential orientation. Grazing Incidence XRD measurements look at crystals with growth directions not normal to the sample surface.

Integrated intensity ratio I_{220}/I_{111} by Grazing Incidence XRD In Figure 6.9 a) the ratios I_{220}/I_{111} for both, GI- and BB-XRD measurements, are shown as a function of *SC*. The values determined by Grazing Incidence XRD varied slightly between 0.54 and 0.59 independent on silane concentration. These values are in good agreement with the standard silicon powder for which I_{220}/I_{111} amounts to 0.55. This indicates a random orientation of the Si crystals in the μc-Si:H layers that grow in a direction not parallel to the surface normal.

Integrated intensity ratio I_{220}/I_{111} by Bragg-Brentano XRD For silane concentrations up to *SC* = 1.0% the integrated intensity ratios of {220} to {111} derived from Bragg-Brentano measurements amounts to ~ 0.8 with a highest value of 1.0 at a silane concentration of 0.9%. These values are slightly higher than the values found by GI-XRD and for standard silicon powder. However, the peak height intensity ratios observed by Vallat-Sauvain et al. and Sugano et al. for textured μc-Si:H were much higher and went up to 3.5 and 4, respectively [132; 139]. That shows that, if at all, only a slight preferential orientation along the [110] axis occurs for crystals that grow parallel to the surface normal. For the standard μc-Si:H material deposited at a silane

concentration of 1.02% a I_{220}/I_{111} of 0.5 was found which is even below the value of the standard silicon powder.

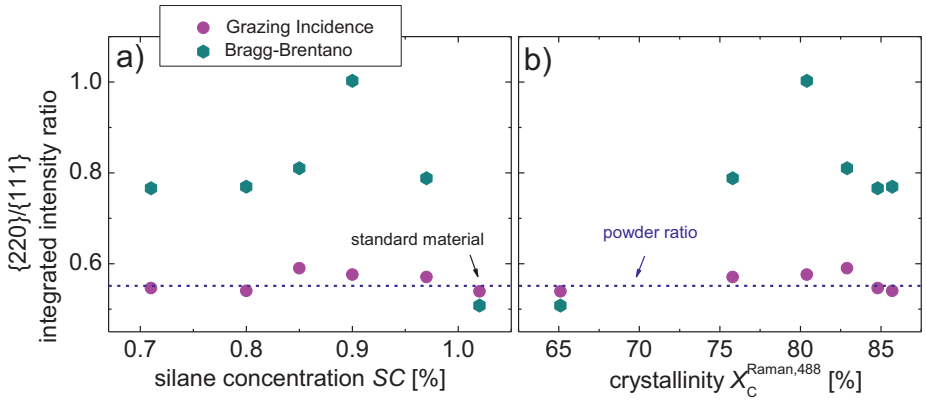

Figure 6.9 Integrated intensity ratio of {220} to {111} as a function of a) silane concentration and b) Raman crystallinity derived from 488 nm measurement. The blue dashed line refers to the {220} to {111} ratio of the powder standard. The blue dashed line indicates the intensity ratio for the powder standard.

6.5.2 Influence of integrated intensity ratio I_{220}/I_{111} on solar cell performance

According to these studies µc-Si:H close to the transition to amorphous material shows no significant (220) texture, neither according to GI- nor BB-XRD measurements, as it was claimed before [132]. For the solar cell in which such material was implemented has the highest efficiency. The high short-circuit current density and fill factor disproved that a preferential orientation along the [110] axis is necessary for device-quality material.

6.5.3 Influence of crystallinity on the integrated intensity ratio I_{220}/I_{111}

In Figure 6.9 b), the integrated intensity ratios of {220} to {111} are related to the Raman crystallinity determined by measurements with the 488 nm laser. With increasing crystallinity the degree of preferential orientation increases slightly. One could suggest that the higher crystallinity might be caused dominantly by a crystal

growth in the [110] direction. This can be explained by the low atomic density of the (220) planes which makes them very fast-growing [37]. Higher crystallinity values are related to low silane concentrations during the deposition. A depletion of silane might cause an enhanced formation of the (220) planes with low atomic density which results in a slight shift towards [110] preferential orientation.

Another explanation considers the twin density. Intersecting twin edges with mostly multiple twinned structure can lead to (220) crystal growth due to preferred attachments sites and advantageous kinetics. For further details, it is referred to Houben who did a detailed study based on transmission electron microscopy (TEM) [143].

6.5.4 Summary

The integrated intensity ratios of {220} to {111} determined from Grazing Incidence XRD measurements are in good agreement with the intensity ratio for standard silicon powder revealing a random orientation of the silicon crystals in the investigated µc-Si:H layers. Although the Bragg-Brentano related I_{220}/I_{111} ratios of ~ 0.8 are slightly higher a pronounced preferential (220) orientation is not observed. The standard microcrystalline material had an integrated intensity ratio {220} to {111} of ~ 0.5 that is even lower than the ratio for the randomly oriented material. Also Houben et al. had published a random orientation in µc-Si:H material deposited at IEF5 [35].

The photovoltaic parameters do not confirm that a (220) texture is a necessary requirement for a good solar cell performance and, additionally, an increasing I_{220}/I_{111} ratio for transition material is disproved according to the presented studies.

The slight increase for the Bragg-Brentano I_{220}/I_{111} ratios with increasing Raman crystallinity (at 488 nm) is explained with the assumption that an increase in crystallinity is mainly due the formation of fast-growing (220) planes.

6.6 Depth resolved crystallinity determination

The crystallinity of µc-Si:H depends strongly on the deposition conditions, e.g., silane concentration. In the following studies, the influence of a continuous *SC* change during the deposition on structural properties is investigated. First, as reference, a µc-

Si:H layer was deposited with constant silane concentration. Second, two µc-Si:H layers were prepared with linearly increasing and decreasing *SC,* respectively.

In order to gain information about the change in crystalline volume fraction along the growth direction XRD and Raman measurements, probing the material in different depths, were carried out. Therefore, GI-XRD under varying incident angles and Bragg-Brentano XRD were performed. The derived crystallinity was compared to Raman measurements taken along a well-defined etch crater.

6.6.1 Sample preparation and measurement details

Deposition of samples with silane grading Three µc-Si:H i-layers were deposited on texture-etched ZnO:Al. Microcrystalline p-doped layers were used as seed layers in order to study the material as implemented in solar cells. The deposition time was kept constant for the three samples which resulted in slightly different layer thicknesses of ~ 1.0 – 1.2 µm due to the difference in *SC*. As reference, Sample 1 was deposited under standard µc-Si:H deposition conditions applying a constant reference silane concentration.

In order to induce a change from higher to lower crystalline volume fraction the silane flow rate was increased continuously during the deposition of Sample 2. Accordingly, the silane concentration increased linearly from 0.89 to 1.28 (normalized to reference). A crystallinity gradient from lower to higher crystallinity was aimed for Sample 3. To obtain crystalline material on rather amorphous silicon the silane concentration had to be reduced to a quite low value. Therefore, *SC,* normalized to the reference value, varied linearly from 3.17 to 0.48.

XRD under varying incident angles With increasing incident angle the X-ray probes deeper into the material. Therefore, the determination of, e.g., crystalline volume fraction in different depths is accessible. However, to access a defined depth coordinate is not straightforward. Three different concepts are given by Birkholz [54]. For data evaluation, it has to be considered that all material from the surface to penetration depth of the X-ray contributes to the signal and the derived crystallinity is an integrated value

over the probed volume. Before the measurement, an appropriate range for α was determined as described previously in subsection 2.3.6. For comparison, Bragg-Brentano measurements were performed under the same condition that probed the samples including the initial growth region.

Raman measurement in different depths The Raman signal of the as-deposited samples were measured with λ_{laser} = 488 nm and 647 nm and evaluated regarding the crystalline volume fraction. Due to the different penetration depths of the lasers, the determined values refer to crystalline volume fractions in ~ 0.1 µm and 1 µm depth for 488 nm and 647 nm, respectively. Depth resolved Raman measurements were carried out along a well-defined, wedge-shaped etch crater. Since the crater is not smooth, a small lateral shift can cause a rather big shift in depth that has to be taken into consideration when evaluating the data.

Figure 6.10 illustrates the information depths of the XRD and Raman measurements which were used to determine the evolution of the crystalline phase.

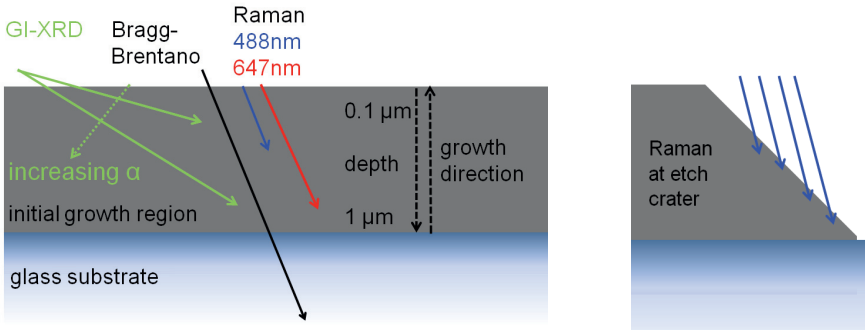

Figure 6.10 Scheme to illustrate information depth of different applied measurement methods

6.6.2 Depth resolved crystallinity determination for µc-Si:H at constant *SC*

XRD crystallinity at different depths Grazing Incidence XRD was measured under four different incident angles α. According to the prior performed omega-scan the measurement at 0.1° probed the sample close to the surface (low depth) whereas the scan under α = 0.35° delivered information including the initial growth region. The BB-

XRD derived crystallinity is assigned to the highest incident angle of 0.35° since the X-ray probes the sample throughout the whole layer thickness including the initial growth region.

The crystalline volume fractions derived from the GI-XRD measurements amount to 75 – 79% as plotted in Figure 6.11 a). The Bragg-Brentano crystallinity revealed an almost identical value. Taken the accuracy of the measurements into account a homogeneous growth is found for µc-Si:H when depositing with constant, sufficiently low silane concentration.

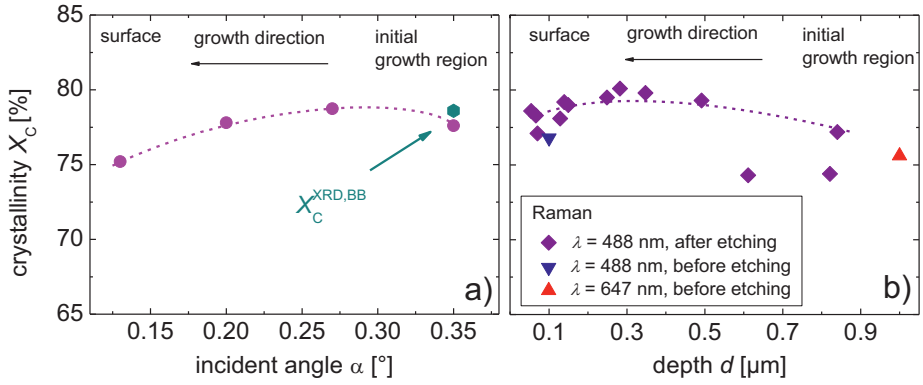

Figure 6.11 a) Crystallinity derived from Grazing Incidence XRD under various incident angles and Bragg-Brentano measurement for Sample 1 deposited with constant silane concentration. b) Raman crystallinity determined before etching and along a well-defined etch crater. The dashed lines are guides to the eye.

Raman crystallinity depending on etch depth The Raman crystallinity for the etched and as-deposited layer varied between 74% and 80% as shown in Figure 6.11 b). The measurements along the etched crater were carried out with the 488 nm laser with a penetration depth of 100 nm. The 100 nm were added to the crater depth to refer to the actual depth of the probed volume. The values are similar to the XRD derived crystallinity values. However, whereas a slight crystallinity increase with layer thickness appears according to the Raman data, GI-XRD data suggests a slightly decreasing crystallinity. However, the differences can be explained by the inaccuracy of

the measurements and evaluation procedure. The slightly lower crystallinity value for the 647 nm before etching is attributed the different cross section of µc-Si:H for laser light with a wavelength of 488 nm and 647 nm as discussed before.

6.6.3 Depth resolved crystallinity determination for µc-Si:H at increasing *SC*

XRD crystallinity at different depths Sample 2 was probed under incident angles α in the range of 0.25° to 0.75°. With increasing incident angle, lower lying layer regions are probed and the scanned volume over which the scattering intensity is collected increases. Due to the change in silane concentration from 0.89 to 1.27 during the deposition, a gradient from higher to lower crystalline volume fraction with thickness is expected, which refers to a gradient from lower to higher crystalline volume fraction with increasing α.

Figure 6.12 a) depicts Bragg-Brentano and GI-XRD crystallinity as a function of the incident angle α. At an incident angle of 0.25° the surface region is probed. The low crystallinity value of 19% is in accordance with the high silane concentration that was applied at the end of the deposition. With increasing α, the X-ray penetrates deeper into the layer and the observed crystallinity increases following the expected trend according to the silane concentration gradient. At an incident angle of α = 0.75° the whole layer including the initial growth region is probed. A value of 52% is found which is higher than the Bragg-Brentano crystallinity of 44% probing into a similar depth.

Influence of overlying material on XRD measurements Although the deposition starts with a lower silane concentration as Sample 1, a lower crystallinity for a probing depth including the initial growth region is observed. This is because the amorphous phase that evolves at the surface of the layer overlies the highly crystalline region and influences the (GI- and BB-) XRD measurements probing deeper into the layer. The determined crystallinity is not a local but an average value over a volume that increases with increasing incident angle. For Sample 1, this effect was not recognized since the layer exhibited a very homogeneous growth.

Raman crystallinity before etching The Raman crystallinity of Sample 2 before and after etching is depicted in Figure 6.12 b). Before etching, a crystalline volume fraction of 47% was found by measuring with the 647 nm laser. This is in accordance with the XRD crystallinity that refers to a similar probed volume (including the initial growth region). With the 488 nm laser the surface region was investigated and a crystalline volume fraction of 18% was determined which is also in very good agreement to the GI-XRD crystallinity at α = 0.25° (19%).

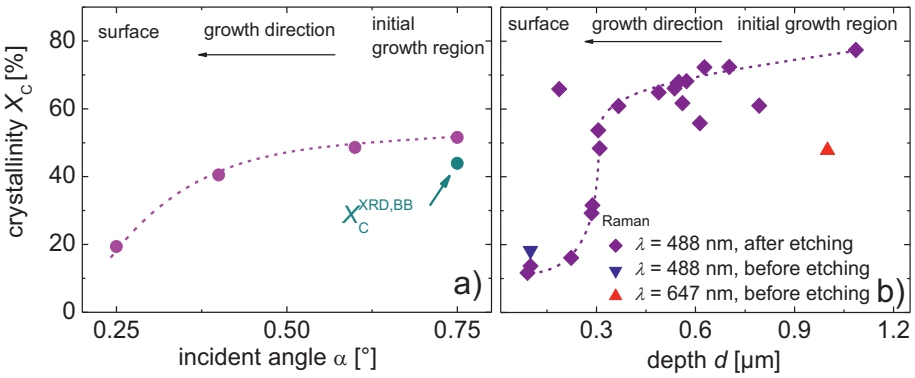

Figure 6.12 a) Crystallinity derived from Grazing Incidence XRD at various incident angles and Bragg-Brentano measurement for Sample 2 deposited with increasing silane concentration. b) Raman crystallinity determined before etching and along a well-defined etch crater. The dashed lines are guides to the eye.

Raman crystallinity depending on etch depth The Raman crystallinity values, shown in Figure 6.12 b), increase when probing deeper lying regions of the µc-Si:H layer In the initial growth region ~ 77% are determined. This value is similar to the crystallinity of Sample 1 for which a slightly higher silane concentration as for Sample 2 was applied at the beginning of the deposition. Due to the increasing silane concentration, the crystallinity decreases to about 58% for a deposited layer thickness of ~ 900 nm. After reaching a certain high silane concentration, the crystallinity drops abruptly over a small thickness range of ~ 100 nm to below 20%.

For Raman measurements at the crater side walls the overlying amorphous material was etched off and did therefore not contribute to the Raman signal. Accordingly, a local crystallinity determination of µc-Si:H material was possible.

6.6.4 Depth resolved crystallinity determination for µc-Si:H at decreasing *SC*

XRD crystallinity at different depths Sample 3 which was slightly thicker (1.2 µm) than Sample 1 and Sample 2 (1 µm) was deposited with a silane concentration that linearly decreased from 3.17 to 0.48 (normalized to the reference value of Sample 1). Figure 6.13 a) shows that the crystallinity derived from GI-XRD under a small incident angle α (referring to the surface region) is higher than at steeper incident angles. This finding goes along with the applied silane concentration gradient. However, over a wide range the crystallinity does not change and amounts to ~ 38%. Bragg-Brentano XRD finds a significantly lower crystallinity value of 16%. With decreasing crystalline volume fraction the evaluation inaccuracy of Bragg-Brentano scans increases due to the small contribution of crystalline phase compared to glass background and amorphous phase and might cause a strong overestimation of amorphous phase. In addition, it might be possible that α was chosen incorrectly so that even with the steepest incident angle the sample was not probed into the depth of initial growth.

Due to the overlying material the calculated crystallinity is influenced by the highly crystalline surface region. The actual crystallinity close to the initial growth region is, according to the high, applied *SC* value, supposed to be much lower and not accessible with the XRD measurements.

Raman crystallinity before etching Raman measurements at the as-deposited sample revealed a crystallinity of 16% when probing into ~ 1 µm depth and 82% at the surface, respectively. These values are in a similar range as the corresponding XRD determined values.

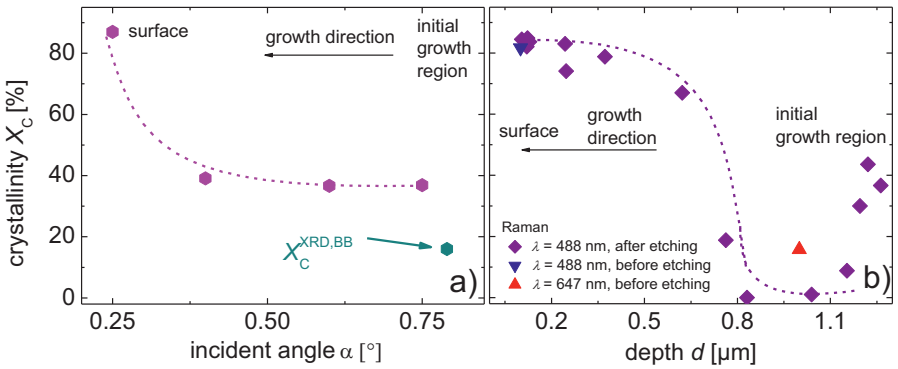

Figure 6.13 a) Crystallinity derived from Grazing Incidence XRD at various incident angles and Bragg-Brentano measurement for Sample 3 deposited with decreasing silane concentration. b) Raman crystallinity determined before etching and along a well-defined etch crater. The dashed lines are guides to the eye.

Raman crystallinity depending on etch depth The crystallinity profile as a function of the etch depth is shown in Figure 6.13 b). In the initial growth region (depth = 1.1–1.2 µm) the high crystallinity values of ~ 40% are attributed to a strong influence of the µc-Si:H p-doped layer for which usually crystallinity values between 40–50% are observed. The crystalline volume fraction decreases and even vanishes totally in the region of ~ 0.80 – 1 µm depth which means that the i-layer grows in the amorphous regime due to the high applied high silane concentration. The crystal growth starts after a sufficiently low silane concentration is reached and the crystallinity increases as expected from the silane concentration grading with thickness. Over a narrow thickness range of < 200 nm the material changes abruptly from amorphous to highly crystalline. At the sample surface a value of 85% is determined which is similar to the GI-XRD derived value at the lowest incident angle (87%).

As it was shown for Sample 2 as well, the transition from crystalline to almost amorphous material (or vice versa) occurs abruptly when a certain threshold silane concentration is applied. This demonstrates the difficulty to reach “transition material” since already a small deviation in *SC* can change the material properties significantly.

6.6.5 Summary

By applying a constant and low silane concentration, highly crystalline silicon was deposited with a good homogeneity throughout the 1 μm thick layer. Grazing Incidence XRD and Raman crystallinity at the etched and as-deposited sample revealed crystalline volume fractions between 74 – 80%.

A linear silane concentration grading resulted in a crystallinity change along the growth direction as expected by the *SC* grading values. Grazing Incidence XRD and Raman measurements with a 647 nm laser are influenced by the overlying material and reveal an average value over the volume from the surface to penetration depth. Raman measurements along a well-defined etch crater access the local crystallinity since the overlying material is removed and does not influence the signal.

The change from crystalline to almost amorphous material or vice versa happens abruptly in a very narrow silane concentration range when a linear silane grading is applied. That expresses the sensitivity of the crystal growth on deposition parameters and thus, the difficulty to achieve high quality transition material for solar cell application.

6.7 Conclusion

Raman spectroscopy and XRD measurements were used to investigate the microstructure of microcrystalline silicon intrinsic layers. The samples were deposited in a silane concentration range of 0.71 – 1.04% to ensure highly crystalline and almost amorphous material which was confirmed by preceding Raman measurements with two different laser wavelengths. For solar cells that were fabricated in the same deposition run as the investigated layer stacks an increase in open-circuit voltage and fill factor with increasing silane concentration was observed. Standard μc-Si:H deposited at $SC = 1.02\%$ exhibited a crystalline volume fraction of 65%. Since the material deposited at 1.04% had a crystalline volume fraction of only 4% the standard material is regarded as “transition material” which is supposed to have excellent properties regarding the application in solar cells. This is confirmed by the solar cell with standard

µc-Si:H as i-layer that achieved the highest V_{oc} and *FF* in the regarded silane concentration series.

The crystallinity derived from additionally performed Grazing Incidence XRD measurements correlated well with the crystallinity derived from Raman measurements with a 488 nm laser. However, measurements with a 647 nm laser revealed a slightly lower crystallinity. This was attributed to a small crystallinity increase throughout the layer growth and to an overestimation of the crystalline phase due to a higher scattering cross section of µc-Si:H for 488 nm laser light.

Significantly lower crystallinity values were determined from Bragg-Brentano scans which is attributed to an underestimation of the diffracting intensity of the glass background leading to an overestimation of amorphous phase.

Besides the characteristic cubic silicon Bragg-reflections an additional peak of a hexagonal polytypic modification was found at the low angle shoulder of the {111} reflection which is caused by stacking faults and twins. The hexagonal fraction increases with crystallinity and varied in case of GI-XRD from 3.0% to 6.2%. The Bragg-Brentano diffractograms revealed higher values between 9.8% and 20%. Thus, it is concluded that stacking faults and twinning appear mainly for crystal planes parallel to the surface.

The occurrence of a preferential (220) orientation, or (220) texture, in µc-Si:H was investigated by Grazing Incidence- and Bragg-Brentano XRD. By comparing the integrated intensity ratios of the {220} and {111} reflections with the cubic standard silicon powder value of 0.55, a random orientation of crystals that grow not parallel to the substrate surface is found. An increased I_{220}/I_{111} ratio of ~ 0.8 indicates a very small preferential orientation along the [110] direction for crystals that grow parallel to the substrate surface. Since the ratio I_{220}/I_{111} increases with crystallinity, one could speculate that the increasing crystalline volume fraction results mainly from growth of fast-growing (220) planes. However, in standard material with the best solar cell performance the crystals are oriented randomly for all growth directions. This evidences that a (220) texture is not a necessary requirement for device-quality µc-Si:H material.

Finally, the evolution of crystallinity in μc-Si:H layers was investigated by XRD and Raman spectroscopy probing into different depths of the samples. As reference, Sample 1 was deposited at constant silane concentration resulting in an almost constant crystallinity. For Sample 2 and Sample 3, the silane concentration increased and decreased, respectively, with a linear slop. The crystallinity determined by GI-XRD and Raman measurements on the as-deposited samples is in good agreement. Both methods reveal an average crystallinity of the samples since the overlying material influences the signal and causes deviations when investigating inhomogeneous material. However, Raman measurements along a well-defined etch crater made the local crystallinity accessible. From the crystallinity taken in different depths it is derived that the transition from material of high to low crystallinity, deposited with increasing silane concentration, and from low to higher crystallinity due to decreasing silane concentration, happens in a very narrow *SC* window. That shows the great importance of an accurate adjustment of deposition parameters to achieve high quality transition material.

Chapter 7

Conclusion

The concept of very thin a-Si:H/µc-Si:H tandem cells deposited on commercially available textured SnO_2:F substrates was successfully demonstrated. Simultaneously reduced intrinsic absorber layer thicknesses of top and bottom cell resulted in a very thin device with only 25% of the standard thickness that reached 75% of the standard thick tandem cell's stabilized efficiency. The low loss in efficiency resulted, e.g., from the increased open-circuit voltage. Since the recombination volume is much smaller compared to thick standard cells the bulk recombination decreased. In addition, higher fill factors were observed indicating a more efficient charge carrier collection. Since the distance the charge carriers have to travel to the contacts is much shorter, and the electrical field as driving force is higher in the thin tandem cells the recombination is reduced. Another advantage is the implementation of very thin amorphous i-layers that exhibit low degradation rates. Thus, it appears that a low efficiency loss faces a high production cost-saving potential since deposition time, material consumption and chamber cleaning efforts are significantly reduced. Oerlikon Solar already recognized this potential and announced the world's lowest module production costs of 0.50 €/W_P for modules with efficiencies of 10.0% manufactured in their new (2010) "ThinFab"

[15]. To reduce the loss in short-circuit current density in the very thin tandem cells an efficient light trapping is necessary. The thin devices might require a different approach then the standard thick tandem cells [96].

The concept of very thin tandem cells allows so-called high band gap amorphous silicon and microcrystalline silicon deposited at high deposition rates without performance deterioration. The application of high band gap material leads to significantly higher open-circuit voltages and is deposited at lower temperatures. An adjustment of the p-type doped layer to the high band gap intrinsic material by, e.g., reducing the deposition temperature improved the cell performance further. The use of high rate microcrystalline silicon reduces the production time. Consequently, these two approaches bear the possibility to further reduce the costs per Watt peak.

The idea of applying very thin absorber layers was extended to the fabrication of the n-i-p tandem cells on self-orderly textured aluminium plates. Light trapping properties and cell performance were investigated to evaluate the usability of the Al plates as substrate for thin tandem cells. Compared to thin tandem cells on texture-etched ZnO:Al and Asahi U, higher short-circuit current densities and considerably lower open-circuit voltages were observed for tandem cells on Al-substrates. This behaviour is attributed compressive stress and higher crystallinity in the μc-Si:H bottom cell, both revealed from Raman measurements. Derived from these investigations the performance of thin tandem cells deposited on Al substrates can so far not compete with the performance of thin tandem cells on texture-etched, coated ZnO:Al or Asahi U.

The structure of intrinsic microcrystalline silicon layers deposited with different silane concentrations at IEF5 were investigated by means of X-ray diffraction and Raman spectroscopy. Neither XRD measurements in the Bragg-Brentano nor in Grazing Incidence geometry evidenced a noteworthy preferential (220) orientation in the microcrystalline silicon layers having different crystalline volume fractions. This finding is in contrast to publications of several research groups that observe such a preferential orientation [132; 139]. The good cell performance of microcrystalline single junctions solar cells that were deposited together with the investigated μc-Si:H layer disproved the necessity of a preferential (220) orientation for solar cell application as it

was claimed previously [129; 130]. Furthermore, a hexagonal contribution which is related to stacking faults and twins in the diffractograms of μc-Si:H layers was observed. Raman spectroscopy along a well-defined etch crater made it possible to determine the local crystalline volume fraction without being influenced by material lying above which is otherwise only accessible by intricate electron microscopy. Together with incident angle dependent XRD layers deposited under non-constant silane concentration conditions were investigated regarding a crystallinity gradient. It appears that the phase transition between amorphous and microcrystalline silicon (and vice versa) appears in a narrow silane concentration range. Consequently, an accurate adjustment and control of the silane concentration is necessary to gain device quality material.

References

1. **D. M. Chapin, C. S. Fuller, P. L. Pearson,** A New Silicon p-n Junction Photocell for Converting Solar Radiation into Electrical Power, *Journal of Applied Physics,* 1954, Vol. 25, pp. 676-677.

2. **D. C. Reynolds, G. Leis, R. E. Marburger,** Photovoltaic Effect in Cadmium Sulfide, *Physical Review,* 1954, Vol. 96, pp. 533-534.

3. **R. Gremmelmeier,** GaAs-Photoelement, *Zeitschrift für Naturforschung,* 1955, Vol. 10a, pp. 501-02.

4. **T. Kirchartz,** *Generalized detailed balance theory of solar cells,* Jülich: Forschungszentrum Jülich GmbH, 2009.

5. **W. E. Spears, P. G. LeComber,** Substitutional doping of amorphous silicon, *Solid State Community.* 1975, Vol. 17, pp. 1193-1196.

6. **D. E. Carlson, C. R. Wronski,** Amorphous Silicon Solar Cells, *Applied Physics Letter,* 1976, Vol. 28, pp. 671-673.

7. **D. L. Staebler, C. R. Wronski,** Reversible conductivity changes in discharged-produced amorphous Si, *Applied Physics Letters,* 1977, Vol. 31, pp. 292-294.

8. **J. Yang, R. Ross, T. Glatfelter, R. Mohr, G. Hammond, C. Bernotaitis, E. Chen, J. Burdick, M. Hopson, S. Guha,** High efficiency multi-junction solar cells using amorphous silicon and amorphous silicon-germanium alloys, Conference Record of the 20th IEEE, Vol. 1, Las Vegas, Nevada, 1988, pp. 241-246.

9. **S. Vepřek, V. Mareček,** The preparation of thin layers of Ge and Si by chemical hydrogen plasma transport, *Solid-State Electron,* 1968, Vol. 11, pp. 683-684 .

10. **K. Prasad, F. Finger, H. Curtins, A. Shah, J. Baumann,** Deposition of phosphorus doped microcrystalline silicon below 70°C at 70 MHz, *Journal of Non-Crystalline Solids,* 1991, Vols. 137-138, pp. 681-684.

11. **M. Heintze, W. Westlake, P. V. Santos.** Surface controlled plasma deposition and etching of silicon near the chemical equilibrium. *Journal of Non-Crystalline Solids.* 1993, Vols. 164-166, 2, pp. 985-988.

12. **J. Meier, R. Flückiger, H. Keppner, A. Shah,** Complete microcrystalline p-i-n solar cell - Crystalline or amorphous cell behavior?, *Applied Physics Letters,* 1994, Vol. 65, pp. 860-862.

13. **K. Yamamoto, A. Nakajima, M. Yoshimi, T. Sawada, S. Fukuda, T. Suezaki, M. Ichikawa, Y. Koi, M. Goto, T. Meguro, T. Matsuda, T. Sasaki, Y. Tawada,** High efficicency thin film silicon hybrid cell and module with newly developed innovative interlayer, Conference Record of the 2006 IEEE 4th World Conference on Photovoltaic Energy Conversion, Waikoloa, Hawaii, 2006, pp. 1489-1492.

14. **Sunfilm AG,** *www.sunfilm.com.* [Online] July 2010. http://www.sunfilm.com/en/communication/index.php?id=42.

15. **Oerlikon Solar,** www.oerlikon.com. [Online] September 2010. www.oerlikon.com/solar/thinfab.

16. **Solarbuzz,** www.solarbuzz.com. [Online] September 2010. http://www.solarbuzz.com/Marketbuzz2010-intro.htm.

17. **Technology & Market Share Forecast.**,www.displaybank.com. [Online] February 2010. http://www.displaybank.com/eng/info/sread.php?id=5730.

18. **Renewable Energy World,** www.renewableenergyworld.com. [Online] November 2009. http://www.renewableenergyworld.com/rea/news/article/2009/11/thin-films-share-of-solar-panel-market-to-double-by-2013.

19. **AZoM.com Pty.Ltd,** www.azonano.com. [Online] 2010. http://www.azonano.com/news.asp?newsID=17842.

20. **Solarbuzz,** www.Solarbuzz.com. [Online] September 2010. http://www.solarbuzz.com/Moduleprices.htm.

21. **First Solar,** Greentechmedia. [Online] July 2010. http://www.greentechmedia.com/articles/read/first-solar-drops-cost-to-76-cents-a-watt/.

22. **R. Rech,** *Solarzellen aus amorphem Silizium mit hohem stabilem Wirkungsgrad,* Jülich: Forschungszentrum Jülich GmbH, 1996.

23. **A. Matsuda, M. Takai, T. Nishimoto, M. Kondo,** Control of plasma chemistry for preparing highly stabilized amorphous silicon, *Solar Energy Material & Solar Cells,* 2003, Vol. 78, pp. 3-26.

24. **A. Matsuda,** Growth mechanism of microcrystalline silicon obtained from reactive plasma, *Thin Solid Films,* 1996, Vol. 337, pp. 1-6.

25. **P. Würfel,** *Physics of Solar Cells,* Weinheim: Wiley-VCH, 2009.

26. **B. E. Pieters,** *Characterization of Thin-Film Silicon Materials and Solar Cells through Numerical Modeling,* Delf: Delft University of Technology, 2008.

27. **K. Deng, E. A. Schiff,** Amorphous Silicon-based Solar Cells, in: S. Hegedus, A. Luque, *Handbook of Photovoltaic Science and Engeneering,* John Wiley & Sons Ltd, 2003.

28. **J. Tauc,** *The Optical Properties of Solids,* New York: New York Academic Press, 1971.

29. **S. Hama, H. Okamoto, Y. Hamakawa, T. Matsubara,** Hydrogen content dependence of the optical energy gap in a-Si:H, *Non-Crystalline Solids,* 1983, Vols. 59-60, pp. 333-336.

30. **M. Meier, S. Muthmann, A. J. Flikweert, G. Dingemans, M. C. M. van de Sanden, A. Gordijn,** In-situ transmission measurements as process control for silicon thin-film solar cells, *Solar Energy Materials & Solar Cells,* 2010, submitted.

31. **A. Kolodziej,** Staebler-Wronski effect in amorphous silicon and its alloys, *Opto-Electronic Reviews,* 2004, Vol. 12, pp. 21-32.

32. **M. Kondo, A. Matsuda,** Preparation and Properties of Nanocrystalline Silicon, in: Y. Hamakawa, *Thin-Film Solar Cells,* Heidelberg: Springer, 2004, pp. 69-89.

33. **M. N. van den Donker, T. Kilper, D. Grunsky, B. Reca, L. Houben, W. M. M. Kessels and M. C. M. van de Sanden,** Microcrystalline silicon deposition: Process stability and process control, *Thin Solid Film,* 2007, Vol. 515, pp. 7455-7459.

34. **O. Vetterl, F. Finger, R. Carius, P. Hapke, L. Houben, O. Kluth, A. Lambertz, A. Mück, B. Rech, H. Wagner,** Intrinsic microcrystalline silicon: A new material for photovoltaics, *Solar Energy Materials and Solar Cells,* 2000, Vol. 62, pp. 97-108.

35. **L. Houben, M. Luysberg, P. Hapke, R. Carius, F. Finger, H. Wagner,** Structural properties of microcrystalline silicon in the transition from highly crystalline to amorphous growth, *Philosophical Magazine A,* 1998, Vol. 77, pp. 1447-1460 .

36. **T. Matsui, M. Kondo, A. Matsuda,** Origin of the improved performance of high-deposition-rate microcrystalline silicon solar cells by high-pressure glow discharge, *Japanese Journal of Applied Physics,* 2003, Vol. 42, pp. 901-903.

37. **H. R. Moutinho, C.-S. Jiang, J. Perkins, Y. Xu, B. P. Nelson, K. M. Jones, M. J. Romero, M. M. Al-Jassim,** Effects of dilution ratio and seed layer on the crystallinity of microcrystalline thin films deposited by hot-wire chemical vapor deposition, *Thin Solid Films,* 2003, Vol. 430, pp. 135-140.

38. **Forschungszentrum Jülich GmbH,** Forschen in Jülich, Information brochure, Forschungszentrum Jülich GmbH, 2002.

39. **A. Matsuda,** Thin-Film Silicon – Growth Process and Solar Cell Application, *Japanese Journal of Applied Physic,.* 2004, Vol. 43, pp. 7909-7920.

40. **J. K. Rath,** Low temperature polycrystalline silicon: a review on deposition, physical properties and solar cell applications, *Solar Energy Material & Solar Cells,* 2003, Vol. 76, pp. 431-487.

41. **R. E. I. Schropp, M. Zeman,** *Amorphous and microcrystalline Silicon Solar Cells: Modeling Materials and Device Technology,* Norwell: Kluwer Academic Publishers, 1998.

42. **R. Brendel,** *Thin-Film Crystalline Silicon Solar Cells,* Weinheim: Wiley-VCH, 2003.

43. **A. V. Shah, H. Schade, M. Vaneček, J. Meier, E. Vallat-Sauvain, N. Wyrsch, U. Kroll, C. Droz, J. Bailat,** Thin-film silicon solar cell technology, *Progress in Photovoltaics,* 2004, Vol. 12, pp. 113-142.

44. **T. Kilper,** *Großflächige Plasmaabscheidung von mikrokristallinem Silizium für mikromorphe Dünnschichtsolarmodule,* Jülich: Forschungszentrum Jülich GmbH, 2008.

45. **F. A. Lindholm, J. G. Fossum, E. L. Burgess** Application of the superposition principle to solar-cell analysis, *IEEE Transactions on Electron Devices,* 1979, Vol. 26, pp. 165-171.

46. **J. Kwak, S. W. Kwon, K. S. Lim,** Fabrication of n-p-p tunnel junction for a protocrystalline silicon multilayer/amorphous silicon tandem solar cell, *Journal of Non-Crystalline Solids,* 2006, Vol. 352, pp. 1847-1850.

47. **L. Gui-Jun, H. Guo-Fu, H. Xiao-Yan, Y. Yu-Jie, W. Chang-Chun, S. Jian, Z. Yin, G. Xin-Hua,** The study of a new n/p tunnel recombination junction and its application in a-Si:H/μc-Si:H tandem solar cells, *Chinese Physics B,* 2009, Vol. 18, p. 1674.

48. **L. Sansonnes, A. A. Howling, C. Hollenstein,** Large area deposition of amorphous and microcrystalline silicon by very high frequency plasma, *Material Research Society Symposium Proceedings,* 1998, Vol. 507, pp. 541-546.

49. **M. Berginski,** *Lichtstreuende Oberflächen, Schichten und Schichtsysteme zur Verbesserung der Lichteinkopplung in Silizium - Dünnschichtsolarzellen,* Jülich: Forschungszentrum Jülich GmbH, 2007.

50. **W. B. Jackson, N. M. Amer, A. C. Boccara, D. Fournier,** Photothermal deflection spectroscopy and detection, *Applied Optics,* 1981, Vol. 20, pp. 1333-1344.

51. **S. Bialkowski,** Photothermal Spectroscopy Methods for Chemical Analysis, *Volume 134 Chemical Analysis: A Series of Monographs on Analytical Chemistry and Its Applications*, J. D. Winefordner, Series Editor, John Wiley & Sons, Inc., 1996.

52. **S. Haas, A. Gordijn, H. Stiebig,** High speed laser processing for monolithical series connection of silicon thin-film modules, *Progress in Photovoltaics,* 2008, Vol. 16, pp. 195-203.

53. **M. Otto,** *Analytische Chemie,* Weinheim: Wiley-VCH, 2000.

54. **M. Birkholz,** *Thin Film Analysis by X-Ray Scattering,* Weinheim: Wiley-VCH, 2006.

55. **D. L. Williamson,** Medium-range order in a-Si:H below and above the onset of microcrystallinity, *Material Research Society Proceedings,* 1999, Vol. 557, pp. 251-261.

56. **K. Ding,** *Charakterisierung und Simulation von a-Si:H/µc-Si:H Tandem Solarzellen,* Jülich: Forschungszentrum Jülich GmbH, 2009.

57. **A. Lambertz, A. Dasgupta, W. Reetz, A. Gordijn, R. Carius, F. Finger,** *Microcrystalline Silicon Oxide as Intermediate Reflector for Thin Film Silicon Solar*

Cells, Proceedings of the 22th European Photovoltaic Solar Energy Conference, Milano, Italy, 2007, pp. 1839-1842.

58. **M. Berginski, C. Das, A. Doumit, J. Hüpkes, B. Rech, M. Wuttig,** *Properties of TiO_2 Layers as Antireflection Coating,* Proceedings of the 22th European Photovoltaic Solar Energy Conference, Milano, Italy, 2007, pp. 2079-2083.

59. **M. Yoshimi, T. Sasaki, T. Sawada, T. Suezaki, T, Meguro, T. Matsuda, K. Santo, K. Wadano, M. Ichikawa,A. Nakajima, K. Yamamoto,** *High efficiency thin film silicon hybrid solar cell module on 1 m^2-class large area substrate,* Proceedings of the Third World Conference on Photovoltaic Energy Conversion Osaka, Japan, 2003, pp. 1566-1569.

60. **T. Repmann, T. Kilper, W. Appenzeller, C. Zahren, H. Stiebig, B. Rech,** *Up-scaling and optimization of thin-film solar cells and modules based on amorphous and microcrystalline silicon*, Proceedings of the 31st IEEE Photovoltaic Specialist Conference and Exhibition, Orlando, Florida, 2005, pp. 1383-1388.

61. **Sunfilm AG.** www.sunfilm.com. [Online] Juli 2010. http://www.sunfilm.com/en/communication/index.php?id=42.

62. **M. Berginski, J. Hüpkes, A. Gordijn, W. Reetz, T. Wätjen, M. Wuttig,** Experimental studies of the light trapping and optical losses in microcrystalline silicon solar cells. *Solar Energy Materials and Solar Cells,* 2008, Vol. 92, pp. 1037-1042.

63. **H. Bach, N. Neuroth,** *The properties of optical glass,* Heidelberg: Springer Verlag, 1995.

64. **M. Schulte, S. Jorke, C. Zahren, J. Hüpkes, H. Stiebig,** *Analysis of the Scattering Properties of Textured TCO Structures for Thin Film Silicon Solar Cells,* Proceedings of the 22nd European Photovoltaic Solar Energy Conference, Milano, Italy, 2007, pp. 2190-2195.

65. **J. Krč, F. Smole, M. Topič,** Potential of Light Trapping in Microcrystallilne Silicon Solar Cells with Textured Surfaces, *Progress in Photovoltaics: Research and Application,* 2003, Vol. 11, pp. 429-436.

66. **P. Lechner, R. Geyer, H. Schade, B. Rech, O. Kluth, H. Stiebig,** *Optical TCO properties and quantum efficencies in thin-film silicon solar cells,* Proceedings of the 19th European Photovoltaic Solar Energy Conference Paris, France, 2004, pp. 1591-1594.

67. **J. Hüpkes, J. Müller, B. Rech,** Texture Etched ZnO:Al, in: A. Klein, B. Rech, K. Ellmer, *Transparent Conductive Zinc Oxide,* Heidelberg: Springer Verlag, 2008, Vol. 104.

68. **H. Zhu, E. Bunte, J. Hüpkes, H. Siekmann, S. M. Huang,** Aluminium doped zinc oxide sputtered from rotatable dual magnetrons for thin film silicon solar cells, *Thin Solid Film,* 2009, Vol. 517, pp. 3161-3166.

69. **H. Zhu, J. Hüpkes, E. Bunte, A. Gerber, S. M. Huang,** Influence of working pressure on ZnO:Al films from tube targets for silicon thin film solar cells, *Thin Solid Films,* 2010, 518, pp. 4997-5002.

70. **S. Schicho, D. Hrunski, R. van Aubel, A. Gordijn,** High potential of thin (<1 μm) a-Si:H/μc-Si:H tandem solar cells, *Progress in Photovoltaics: Research and Applications,* 2010, Vol. 18, pp. 83-89.

71. **B. E. Pieters, H. Stiebig, M. Zeman, R. A. C. M. M. van Swaaij,** Determination of the mobility gap of intrinsic μc-Si:H in p-i-n solar cells, *Journal of Applied Physics,* 2009, Vol. 105, p. 044502.

72. **T. Brammer, H. Stiebig,** Applying analytical and numerical methods for the analysis of microcrystalline silicon solar cells, *Solar Energy Materials & Solar Cells,* 2006, Vol. 90, pp. 3021-3030.

73. **M. Isomura, T. Takahama, S. Tsuda, S. Nakano,** Dependence of Open Circuit Voltage of Amorphous Silicon Solar Cells on Thickness and Doping Level of the p-Layer, *Japanese Journal of Applied Physics,* 1993, Vol. 32, pp. 1902-1907 .

74. **U. Dutta, P. Chatterjee,** The open circuit voltage in amorphous silicon p-i-n solar cells and its relationship to material, device and dark diode parameters, *Journal of Applied Physics,* 2004, Vol. 96, pp. 2261-2271.

75. **K. Ding, T. Kirchartz, B. E. Pieters, C. Ulbrich, S. Schicho, A. Lambertz, R. Carius, U. Rau,** *Detailed analysis of a-Si:H/µc-Si:H tandem solar cell characterization data using numerical simulation*, Proceedings of the 25th European Photovoltaic Solar Energy Conference, Valencia, Spain, 2010, pp. 2908-2914.

76. **Y. Wang, X. Geng, H. Stiebig, F. Finger,** Stability of microcrystalline silicon solar cells with HWCVD buffer layer, *Thin Solid Films,* 2008, Vol. 516, pp. 733-735.

77. **H. Kakinuma, S. Nishikawa, T. Watanabe,** Thickness dependence of Staebler-Wronski-Effect in a-Si:H, *Journal of Non-Crystalline Solids,* 1983, Vols. 59-60, pp. 421-424.

78. **T. Repmann, B. Sehrbrock, C. Zahren, H. Siekmann, J. Müller, B. Rech, W. Psyk, R. Geyer, P. Lechner,** *Thin film solar modules based on amorphous and microcrystalline silicon*, Proceedings of Third World Conference on Photovoltaic Energy Conversion, Osaka, Japan, 2003, pp. 1574-1579.

79. **H. Sakai, T. Yoshida, S. Fujikae, Y. Ichikawa** *Double-stacked a-Si/a-Si and a-SiC/a-Si Tandem Cells With High Stability and High Reliability,* Material Research Society Symposium Proceedings, San Diego, California,1989, pp. 477-482.

80. **Y.-M. Li, F. Jackson, R. R. Ayra,** *A study of Amorphous Silicon-Carbon Alloy Solar Cells,* Proceedings of the 23rd IEEE Photovoltaic Specialists Conference Louisville, Kentucky, 1993. pp. 850-854 .

81. **S. Fujikake, H. Ohta, P. Sichanugrist, M. Ohsawa, Y. Ichikawa, H. Sakai,** a-SiO:H Films and their Application in Solar Cells, *Optoelectronis- Devices and Technology,* 1994, Vol. 9, pp. 379-90.

82. **A. Gordijn, M. Vaneček, W. J. Goedheer, J. K. Rath, R. E. I. Schropp,** Influence of Pressure and Plasma Potential on High Growth Rate Microcrystalline Silicon Grown by Very High Frequency Plasma Enhanced Chemical Vapour Deposition, *Japanese Journal of Applied Physics,* 2006, Vol. 45, pp. 6166-72.

83. **B. Rech, T. Repmann, M. N. van den Donker, M. Berginski, T. Kilper, J. Hüpkes, S. Calnan, H. Stiebig, S. Wieder,** Challenges in microcrystalline silicon based solar cell technology, *Thin Solid Films,* 2006, Vols. 511-512, pp. 548-555.

84. **A. H. M. Smets, T. Matsui, M. Kondo,** High-rate deposition of microcrystalline silicon p-i-n solar cells in the high pressure depletion regime, *Journal of Applied Physics,* 2008, Vol. 104, pp. 034508-1-034508-11.

85. **X. Deng, K. L. Narasiman, J. Evans, M. Izu, S. R. Ovshinsky,** *Dependence of a-Si solar cell V_{oc} on deposition temperature,* Proceedings of 1994 IEEE 1st World Conference on Photovoltaic Energy Conversion - WCPEC Waikoloa, Hawaii, 1994, pp. 678-681.

86. **J. Yang, X. Xu, S. Guha,** *Stability Studies of Hydrogenated Amorphous Silicon Alloy Solar Cells Prepared With Hydrogen Dilution,* Conference Record of the 28th IEEE Photovoltaic Specialists Conference Anchorage, Alaska, 1994, Vol. 336, pp. 742-745.

87. **S. C. Saha, S. Ghosh, S. Ray,** Widegap a-Si:H films prepared at low substrate temperature, *Solar Energy Materials and Solar Cells,* 1997, Vol. 45, pp. 115-126.

88. **S. Muthmann, A. Gordijn,** Amorphous silicon solar cells deposited with non-constant silane concentration, *Solar Energy Materials & Solar Cells,* 2010, Vol. 95, pp. 573-578.

89. **S. Guha, , J. Yang, A. Banerjee, B. Yan, K. Lord,** High quality amorphous silicon materials and cells grown with hydrogen dilution, *Solar Energy Materials and Solar Cells,* 2003, Vol. 78, pp. 329-347.

90. **S. Muthmann, F. Köhler, R. Carius, A. Gordijn,** Structural order on different length scales in amorphous silicon investigated by Raman spectroscopy. *Physica Status Solid.* 2010, Vol. 207, 3, pp. 544-547.

91. **S. Wieder, B. Rech, C. Benking, F. Siebke, W. Reetz, H. Wagner,** *Inflluence of Hydrogen Dilution and SUbstrate Temperature, on the Initial and Stabilized Performance of a-Si:H Solar Cells*, Proceedings of the 13th EC-PVSEC, Nice, France, 1995, pp. 234-237.

92. **P. Siamchai, K. Konagai,** Degradation behavior of amorphous silicon solar cells fabricated by mercury-sensitized photochemical vapor deposition with hydrogen dilution, *Applied Physics Letters,* 1995, Vol. 67, pp. 3468-3470.

93. **B. Vet, M. Zeman,** Relation between the open-circuit voltage and the band gap of absorber and buffer layers in a-Si:H solar cells, *Thin Solid Films,* 2008, Vol. 516, pp. 6873-6876.

94. **S. S. Hegedus, F. Kampas, J. Xi,** Current transport in amorphous silicon n/p junctions and their application as ‘‘tunnel’’ junctions in tandem solar cells. *Applied Physics Letters,* 1995, Vol. 67, pp. 813-815.

95. **A. Gordijn, S. Schicho, S. Muthmann, T. Kilper, H. Zhu, E. Bunte, J. Hüpkes,** Significantly decreased production times for a-Si/µc-Si tandem cells on texture-etched ZnO:Al, *Physica Status Solidi A,* 2010, Vol. 207, pp. 678-681.

96. **A. Gordijn, K. Bittkau, E. Bunte, C. Haase, J. Hüpkes, J. Kirchhoff, S. Schicho, M. Schulte, H. Zhu** *Light-trapping for very thin a-Si:H/µc-Si:H solar cells,* Proceedings 25th European Photovoltaic Solar Energy Conference and Exhibition, Valencia Spain, 2010, pp. 2798-2801.

97. **H. Zhu, E. Bunte, J. Hüpkes, H. Siekmann, S. M. Huang,** Aluminium doped zinc oxide sputtered from rotatable dual magnetrons for thin film silicon solar cells, *Thin Solid Films,* 2009, Vol. 517, pp. 3161-3166.

98. **T. Kilper, T. Repmann, B. Rech, G. Bräuer, S. Wieder,** *Development of microcrystalline silicon solar cells using large area capacitively coupled planar electrodes,* Proceedings of the 20th European Photovoltaic Solar Energy Conference, Barcelona, Spain, 2005, pp. 1544-1547.

99. **K. Tao, D. Zhang, L. Wang, J. Zhao, H. Cai, Y. Sub, Z. Qiao, Q. Hea, Y. Zhanga, Y. Suna,** Development of textured back reflector for n–i–p flexible silicon thin film solar cells, *Solar Energy Materials and Solar Cells.* 2010, Vol. 94, 4, pp. 709-714 .

100. **A. Banerjee, S. Guha,** Study of back reflectors for amorphous silicon alloy solar cell application. *Journal of Applied Physics,* 1991, Vol. 69, pp. 1030-1035.

101. **J. Bailat, V. Terrazzoni-Daudrix, J. Guillet, F. Freitas, X. Niquille, A. Shah, C. Ballif, T. Scharf, R. Morf, A. Hansen, D. Fischer, Y. Ziegler, A. Closset,** *Recent Development of Solar Cells on Low-Cost Plastic Substrates,* Proceedings of the 20th EU Photovoltaic Solar Energy Conference, Barcelona, Spain, 2005, pp. 1529-1532.

102. **V. Terrazzoni-Daudrix, J. Guillet, X. Niquille,L. Feitknecht, F. Freitas, P. Winkler, A. Shah, R. Morf, O. Parriaux, D. Fischer,** *Enhanced light trapping in thin film silicon solar cells deposited on PET and glass,* Proceedings of the Third World Conference on Photovoltaic Energy Conversion, Osaka, Japan, 2003, pp. 1596-1600.

103. **C. Heine, R. H. Morf,** Submicrometer gratings for solar energy applications, *Applied Optics,* 1995, Vol. 34, pp. 2476-2482.

104. **P. Bermel, C. Luo, L. Zeng, L. C. Kimerling, J. D. Joannopoulus,** Improving thin-film crystalline silicon solar cell efficiencies with photonic crystals, *Optics Express,* 2007, Vol. 15, pp. 16968-17000.

105. **H. Stiebig, C. Haase, C. Zahren, B. Rech, N. Senoussaoui,** Thin-film silicon solar cells with grating couplers – An experimental and numerical study, *Journal of Non-Crystalline Solids,* 2006, Vol. 352, pp. 1949-1952.

106. **T. Söderström, F.-J. Haug, X. Niquille, C. Ballif,** TCOs for NIP Thin Film Silicon Solar Cells, *Progress in Photovoltaics: Research and Application,* 2008, Vol. 17, pp. 165-176 .

107. **V. Terrazzoni-Daudrix, F.-J. Haug, T. Söderström, C. Ballif, D. Fischer, W. Soppe, J. Bertomeu, M. Fahland, H. Schlemm, M. Grimm, M. Topic, M. Wutz,** *Final Results of the European Project Flexcellence Roll to Roll technology for the Production of High Efficient Low Cost Thin Film Solar Cells,* Proceedings of 24th European Photovoltaic Solar Energy Conference Hamburg, Germany, 2009, pp. 2831-2834.

108. **H. Sai, H. Fujiwara, M. Kondo, Y. Kanamorie,** Enhancement of light-trapping in thin-film hydrogenated microcrystalline Si solar cells using back reflectors with self order dimple-pattern, *Applied Physics Letters,* 2008, Vol. 93, p. 143501-1-143501-3.

109. **A. P. Li, F. Müller, U. Gösele,** Polycrystalline and Monocrystalline Pore Arrays with Large Interpore Distance in Anodic Alumina, *Electrochemical and Solid State Letters,* 2000, Vol. 3, pp. 131-134.

110. **A. P. Li, F. Müller, A. Birner, K. Nielsch, U. Gösele,** Polycrystalline nanopore arrays with hexagonal ordering on aluminium, *Journal of Vacuum Science and Technology,* 1999, Vol. 17, pp. 1428-1431.

111. **A. P. Li, F. Müller, A. Birner, K. Nielsch, U. Gösele,** Hexagonal pore arrays with a 50-420 nm interpore distance formed by self-organization in anodic alumina, *Journal of Applied Physics,* 1998, Vol. 84, pp. 6023-6026.

112. **H. Sai, Y. Kanamori, M. Kondo,** *Light trapping in Thin-film μc-Si:H Solar Cells using Self-ordered 2D Grating*, IWTFSSC-2*,* Berlin, Germany, 2009.

113. **H. Sai, M. Kondo,** Effect of self-ordered textured back reflectors on light trapping in thin-film microcrystalline silicon solar cells, *Journal of Applied Physics,* 2009, Vol. 105, pp. 094511-094518.

114. **H. Sai, Y. Kanamori, M. Kondo,** *Light trapping in Thin-film μc-Si:H Solar Cells using Self-ordered 2D Grating Reflector*, Proceeding Material Research Society Spring Meeting, San Francisco, California, 2009.

115. **M. Python, E. Vallat-Sauvain, J. Bailat, D. Dominé, L. Fesquet, A. Shah, C. Balif,** Relation between substrate surface morphology and microcrystalline silicon solcar cell performance, *Journal of Non-Crystalline Solids*, 2008, Vols. 19-25, pp. 2258-2262.

116. **L. Feitknecht, J. Steinhauer, R. Schüchter, S. Fay, D. Dominé, E. Vallat-Sauvin, F. Meillaud, C. Balif, A. Shah,** *Investigations on Fill-Factor drop of microcrystalline silicon p-i-n solar cells deposited onto highly surface-textured ZnO substrates*, Proceedings of the 15th International Photovoltaic Science and Engineering Conference, Shanghai, China, 2005, pp. 473-474.

117. **Y. Nasuno, M. Kondo, A. Matsuda,** Microcrystalline silicon thin-film solar cells prepared at low temperature using PECVD, *Solar Energy and Solar Cells,* 2002, Vol. 74, pp. 497-503.

118. **Y. Nasuno, M. Kondo, A. Matsuda,** Effects of substrate surface morphology on microcrystalline silicon solar cells, *Japanese Journal of Applied Physics,* 2001, Vol. 40, pp. 303-305 .

119. **Y. Mai, S. Klein, X. Geng, M. Hülsbeck, R. Carius, F. Finger,** Differences in the structure composition of microcrystalline solar cells deposited by HWCVD and PECVD: Influence on open circuit voltage, *Thin Solid Films*, 2005, Vol. 501, pp. 272-275.

120. **P.A. Tipler,** *Physics for Scientists and Engineers 4th edition,* New York: W.H. Freeman, 1999.

121. **D. Matras, E. Amanatides, E. Katsia, D. Matras, A. Soto, G. A. Voyiatzis,** Temperature effect and stress on microcrystalline silicon thin films deposited under high pressure plasma conditions, *Thin Solid Films*, 2006, Vols. 511-512, pp. 603-607.

122. **S. Vepřek, Z. Iqbal, F.-A. Sarott,** A thermodynamic criterion of the crystalline-to-amorphous transition in silicon, *Philosophical Magazine B*, 1982, Vol. 45, pp. 137-145.

123. **Z. Iqbal, S. Vepřek,** Raman scattering from hydrogenated microcrystalline and amorphous silicon, *Journal of Physcics C: Solid State Physics*, 1982, Vol. 15, pp. 377-392.

124. **S. Vepřek, F.-A. Sarott, Z. Iqbal,** Effect of grain boundaries on he Raman spectra, optical absorption, and elastic light scattering in nanometer-sized crystalline silicon, *Physical Review*, 1987, Vol. 36, pp. 3344-3350.

125. **V. Paillard, P. Puech, P. R. i Cabarrocas,** Measurement of stress gradients in hydrogenated microcrystalline silicon thin films using Raman spectroscopy, *Journal of Non-Crystalline Solids*, 2002, Vols. 299-302, pp. 280-283 .

126. **L. Meyer,** *Formeln und Tabellen für Sekundarstufe 1 und 2,* Berlin: paetec, 2000.

127. **E. A. G. Hamers, A. Fontcuberta i Morral, C. Niikura, R. Brenot, P. Roca i Cabarrocas,** Contribution of ions to the growth of amorphous, polymorphous, and microcrystalline silicon thin films, *Journal of Applied Physics*, 2000, Vol. 88, pp. 3674-3688.

128. **A. Shah, J. Meier, E. Vallat-Sauvain, C. Droz, U. Kroll, N. Wyrsch, J. Guillet, U. Graf,** Microcrystalline silicon and "micromorph" tandem solar cells, *Thin Solid Films*, 2002, Vols. 403-404, pp. 179-187.

129. **Y. Sobajima, T. Sugano, T. Kitagawa, T. Toyama, H. Okamoto,** *Crystallographic Study on Initial Growth Region of μc-Si with Different Preferential Orientations*, Material Research Society Symposium Proceedings, San Francisco, California, 2005, pp. 111-116.

130. **T. Matsui, M. Tsukiji, H. Saika, T. Toyama, H. Okamoto.** Influence of substrate texture on microstructure and photovoltaic performances of thin film polycrystalline silicon solar cells. *Journal of Non-Crystalline Solids.* 2002, Vols. 299-302, pp. 1152-1156.

131. **E. Vallat-Sauvain, U. Kroll, J. Meier, A. Shah, J. Pohl,** Evolution of the Microstructure in Microcrystalline Silicon Prepared by Very High Frequency Glow-Discharge using Hydrogen Dilution, *Journal of Applied Physics*, 2000, Vol. 87, pp. 3137-3142.

132. **L. Houben, M. Luysberg, R. Carius,** Microtwinning in microcrystalline silicon and its effect on grain-size measurements, *Physical Review B*, 2003, Vol. 67, pp. 045312-1-045312-10.

133. **M. Hendriks, S. Radelaar, A. M. Beer, J. Bloem,** Additional X-Ray and Electron Diffraction Peak of Polycrystalline Silicon Films, *Thin Solid Films*, 1984, Vol. 113, pp. 59-72.

134. **M. Luysberg, P. Hapke, R. Carius, F. Finger,** Structure and growth of hydrogenated microcrystalline silicon: Investigation by transmission electron microscopy and Raman spectroscopy of films grown at different plasma excitation frequencies, *Philosophical Magazine A*, 1997, Vol. 75, pp. 31-47.

135. **C. Kittel,** *Einführung in die Festkörperphysik*, München: Oldenbourg Verlag München Wien, 1995.

136. **27-1402, ASTM card number.**

137. **K. Wang, D. Han, D. L. Williamson, B. Huie, J. R. Weinberg-Wolf, B. Yan, J. Yang, S. Guha** *Structural and Electronic Properties of Hydrogenated Nanocrystalline Silicon Films Made with Hydrogen Dilution Profiling Technique*, Material Research Society Symposium Proceedings, San Francisco, California, 2005, pp. 117-121.

138. **T. Sugano, T. Kitagawa, Y. Sobajima, T. Toyama, H. Okamoto,** Hybrid-phase growth in microcrystalline silicon thin films deposited by plasma enhanced chemical vapor deposition at low temperature, *Journal of Applied Physics*, 2005, Vol. 97, pp. 094910-1-6.

139. **K. Saito, M. Kondo,** Investigation of crystalline orientation factor in microcrystallin silicon thin film deposition, *Physica Status Solidi A*, 2010, Vol. 207, pp. 535-538.

140. **A. Matsuda, K. Kumagai, K. Tanaka,** Wide-Range Control of Crystallite Size and Its Orientation in Glow-Discharge Deposited μc-Si:H, *Japanese Journal Applied Physics*, 1983, Vol. 22, pp. 34-36.

141. **K. Saito, M. Kondo,** *Mechanism of <110> preferential orientation in microcrystalline silicon growth and its influence on post-oxidation property*, Proceedings of Photovoltaic Specialists Conference (PVSC), Honolulu, Hawaii, 2010 pp. 003729-003734,

142. **L. Houben,** *Plasmaunterstützte Abscheidung von mikrokristallinem Silizium: Merkmale und Mikrostruktur und deren Deutung im Sinne von Wachtumsvorgängen.* Jülich: Forschungszentrum Jülich, 1999.

Danksagung

Ich konnte bei der Anfertigung meiner Doktorarbeit am IEF5 am Forschungszentrum Jülich auf die Hilfe und Unterstützung vieler Kollegen und Freunde zurückgreifen. Mein ganz besonderer Dank gilt:

Prof. Uwe Rau für die sehr gute Betreuung meiner Arbeit und die wissenschaftliche wie persönliche Unterstützung;

Dr. Aad Gordijn, der mir nicht nur die Wichtigkeit von Referenzen beibrachte, für das interessante Thema, die Möglichkeit, einen Teil meiner Arbeit in Japan durchführen zu können, und das allzeit gute Gruppenklima;

Prof. Rainer Waser für die Übernahme des Koreferats meiner Doktorarbeit;

Prof. Reinhard Carius für die hilfreichen Diskussionen, das immer kritische Hinterfragen und das Heranführen an das ursprünglich eher unliebsame Thema der XRD;

Dr. Thomas Kirchartz für die geduldigen Versuche „am Laufenden Band", mir die Theorie näherzubringen;

Wolfgang Appenzeller, Joachim Kirchhoff und Stefan Muthmann für die gute Stimmung an der PECVD-Anlage, das kollegiale Zusammenarbeiten und die gegenseitige Unterstützung beim Deponieren;

Dr. Werner Fischer (IEF-1), Mirko Ziegner (IEF-1) und Dr. Lothar Houben (IFF) für die Nutzung der XRD-Anlage, die auch mal länger dauern konnte, die gute Zusammenarbeit und hilfreichen Diskussionen;

Florian Köhler für seine „ätzende" Arbeit und zahlreichen Raman-Messungen;

Markus Hülsbeck, Josef Klomfaß, Christoph Zahren, Rebecca van Aubel, Gunnar Schöpe, Janine Worbs und Hilde Siekmann für die zahlreichen und schnellen Raman- und PDS-Messungen, die Degradationsexperimente, Laserlinien und Rückkontakte;

Dr. Jürgen Hüpkes, Andreas Lambertz, Wilfried Reetz, Dr. Eerke Bunte und Dr. Bart Pieters für die Unterstützung und die nette Zusammenarbeit;

Alain Doumit, da er mich selbst in den stressigsten Phasen geduldig in unserem Büro ertragen hat;

Andrea Mülheims und Suanne Griesen für die Hilfe beim Bürokratie-Wirrwarr, allem Organisatorischen und dem persönlichen „Beistand“;

Carolin Ulbrich für ihre stetige Hilfsbereitschaft, die lustigen Lernabende und das Teilen gemeinsamer „Ängste“;

Dr. Matthias Meier für seine positive und ruhige Art, sowie die fachliche und persönliche Unterstützung;

Michael Göldner für den Beistand und Ansporn in den letzten 15 Jahren auf der „Suche nach dem Schicho²“, das Bestehen darauf, dass es kein Vakuum gibt und das Interesse an meiner Arbeit;

meiner Schwester Cornelia und meinem Freund Christian für all die Unterstützung und Hilfe, wann immer sie gebraucht wurde;

meiner Familie, sowie Bernd und Lydia Weber vor allem für das Verständnis für „gestresste Doktoranden“.

Additional, I would like to thank Dr. Michio Kondo (AIST Japan) for giving me the possibility to do parts of my studies at AIST, Tsukuba, and supporting my scientific and cultural studies there. Also, I would like to thank my Japanese colleagues for all interesting discussions and helping me with the Japanese working equipment. Especially, I want to thank: Yoscina Miyanuma, Dr. Hitoshi Sai for his patience and forgiven me all emergency alarms, Dr. Takuya Matsui, not only for breaking countless substrates and Dr. Kimihiko Saito and his family; Thank you all for let me having such an interesting time in Japan

どもありがとお ございます

Curriculum Vitae

Name:	Sandra Schicho
Date and place of birth	03.04.1983, Greiz (Germany)

06/2007 – 11/2010	**PhD thesis** at Institut für Energie- und Klimaforschung (Photovoltaik), Forschungszentrum Jülich GmbH, Title: "Amorphous and microcrystalline silicon applied in very thin tandem solar cells"
03/2009 – 09/2009	**Research Project** at Research Center for Photovoltaics (RCPV), Advanced Institute for Science and Technology (AIST) Tsukuba, Japan Topic: Thin tandem solar cells in n-i-p configuration
07/2006 – 04/2007	**Diploma thesis** at Institut für Festkörperforschung (IFF), Forschungszentrum Jülich GmbH Topic: "Electrical Characterization of STO-thin-films depending on the microstructure of the platinum bottom electrode"
10/2001 – 04/2007	**Studies of Applied Natural Science** at Technische Universität Bergakademie Freiberg, Major: Microelectronics, Semiconductor Physics

1. **Einsatz von multispektralen Satellitenbilddaten in der Wasserhaushalts- und Stoffstrommodellierung – dargestellt am Beispiel des Rureinzugsgebietes**
   von C. Montzka (2008), XX, 238 Seiten
   ISBN: 978-3-89336-508-1

2. **Ozone Production in the Atmosphere Simulation Chamber SAPHIR**
   by C. A. Richter (2008), XIV, 147 pages
   ISBN: 978-3-89336-513-5

3. **Entwicklung neuer Schutz- und Kontaktierungsschichten für Hochtemperatur-Brennstoffzellen**
   von T. Kiefer (2008), 138 Seiten
   ISBN: 978-3-89336-514-2

4. **Optimierung der Reflektivität keramischer Wärmedämmschichten aus Yttrium-teilstabilisiertem Zirkoniumdioxid für den Einsatz auf metallischen Komponenten in Gasturbinen**
   von A. Stuke (2008), X, 201 Seiten
   ISBN: 978-3-89336-515-9

5. **Lichtstreuende Oberflächen, Schichten und Schichtsysteme zur Verbesserung der Lichteinkopplung in Silizium-Dünnschichtsolarzellen**
   von M. Berginski (2008), XV, 171 Seiten
   ISBN: 978-3-89336-516-6

6. **Politikszenarien für den Klimaschutz IV – Szenarien bis 2030**
   hrsg.von P. Markewitz, F. Chr. Matthes (2008), 376 Seiten
   ISBN 978-3-89336-518-0

7. **Untersuchungen zum Verschmutzungsverhalten rheinischer Braunkohlen in Kohledampferzeugern**
   von A. Schlüter (2008), 164 Seiten
   ISBN 978-3-89336-524-1

8. **Inorganic Microporous Membranes for Gas Separation in Fossil Fuel Power Plants**
   by G. van der Donk (2008), VI, 120 pages
   ISBN: 978-3-89336-525-8

9. **Sinterung von Zirkoniumdioxid-Elektrolyten im Mehrlagenverbund der oxidkeramischen Brennstoffzelle (SOFC)**
   von R. Mücke (2008), VI, 165 Seiten
   ISBN: 978-3-89336-529-6

10. **Safety Considerations on Liquid Hydrogen**
    by K. Verfondern (2008), VIII, 167 pages
    ISBN: 978-3-89336-530-2

11. **Kerosinreformierung für Luftfahrtanwendungen**
von R. C. Samsun (2008), VII, 218 Seiten
ISBN: 978-3-89336-531-9

12. **Der 4. Deutsche Wasserstoff Congress 2008 – Tagungsband**
hrsg. von D. Stolten, B. Emonts, Th. Grube (2008), 269 Seiten
ISBN: 978-3-89336-533-3

13. **Organic matter in Late Devonian sediments as an indicator for environmental changes**
by M. Kloppisch (2008), XII, 188 pages
ISBN: 978-3-89336-534-0

14. **Entschwefelung von Mitteldestillaten für die Anwendung in mobilen Brennstoffzellen-Systemen**
von J. Latz (2008), XII, 215 Seiten
ISBN: 978-3-89336-535-7

15. **RED-IMPACT**
Impact of Partitioning, Transmutation and Waste Reduction Technologies on the Final Nuclear Waste Disposal
SYNTHESIS REPORT
ed. by W. von Lensa, R. Nabbi, M. Rossbach (2008), 178 pages
ISBN 978-3-89336-538-8

16. **Ferritic Steel Interconnectors and their Interactions with Ni Base Anodes in Solid Oxide Fuel Cells (SOFC)**
by J. H. Froitzheim (2008), 169 pages
ISBN: 978-3-89336-540-1

17. **Integrated Modelling of Nutrients in Selected River Basins of Turkey**
Results of a bilateral German-Turkish Research Project
project coord. M. Karpuzcu, F. Wendland (2008), XVI, 183 pages
ISBN: 978-3-89336-541-8

18. **Isotopengeochemische Studien zur klimatischen Ausprägung der Jüngeren Dryas in terrestrischen Archiven Eurasiens**
von J. Parplies (2008), XI, 155 Seiten, Anh.
ISBN: 978-3-89336-542-5

19. **Untersuchungen zur Klimavariabilität auf dem Tibetischen Plateau - Ein Beitrag auf der Basis stabiler Kohlenstoff- und Sauerstoffisotope in Jahrringen von Bäumen waldgrenznaher Standorte**
von J. Griessinger (2008), XIII, 172 Seiten
ISBN: 978-3-89336-544-9

20. **Neutron-Irradiation + Helium Hardening & Embrittlement Modeling of 9%Cr-Steels in an Engineering Perspective (HELENA)**
by R. Chaouadi (2008), VIII, 139 pages
ISBN: 978-3-89336-545-6

21. **in Bearbeitung**

22. **Verbundvorhaben APAWAGS (AOEV und Wassergenerierung) – Teilprojekt: Brennstoffreformierung – Schlussbericht**
von R. Peters, R. C. Samsun, J. Pasel, Z. Porš, D. Stolten (2008), VI, 106 Seiten
ISBN: 978-3-89336-547-0

23. **FREEVAL**
Evaluation of a Fire Radiative Power Product derived from Meteosat 8/9 and Identification of Operational User Needs
Final Report
project coord. M. Schultz, M. Wooster (2008), 139 pages
ISBN: 978-3-89336-549-4

24. **Untersuchungen zum Alkaliverhalten unter Oxycoal-Bedingungen**
von C. Weber (2008), VII, 143, XII Seiten
ISBN: 978-3-89336-551-7

25. **Grundlegende Untersuchungen zur Freisetzung von Spurstoffen, Heißgaschemie, Korrosionsbeständigkeit keramischer Werkstoffe und Alkalirückhaltung in der Druckkohlenstaubfeuerung**
von M. Müller (2008), 207 Seiten
ISBN: 978-3-89336-552-4

26. **Analytik von ozoninduzierten phenolischen Sekundärmetaboliten in *Nicotiana tabacum* L. cv Bel W3 mittels LC-MS**
von I. Koch (2008), III, V, 153 Seiten
ISBN 978-3-89336-553-1

27. **IEF-3 Report 2009. Grundlagenforschung für die Anwendung**
(2009), ca. 230 Seiten
ISBN: 978-3-89336-554-8

28. **Influence of Composition and Processing in the Oxidation Behavior of MCrAlY-Coatings for TBC Applications**
by J. Toscano (2009), 168 pages
ISBN: 978-3-89336-556-2

29. **Modellgestützte Analyse signifikanter Phosphorbelastungen in hessischen Oberflächengewässern aus diffusen und punktuellen Quellen**
von B. Tetzlaff (2009), 149 Seiten
ISBN: 978-3-89336-557-9

30. **Nickelreaktivlot / Oxidkeramik – Fügungen als elektrisch isolierende Dichtungskonzepte für Hochtemperatur-Brennstoffzellen-Stacks**
von S. Zügner (2009), 136 Seiten
ISBN: 978-3-89336-558-6

31. **Langzeitbeobachtung der Dosisbelastung der Bevölkerung in radioaktiv kontaminierten Gebieten Weißrusslands – Korma-Studie**
von H. Dederichs, J. Pillath, B. Heuel-Fabianek, P. Hill, R. Lennartz (2009), Getr. Pag.
ISBN: 978-3-89336-532-3

32. **Herstellung von Hochtemperatur-Brennstoffzellen über physikalische Gasphasenabscheidung**
von N. Jordán Escalona (2009), 148 Seiten
ISBN: 978-3-89336-532-3

33. **Real-time Digital Control of Plasma Position and Shape on the TEXTOR Tokamak**
by M. Mitri (2009), IV, 128 pages
ISBN: 978-3-89336-567-8

34. **Freisetzung und Einbindung von Alkalimetallverbindungen in kohlebefeuerten Kombikraftwerken**
von M. Müller (2009), 155 Seiten
ISBN: 978-3-89336-568-5

35. **Kosten von Brennstoffzellensystemen auf Massenbasis in Abhängigkeit von der Absatzmenge**
von J. Werhahn (2009), 242 Seiten
ISBN: 978-3-89336-569-2

36. **Einfluss von Reoxidationszyklen auf die Betriebsfestigkeit von anodengestützten Festoxid-Brennstoffzellen**
von M. Ettler (2009), 138 Seiten
ISBN: 978-3-89336-570-8

37. **Großflächige Plasmaabscheidung von mikrokristallinem Silizium für mikromorphe Dünnschichtsolarmodule**
von T. Kilper (2009), XVII, 154 Seiten
ISBN: 978-3-89336-572-2

38. **Generalized detailed balance theory of solar cells**
by T. Kirchartz (2009), IV, 198 pages
ISBN: 978-3-89336-573-9

39. **The Influence of the Dynamic Ergodic Divertor on the Radial Electric Field at the Tokamak TEXTOR**
von J. W. Coenen (2009), xii, 122, XXVI pages
ISBN: 978-3-89336-574-6

40. **Sicherheitstechnik im Wandel Nuklearer Systeme**
von K. Nünighoff (2009), viii, 215 Seiten
ISBN: 978-3-89336-578-4

41. **Pulvermetallurgie hochporöser NiTi-Legierungen für Implanat- und Dämpfungsanwendungen**
von M. Köhl (2009), XVII, 199 Seiten
ISBN: 978-3-89336-580-7

42. **Einfluss der Bondcoatzusammensetzung und Herstellungsparameter auf die Lebensdauer von Wärmedämmschichten bei zyklischer Temperaturbelastung**
von M. Subanovic (2009), 188, VI Seiten
ISBN: 978-3-89336-582-1

43. **Oxygen Permeation and Thermo-Chemical Stability of Oxygen Permeation Membrane Materials for the Oxyfuel Process**
by A. J. Ellett (2009), 176 pages
ISBN: 978-3-89336-581-4

44. **Korrosion von polykristallinem Aluminiumoxid (PCA) durch Metalljodidschmelzen sowie deren Benetzungseigenschaften**
von S. C. Fischer (2009), 148 Seiten
ISBN: 978-3-89336-584-5

45. **IEF-3 Report 2009. Basic Research for Applications**
(2009), 217 Seiten
ISBN: 978-3-89336-585-2

46. **Verbundvorhaben ELBASYS (Elektrische Basissysteme in einem CFK-Rumpf) - Teilprojekt: Brennstoffzellenabgase zur Tankinertisierung - Schlussbericht**
von R. Peters, J. Latz, J. Pasel, R. C. Samsun, D. Stolten
(2009), xi, 202 Seiten
ISBN: 978-3-89336-587-6

47. **Aging of ^{14}C-labeled Atrazine Residues in Soil: Location, Characterization and Biological Accessibility**
by N. D. Jablonowski (2009), IX, 104 pages
ISBN: 978-3-89336-588-3

48. **Entwicklung eines energetischen Sanierungsmodells für den europäischen Wohngebäudesektor unter dem Aspekt der Erstellung von Szenarien für Energie- und CO_2 - Einsparpotenziale bis 2030**
von P. Hansen (2009), XXII, 281 Seiten
ISBN: 978-3-89336-590-6

49. **Reduktion der Chromfreisetzung aus metallischen Interkonnektoren für Hochtemperaturbrennstofzellen durch Schutzschichtsysteme**
von R. Trebbels (2009), iii, 135 Seiten
ISBN: 978-3-89336-591-3

50. **Bruchmechanische Untersuchung von Metall / Keramik-Verbundsystemen für die Anwendung in der Hochtemperaturbrennstoffzelle**
von B. Kuhn (2009), 118 Seiten
ISBN: 978-3-89336-592-0

51. **Wasserstoff-Emissionen und ihre Auswirkungen auf den arktischen Ozonverlust**
Risikoanalyse einer globalen Wasserstoffwirtschaft
von T. Feck (2009), 180 Seiten
ISBN: 978-3-89336-593-7

52. **Development of a new Online Method for Compound Specific Measurements of Organic Aerosols**
by T. Hohaus (2009), 156 pages
ISBN: 978-3-89336-596-8

53. **Entwicklung einer FPGA basierten Ansteuerungselektronik für Justageeinheiten im Michelson Interferometer**
von H. Nöldgen (2009), 121 Seiten
ISBN: 978-3-89336-599-9

54. **Observation – and model – based study of the extratropical UT/LS**
by A. Kunz (2010), xii, 120, xii pages
ISBN: 978-3-89336-603-3

55. **Herstellung polykristalliner Szintillatoren für die Positronen-Emissions-Tomographie (PET)**
von S. K. Karim (2010), VIII, 154 Seiten
ISBN: 978-3-89336-610-1

56. **Kombination eines Gebäudekondensators mit H2-Rekombinatorelementen in Leichwasserreaktoren**
von S. Kelm (2010), vii, 119 Seiten
ISBN: 978-3-89336-611-8

57. **Plant Leaf Motion Estimation Using A 5D Affine Optical Flow Model**
by T. Schuchert (2010), X, 143 pages
ISBN: 978-3-89336-613-2

58. **Tracer-tracer relations as a tool for research on polar ozone loss**
by R. Müller (2010), 116 pages
ISBN: 978-3-89336-614-9

59. **Sorption of polycyclic aromatic hydrocarbon (PAH) to Yangtze River sediments and their components**
by J. Zhang (2010), X, 109 pages
ISBN: 978-3-89336-616-3

60. **Weltweite Innovationen bei der Entwicklung von CCS-Technologien und Möglichkeiten der Nutzung und des Recyclings von CO_2**
Studie im Auftrag des BMWi
von W. Kuckshinrichs et al. (2010), X, 139 Seiten
ISBN: 978-3-89336-617-0

61. **Herstellung und Charakterisierung von sauerstoffionenleitenden Dünnschichtmembranstrukturen**
von M. Betz (2010), XII, 112 Seiten
ISBN: 978-3-89336-618-7

62. **Politikszenarien für den Klimaschutz V – auf dem Weg zum Strukturwandel, Treibhausgas-Emissionsszenarien bis zum Jahr 2030**
hrsg. von P. Hansen, F. Chr. Matthes (2010), 276 Seiten
ISBN: 978-3-89336-619-4

63. **Charakterisierung Biogener Sekundärer Organischer Aerosole mit Statistischen Methoden**
von C. Spindler (2010), iv, 163 Seiten
ISBN: 978-3-89336-622-4

64. **Stabile Algorithmen für die Magnetotomographie an Brennstoffzellen**
von M. Wannert (2010), ix, 119 Seiten
ISBN: 978-3-89336-623-1

65. **Sauerstofftransport und Degradationsverhalten von Hochtemperaturmembranen für CO2-freie Kraftwerke**
von D. Schlehuber (2010), VII, 139 Seiten
ISBN: 978-3-89336-630-9

66. **Entwicklung und Herstellung von foliengegossenen, anodengestützten Festoxidbrennstoffzellen**
von W. Schafbauer (2010), VI, 164 Seiten
ISBN: 978-3-89336-631-6

67. **Disposal strategy of proton irradiated mercury from high power spallation sources**
by S. Chiriki (2010), xiv, 124 pages
ISBN: 978-3-89336-632-3

68. **Oxides with polyatomic anions considered as new electrolyte materials for solid oxide fuel cells (SOFCs)**
by O. H. Bin Hassan (2010), vii, 121 pages
ISBN: 978-3-89336-633-0

69. **Von der Komponente zum Stack: Entwicklung und Auslegung von HT-PEFC-Stacks der 5 kW-Klasse**
von A. Bendzulla (2010), IX, 203 Seiten
ISBN: 978-3-89336-634-7

70. **Satellitengestützte Schwerewellenmessungen in der Atmosphäre und Perspektiven einer zukünftigen ESA Mission (PREMIER)**
von S. Höfer (2010), 81 Seiten
ISBN: 978-3-89336-637-8

71. **Untersuchungen der Verhältnisse stabiler Kohlenstoffisotope in atmosphärisch relevanten VOC in Simulations- und Feldexperimenten**
von H. Spahn (2010), IV, 210 Seiten
ISBN: 978-3-89336-638-5

72. **Entwicklung und Charakterisierung eines metallischen Substrats für nanostrukturierte keramische Gastrennmembranen**
von K. Brands (2010), vii, 137 Seiten
ISBN: 978-3-89336-640-8

73. **Hybridisierung und Regelung eines mobilen Direktmethanol-Brennstoffzellen-Systems**
von J. Chr. Wilhelm (2010), 220 Seiten
ISBN: 978-3-89336-642-2

74. **Charakterisierung perowskitischer Hochtemperaturmembranen zur Sauerstoffbereitstellung für fossil gefeuerte Kraftwerksprozesse**
von S.A. Möbius (2010) III, 208 Seiten
ISBN: 978-3-89336-643-9

75. **Characterization of natural porous media by NMR and MRI techniques: High and low magnetic field studies for estimation of hydraulic properties**
by L.-R. Stingaciu (2010), 96 pages
ISBN: 978-3-89336-645-3

76. **Hydrological Characterization of a Forest Soil Using Electrical Resistivity Tomography**
by Chr. Oberdörster (2010), XXI, 151 pages
ISBN: 978-3-89336-647-7

77. **Ableitung von atomarem Sauerstoff und Wasserstoff aus Satellitendaten und deren Abhängigkeit vom solaren Zyklus**
von C. Lehmann (2010), 127 Seiten
ISBN: 978-3-89336-649-1

78. **18th World Hydrogen Energy Conference 2010 – WHEC2010 Proceedings**
Speeches and Plenary Talks
ed. by D. Stolten, B. Emonts (2010)
ISBN: 978-3-89336-658-3

78-1. **18th World Hydrogen Energy Conference 2010 – WHEC2010 Proceedings**
Parallel Sessions Book 1:
Fuel Cell Basics / Fuel Infrastructures
ed. by D. Stolten, T. Grube (2010), ca. 460 pages
ISBN: 978-3-89336-651-4

78-2. **18th World Hydrogen Energy Conference 2010 – WHEC2010 Proceedings**
Parallel Sessions Book 2:
Hydrogen Production Technologies – Part 1
ed. by D. Stolten, T. Grube (2010), ca. 400 pages
ISBN: 978-3-89336-652-1

78-3. **18th World Hydrogen Energy Conference 2010 – WHEC2010 Proceedings**
Parallel Sessions Book 3:
Hydrogen Production Technologies – Part 2
ed. by D. Stolten, T. Grube (2010), ca. 640 pages
ISBN: 978-3-89336-653-8

78-4. **18th World Hydrogen Energy Conference 2010 – WHEC2010 Proceedings**
Parallel Sessions Book 4:
Storage Systems / Policy Perspectives, Initiatives and Cooperations
ed. by D. Stolten, T. Grube (2010), ca. 500 pages
ISBN: 978-3-89336-654-5

78-5. **18th World Hydrogen Energy Conference 2010 – WHEC2010 Proceedings**
Parallel Sessions Book 5:
Stategic Analysis / Safety Issues / Existing and Emerging Markets
ed. by D. Stolten, T. Grube (2010), ca. 530 pages
ISBN: 978-3-89336-655-2

78-6. **18th World Hydrogen Energy Conference 2010 – WHEC2010 Proceedings**
Parallel Sessions Book 6:
Stationary Applications / Transportation Applications
ed. by D. Stolten, T. Grube (2010), ca. 330 pages
ISBN: 978-3-89336-656-9

78 Set (complete book series)

18th World Hydrogen Energy Conference 2010 – WHEC2010 Proceedings
ed. by D. Stolten, T. Grube, B. Emonts (2010)
ISBN: 978-3-89336-657-6

79. **Ultrafast voltex core dynamics investigated by finite-element micromagnetic simulations**
by S. Gliga (2010), vi, 144 pages
ISBN: 978-3-89336-660-6

80. **Herstellung und Charakterisierung von keramik- und metallgestützten Membranschichten für die CO_2-Abtrennung in fossilen Kraftwerken**
von F. Hauler (2010), XVIII, 178 Seiten
ISBN: 978-3-89336-662-0

81. **Experiments and numerical studies on transport of sulfadiazine in soil columns**
by M. Unold (2010), xvi, 115 pages
ISBN: 978-3-89336-663-7

82. **Prompt-Gamma-Neutronen-Aktivierungs-Analyse zur zerstörungsfreien Charakterisierung radioaktiver Abfälle**
von J.P.H. Kettler (2010), iv, 205 Seiten
ISBN: 978-3-89336-665-1

83. **Transportparameter dünner geträgerter Kathodenschichten der oxidkeramischen Brennstoffzelle**
von C. Wedershoven (2010), vi, 137 Seiten
ISBN: 978-3-89336-666-8

84. **Charakterisierung der Quellverteilung von Feinstaub und Stickoxiden in ländlichem und städtischem Gebiet**
von S. Urban (2010), vi, 211 Seiten
ISBN: 978-3-89336-669-9

85. **Optics of Nanostructured Thin-Film Silicon Solar Cells**
by C. Haase (2010), 150 pages
ISBN: 978-3-89336-671-2

86. **Entwicklung einer Isolationsschicht für einen Leichtbau-SOFC-Stack**
von R. Berhane (2010), X, 162 Seiten
ISBN: 978-3-89336-672-9

87. **Hydrogen recycling and transport in the helical divertor of TEXTOR**
by M. Clever (2010), x, 172 pages
ISBN: 978-3-89336-673-6

88. **Räumlich differenzierte Quantifizierung der N- und P-Einträge in Grundwasser und Oberflächengewässer in Nordrhein-Westfalen unter besonderer Berücksichtigung diffuser landwirtschaftlicher Quellen**
von F. Wendland et. al. (2010), xii, 216 Seiten
ISBN: 978-3-89336-674-3

89. **Oxidationskinetik innovativer Kohlenstoffmaterialien hinsichtlich schwerer Lufteinbruchstörfälle in HTR´s und Graphitentsorgung oder Aufarbeitung**
von B. Schlögl (2010), ix, 117 Seiten
ISBN: 978-3-89336-676-7

90. **Chemische Heißgasreinigung bei Biomassenvergasungsprozessen**
von M. Stemmler (2010), xv, 196 Seiten
ISBN: 978-3-89336-678-1

91. **Untersuchung und Optimierung der Serienverschaltung von Silizium-Dünnschicht-Solarmodulen**
von S. Haas (2010), ii, 202 Seiten
ISBN: 978-3-89336-680-4

92. **Non-invasive monitoring of water and solute fluxes in a cropped soil**
by S. Garré (2010), xxiv, 133 pages
ISBN: 978-3-89336-681-1

93. **Improved hydrogen sorption kinetics in wet ball milled Mg hydrides**
by L. Meng (2011), II, 119 pages
ISBN: 978-3-89336-687-3

94. **Materials for Advanced Power Engineering 2010**
ed. by J. Lecomte-Beckers, Q. Contrepois, T. Beck and B. Kuhn
(2010), 1327 pages
ISBN: 978-3-89336-685-9

95. **2D cross-hole MMR – Survey design and sensitivity analysis for cross-hole applications of the magnetometric resistivity**
by D. Fielitz (2011), xvi, 123 pages
ISBN: 978-3-89336-689-7

96. **Untersuchungen zur Oberflächenspannung von Kohleschlacken unter Vergasungsbedingungen**
von T. Melchior (2011), xvii, 270 Seiten
ISBN: 978-3-89336-690-3

97. **Secondary Organic Aerosols: Chemical Aging, Hygroscopicity, and Cloud Droplet Activation**
by A. Buchholz (2011), xiv, 134 pages
ISBN: 978-3-89336-691-0

Energie & Umwelt / Energy & Environment
Band / Volume 99
ISBN 978-3-89336-693-4

JÜLICH
FORSCHUNGSZENTRUM